Investigation of calculated adiabatic temperature change of $MnFeP_{1-x}As_x$ alloys

by

David Oliver Campbell
Bachelor of Science, University of Victoria, 2009

A Thesis Submitted in Partial Fulfillment of the Requirements for the Degree of

MASTER OF APPLIED SCIENCE

in the

Department of Mechanical Engineering

© David Oliver Campbell, 2015
University of Victoria

All rights reserved. This thesis may not be reproduced in whole or in part, by photocopy or other means, without the permission of the author.

Supervisory Committee

Investigation of calculated adiabatic temperature change of $MnFeP_{1-x}As_x$ alloys

by

David Oliver Campbell
Bachelor of Science, Major Physics, Minor Mathematics University of Victoria, 2009

Supervisory Committee

Dr. Andrew Rowe (Department of Mechanical Engineering)
Supervisor

Dr. Rustom Bhiladvala (Department of Mechanical Engineering)
Departmental Member

Abstract

Supervisory Committee
Dr. Andrew Rowe (Department of Mechanical Engineering)
Supervisor

Dr. Rustom Bhiladvala (Department of Mechanical Engineering)
Departmental Member

Magnetic refrigeration is an alternative cooling technology to vapour compression. Due to the large operating space of magnetic refrigeration devices, modelling is critical to predict results, optimize device parameters and regenerator design, and understand the physics of the system. Modeling requires accurate material data including specific heat, magnetization and adiabatic temperature change, ΔT_{ad}. For a reversible material ΔT_{ad} can be attained directly from measurement or indirectly through calculation from specific heat and magnetization data. Data sets of nine $MnFeP_{1-x}As_x$ alloys are used to compare calculated against measured ΔT_{ad}. $MnFeP_{1-x}As_x$ is a promising first order material because of a tunable transition temperature, low material cost and large magnetocaloric properties. Because $MnFeP_{1-x}As_x$ alloys exhibit thermal hysteresis there are four possible calculation protocols for adiabatic temperature change; $\Delta T_{ad,HH}$, $\Delta T_{ad,CC}$, $\Delta T_{ad,HC}$ and $\Delta T_{ad,CH}$. $\Delta T_{ad,CH}$ deviates the most from measured data and therefore it is assumed that this case is not representative of the material behavior. Results show $\Delta T_{ad,HH}$ and $\Delta T_{ad,CC}$ align with measured data as well as $\Delta T_{ad,HC}$. The three protocols that align best with measured data have two consistent errors including a colder peak ΔT_{ad} and a larger $FWHM$. With more data sets and analysis a preferred calculation protocol may be found.

Table of Contents

Supervisory Committee ii
Abstract iii
Table of Contents iv
List of Tables vi
List of Figures vii
Nomenclature xv
Acronyms xv
Constants xv
Gadolinium Properties xv
Alphabetic xvi
Greek xix
Acknowledgments xxi
Dedication xxii
Chapter 1 – Introduction 1
1.1. Increasing demand for cooling technologies 1
1.2. Magnetic refrigeration 3
1.3. The Magnetocaloric Effect 4
1.4. The active magnetic regenerative (AMR) cycle 6
1.5. Magnetocaloric materials 8
1.6. Curie Temperature 8
1.7. Investigated material: $MnFeP_{1-x}As_x$ alloys 12
1.8. Objectives 13
1.9. Summary 15
Chapter 2 – Theory 17
2.1. Thermodynamics 17
2.2. Mean field theory 24
2.3. Magnetic entropy and specific heat 33
2.4. Lattice entropy and specific heat 35
2.5. Electronic entropy and specific heat 35
2.6. First order MFT 36
2.7. MFT Summary 37
2.8. Demagnetization 40
2.9. Summary 42
Chapter 3 – Methods 43
3.1. Data Collection 47
3.1.1. Specific heat 47
3.1.2. Magnetization 49
3.1.3. Adiabatic temperature change 51
3.2. Smoothing 52
3.3. Interpolation 57
3.3.1. Specific heat interpolation 58
3.3.2. Magnetization interpolation 63

3.3.3. Entropy interpolation 64
3.4. Demagnetization factors 65
3.5. Correcting magnetization data for demagnetizing field 66
3.6. Correcting specific heat data for demagnetization 68
3.7. Hysteresis 70
3.8. Uncertainties 73
3.9. Summary 77
Chapter 4 – Results 78
4.1. MFT Gadolinium results 78
4.1.1. Magnetization 79
4.1.2. Specific heat 80
4.1.3. Entropy 82
4.1.4. Adiabatic temperature change 84
4.1.5. Isothermal field induced change in entropy 86
4.2. Isothermal field induced change in entropy of $MnFeP_{1-x}As_x$ 87
4.3. Demagnetization results 90
4.4. Measured versus calculated ΔT_{ad} 91
Chapter 5 – Discussion 104
5.1. Demagnetization 104
5.2. Measured versus calculated ΔT_{ad} of $MnFeP_{1-x}As_x$ alloys 105
5.3. Summary 110
Chapter 6 – Conclusion and Recommendations 111
Bibliography 113
Appendix A – Isothermal field induced entropy change derivation 116

List of Tables

Table 1-1– The alloy labels and respective Curie temperatures are presented here. 13

Table 1-2 –The ΔT_{ad} labeling convention is outlined here. 14

Table 2-1 – Orbital diagram of the $4f^7$ subshell of Gadolinium. The numbers represent the orbital quantum number m_l and each arrow represents an electron and its spin. 29

Table 2-2 – The labeling convention of different magnetization quantities is presented below. 31

Table 2-3 – Values of parameter η for various $MnFeP_{1-x}As_x$ materials of Curie temperatures. 37

Table 3-1 – Applied magnetic field strengths 58

Table 3-2 – Sample dimensions and demagnetizing factors for specific heat and magnetization data. 66

Table 3-3 – Protocols are defined by the low and high field entropy curve used to determine the isentropic temperature change. 72

Table 4-1 – The three metrics that define the measured and calculated ΔT_{ad} curves for all nine alloys are presented in this table. Two other properties are presented here, hysteresis, and dT/dH. Hysteresis (Hyst.) is defined here as the difference in temperature between the heating and cooling zero field specific heat peaks. dT/dH is defined here as the shift in the temperature of the peak specific heat with increasing field strength. 96

Table 4-2 – The 9 material average errors between calculated and measured ΔT_{ad} are presented. 100

List of Figures

Figure 1-1 – The percentage of delivered residential energy consumption by electricity in 2011 of cooling technologies. The total energy delivered by electricity in 2011 was 4.9 quadrillion BTU [1]. 2

Figure 1-2 – The projected percentage of delivered energy consumption by electricity in 2040 of cooling technologies. The total energy delivered by electricity in 2040 is forecasted to be 6.0 quadrillion BTU [1]. 2

Figure 1-3 – Cooling degree days of each country [4]. 2

Figure 1-4 – The left process represents the steps of MR while the right process represents GCR. The colours represent the temperature of the MCM on the left and the refrigerant on the right, green indicating starting temperature, blue indicating colder temperature and red indicating hotter temperature. H represents a magnetic field, Q represents heat (negative indicates heat leaving the system), and ΔT_{ad} represents the adiabatic change in temperature due to the MCE. 4

Figure 1-5 – The entropy curves of Gadolinium at zero and two Tesla. By plotting the high and low field entropy curves, the adiabatic temperature change and isothermal entropy change can be determined. The reference temperature for both these derived properties is the temperature at low magnetic field. 5

Figure 1-6 – The adiabatic temperature change of Gadolinium and two $MnFeP_{1-x}As_x$ compounds are displayed here. The Gadolinium data is from AMES laboratory, and the $MnFeP_{1-x}As_x$ data is from BASF. Gadolinium is a second order MCM characterized by the broad adiabatic temperature change peak. $MnFeP_{1-x}As_x$ compounds are first order MCMs characterized by a narrow adiabatic temperature change peak. 6

Figure 1-7 – T-s diagram of the MCM in an AMR cycle. H_H and H_L are high and low fields, respectively. *a'* and *c'* represent the temperature of the solid refrigerant after a field change while *a* and *c* represent the equilibrium temperature of the solid and fluid. 7

Figure 1-8 – Gadolinium (2^{nd} order) specific heat data [8]. 10

Figure 1-9 - $MnFeP_{1-x}As_x$ (1^{st} order) specific heat data [9]. 10

Figure 1-10 – Gadolinium ΔT_{ad} data corrected for demagnetization [10]. 11

Figure 1-11 - $MnFeP_{1-x}As_x$ calculated ΔT_{ad} data corrected for demagnetization. 11

Figure 1-12 – Calculated ΔT_{ad} curves of a $MnFeP_{1-x}As_x$ alloy, sample 2. 15

Figure 1-13 – A flow chart describing the calculation process of ΔT_{ad} from specific heat and magnetization. The colour boxes represent data while the numbers in brackets correspond to equations described in the Chapter 2 – Theory. 16

Figure 2-1 – Gadolinium entropy data obtained from integrating MFT specific heat data are plotted to illustrate the different components to the entropy integration. The red line represents entropy contribution from the Δs term that can be calculated. The blue dashed line represents the entropy contribution from the s_0 term that cannot be calculated because there is no data for this temperature range. 19

Figure 2-2 – Gadolinium change in entropy data for two field strengths using T=250K as the reference temperature. Note that at T=250K, both field strengths have the same entropy which is not possible. 20

Figure 2-3 – Representative entropy curves are plotted to show the effect of adding the magnetic entropy correction, Δs_H, to the entropy calculation shown in Equation (2.8). 20

Figure 2-4 – Example $MnFeP_{1-x}As_x$ alloy entropy curves at 0T and 1.1T. The solid red line represents the corrected high field entropy curve calculated using Equation (2.8). The dashed red line represents high field entropy calculated using Equation (2.5). 22

Figure 2-5 – Focussing on a smaller temperature range makes the magnetic entropy correction more visible. 22

Figure 2-6 – A visual representation of the ΔT_{ad} calculation is given above. Note that the ΔT_{ad} is defined as a function of the temperature at low magnetic field. 23

Figure 2-7 – The total angular momentum $\vec{J}$ is the sum of the orbital $\vec{L}$ and spin $\vec{S}$ angular momenta. The momentum vectors have a magnitude of $\hbar\sqrt{x(x+1)}$ where $x = s_q, l, j$. The magnetic moments associated with these momenta are also displayed. Note that μ is the total angular momentum and has a component parallel and perpendicular to $\vec{J}$, but only the parallel component contributes to the magnetic moment [15]. 26

Figure 2-8 – Vector model of Gadolinium with an applied magnetic field in the z direction. The arrows represent the possible orbital momentum $\vec{L}$ vectors while the values along the m_l axis represent the associated possible values of the orbital momentum quantum number l [16]. 28

Figure 2-9 – The Brillouin function plotted against the ratio x for different j values.... 32

Figure 2-10 – A flow chart describing the progression of calculating material properties using MFT. This chart progression flows top to bottom. The numbers in brackets between the coloured boxes correspond to equation numbers. The equations are applied to the data in the box above to yield the resultant data in the box below. Note that all data on this flow chart is mass specific rather than total as can be seen by the lower case letters. 39

Figure 3-1 – A flow chart describing the processing of the specific heat data is presented. The numbers in brackets are related to sections of this document that explain the processes. 44

Figure 3-2 – A flow chart describing the processing of the magnetization data is presented. The numbers in brackets are related to sections of this document that explain the processes. The differentiation and integration of magnetization data with respect to temperature do not have a sections devoted them. 45

Figure 3-3 – A flow chart describing the processing of the entropy data is presented. The numbers in brackets are related to sections of this document that explain the processes. 46

Figure 3-4 – A flow chart describing the processing of the ΔT_{ad} data is presented. The numbers in brackets are related to sections of this document that explain the processes. 46

Figure 3-5 – A schematic of a DSC. The computer uses the data from the thermocouples to ensure that both the sample and reference are changing temperature at the same rate by adjusting the power delivered to each heater. 48

Figure 3-6 – Sample-field orientation of in-field specific heat and magnetization measurements. 48

Figure 3-7 – From left to right the above image shows a dime, the mDSC sample holder, and the mDSC sample lid. The lid sits on top of the crucible in the orientation shown such that it reduces the volume of the crucible by a small amount. 49

Figure 3-8 – The above image shows (from left to right) a connected VSM sample holder, a disconnected VSM sample holder, and a dime. The pink material in the connected sample holder illustrates how the sample would be contained in the VersaLab VSM. 51

Figure 3-9 – Schematic of sample size and orientation in BASF ΔT_{ad} device to measure adiabatic temperature change. The magnetic field lines are parallel to the 5 mm

side of the sample. (A) represents the low field position and (B) represents the high field position. 52

Figure 3-10 – The percent difference between smoothing and raw heating magnetization data for a sample material is presented here. 54

Figure 3-11 – The temperature derivative of raw magnetization data. 55

Figure 3-12 – The temperature derivative of smoothed magnetization data. 55

Figure 3-13 – Raw and smoothed heating adiabatic temperature change data are plotted. The percent difference between the raw and smoothed data are also plotted. 56

Figure 3-14 – A closer look at the peak adiabatic temperature change data shows the necessity of smoothing. Without smoothing, determining the temperature and magnitude of the peak would be difficult. 57

Figure 3-15 – The blue and red line represent measured specific heat data while the orange dotted line represents specific heat data at an interpolated field strength using the temperature offset interpolation method. δT_{peak} is the temperature offset and is defined as the difference in temperature of the high and low field specific heat peaks. 59

Figure 3-16 – Sample heating specific heat data. 59

Figure 3-17 – The dark blue columns represent specific heat data at different field strengths, the tan columns represent interpolated specific heat data, and the red bars indicate the peak specific heat value for each field strength. 62

Figure 3-18 – Temperature offset interpolation results of a sample $MnFeP_{1-X}As_X$ material between zero and 0.5 Tesla. 63

Figure 3-19 – The blue and red lines represent entropy curves calculated from specific heat data. The green dashed line represents an entropy curve calculated by isothermal linear interpolation. 65

Figure 3-20 – Magnetization data diagram. Each column of data is exposed to the same field, and each row of data is exposed to the same ambient temperature. This diagram highlights that the magnetization values are dependent on internal field H_{in} rather than the applied field H_a 67

Figure 3-21 –Heating magnetization data of an example $MnFeP_{1-x}As_x$ material. The dashed lines are magnetization data at constant H_a while the solid lines are magnetization data at constant H_{in}. 68

Figure 3-22 –Heating entropy data of an example $MnFeP_{1-x}As_x$ material. The dashed lines are m-data at constant H_a while the solid lines are m-data at constant H_{in} ... 70

Figure 3-23 – Heating and cooling specific heat data at two applied field strengths of sample 2. ... 71

Figure 3-24 – Heating and cooling magnetization data at three applied fields of a sample 2. ... 71

Figure 3-25 – Schematic of the four ΔT_{ad} calculation protocols. ... 72

Figure 3-26 – The maximum and RSS absolute uncertainties in calculated adiabatic temperature change are plotted with the calculated adiabatic temperature change. 76

Figure 4-1 – Magnetization of Gadolinium at three field strengths. ... 79

Figure 4-2 – Specific heat has three components that are plotted above: lattice, electronic and magnetic. Total specific heat data produced by MFT of Gadolinium for three internal field strengths are also plotted. ... 80

Figure 4-3 – Gadolinium MFT results compared to the original AMES specific heat data [8]. ... 81

Figure 4-4 – Gadolinium MFT results compared to the corrected AMES specific heat data [10]. ... 81

Figure 4-5 – The difference in entropy calculated from method 1 and 2 are plotted. The difference is calculated by subtracting method 1 results from method 2 results. ... 82

Figure 4-6 – Calculated entropy data at three internal field strengths. ... 83

Figure 4-7 – A closer look at the entropy curves near the Curie temperature. ... 83

Figure 4-8 – The data series with hollow markers are the original adiabatic temperature change data that has not been corrected for demagnetization. The original data series are labeled with H_a which stands for applied field. The data series with solid markers are the corrected data. The corrected data series are labeled with H_in which stands for internal field. ... 84

Figure 4-9 - MFT adiabatic temperature change compared to original adiabatic temperature change data from AMES laboratory. ... 85

Figure 4-10 – MFT adiabatic temperature change compared to demagnetization corrected adiabatic temperature change data from AMES laboratory. ... 85

Figure 4-11 – The percent difference between adiabatic temperature change data calculated using two different methods is plotted here for three magnetic field changes. 86

Figure 4-12 – The magnetic entropy change offset of each material for a field change from 0-1.1T..... 88

Figure 4-13 – The increase in adiabatic temperature change due to the addition of the magnetic entropy change is illustrated here. 88

Figure 4-14 – The 'offset' is the magnetic entropy change value that is subtracted from the entire high field entropy curve..... 89

Figure 4-15 – Adiabatic temperature change results from including and ignoring demagnetization are compared for sample 2. 90

Figure 4-16 - The metrics use to compare the measured against the calculated ΔT_{ad} including peak magnitude $\left(\Delta T_{peak}\right)$, peak temperature $\left(T_{peak}\right)$, and full width at half maximum $\left(FWHM\right)$ are presented here. 92

Figure 4-17 – Material 1 measured heating adiabatic temperature change data compared against three calculated adiabatic temperature change data sets. 93

Figure 4-18 – Material 1 measured cooling adiabatic temperature change data compared against three calculated adiabatic temperature change data sets. 93

Figure 4-19 – Material 2 measured heating adiabatic temperature change data compared against three calculated adiabatic temperature change data sets. 94

Figure 4-20 – Material 2 measured cooling adiabatic temperature change data compared against three calculated adiabatic temperature change data sets. 94

Figure 4-21 – Material 7 measured heating adiabatic temperature change data compared against three calculated adiabatic temperature change data sets. 95

Figure 4-22 – Material 7 measured cooling adiabatic temperature change data compared against three calculated adiabatic temperature change data sets. 95

Figure 4-23 – Calculated ΔT_{ad} peak magnitudes relative to the measured heating ΔT_{ad} peak. A positive value indicates calculated values are higher than measured. A negative value indicates calculated values are lower than measured. The Curie temperature increases with material number. 97

Figure 4-24 – Calculated ΔT_{ad} peak magnitudes relative to the measured cooling ΔT_{ad} peak..... 97

Figure 4-25 – Calculated ΔT_{ad} peak temperatures relative to the measured heating ΔT_{ad} peak..... 98

Figure 4-26 – Calculated ΔT_{ad} peak temperatures relative to the measured cooling ΔT_{ad} peak..... 98

Figure 4-27 – Calculated ΔT_{ad} FWHM relative to the measured heating ΔT_{ad} FWHM. 99

Figure 4-28 – Calculated ΔT_{ad} FWHM relative to the measured cooling ΔT_{ad} FWHM. 99

Figure 4-29 – Error relative to measured heating ΔT_{ad} 100

Figure 4-30 - Error relative to measured cooling ΔT_{ad} 100

Figure 4-31 – Material 1 measured heating adiabatic temperature change data compared against two calculated adiabatic temperature change data sets. The shaded areas represent the uncertainties of each data set. 101

Figure 4-32 – Material 1 measured cooling ΔT_{ad} data compared to two calculated ΔT_{ad} data sets. 101

Figure 4-33 – Material 2 measured heating adiabatic temperature change data compared against two calculated adiabatic temperature change data sets. 102

Figure 4-34 – Material 2 measured cooling ΔT_{ad} data compared to two calculated ΔT_{ad} data sets. 102

Figure 4-35 – Material 7 measured heating adiabatic temperature change data compared against two calculated adiabatic temperature change data sets. 103

Figure 4-36 – Material 7 measured cooling ΔT_{ad} data compared to two calculated ΔT_{ad} data sets. 103

Figure 5-1 – Measured peak ΔT_{ad} is plotted against hysteresis for all nine alloys. 108

Figure 5-2 – Calculated peak ΔT_{ad} is plotted against hysteresis for all nine alloys. Heating represents calculated $\Delta T_{ad,HH}$ and cooling represents calculated $\Delta T_{ad,CC}$ 108

Figure 5-3 – Measured FWHM is plotted against hysteresis for all nine alloys..... 109

Figure 5-4 – Calculated FWHM is plotted against hysteresis for all nine alloys. Heating represents calculated $\Delta T_{ad,HH}$ and cooling represents calculated $\Delta T_{ad,CC}$ 109

Nomenclature

Acronyms

MR	Magnetic refrigeration
VC	Vapour compression refrigeration
MCE	Magnetocaloric effect
MCM	Magnetocaloric material
AMR	Active magnetic regenerator
MFT	Mean field theory
DSC	Digital scanning calorimeter
VSM	Vibrating sample magnetometer

Constants

R	Universal gas constant	8.314 $Jmol^{-1}\ K^{-1}$
μ_0	Permeability of free space	$4\pi x10^{-7}\ Hm^{-1}$
μ_B	Bohr magneton	$9.27x10^{-24}\ JT^{-1}$
k_B	Boltzmann constant	$1.381x10^{-23}\ JK^{-1}$
N_A	Avogadro constant	$6.02214x10^{23}$ molecules mol^{-1}

Gadolinium Properties

MW	Molecular mass	0.15725 $kgmol^{-1}$
ρ	Density	7900 kgm^{-3}
s_q	Electron spin	3.5
l	Orbital angular momentum	0
j	Total angular momentum	3.5

T_C	Curie temperature	293.4 K
T_D	Debye temperature	169 K
γ	Sommerfeld constant	0.00448 $Jmol^{-1}K^{-2}$
g	Landé g-factor	2

Alphabetic

B	Magnetic field	T
$B_J(x)$	Brillouin function	-
c_{elec}	Mass specific electronic specific heat	$J \cdot kg^{-1} \cdot K^{-1}$
c_H	Mass specific magnetic specific heat	$J \cdot kg^{-1} \cdot K^{-1}$
c_{Lat}	Mass specific lattice specific heat	$J \cdot kg^{-1} \cdot K^{-1}$
C_{Elec}	Electronic specific heat	$J \cdot K^{-1}$
C_H	Magnetic specific heat	$J \cdot K^{-1}$
C_{Lat}	Lattice specific heat	$J \cdot K^{-1}$
$E(k)$	Complete elliptic integral of the second kind	-
F	Helmholtz free energy	J
$FWHM$	Full width at half maximum	K
g	Landé factor	-
G	Gibbs free energy	J
H	Magnetic field strength	$A \cdot m^{-1}$
H_a	Applied magnetic field strength	$A \cdot m^{-1}$ or T
H_d	Demagnetizing field	$A \cdot m^{-1}$ or T

H_{in}	Internal magnetic field strength	$A \cdot m^{-1}$ or T
H_{tot}	Total magnetic field strength	$A \cdot m^{-1}$ or T
j	Total angular momentum quantum number	-
$\vec{J}$	Total angular momentum	$J \cdot s$ or $eV \cdot s$
k	Elliptic modulus	-
K	Compressibility factor	-
$K(k)$	Complete elliptic integral of the first kind	-
l	Orbital angular momentum quantum number	-
$\vec{L}$	Orbital angular momentum	$J \cdot s$ or $eV \cdot s$
m_j	Possible total angular momentum quantum number values	-
m_l	Possible orbital angular momentum quantum number values	-
m_s	Possible spin angular momentum quantum number values	-
m	Mass specific magnetization	$A \cdot m^2 \cdot kg^{-1}$
$\dot{m}$	Molar specific magnetization	$A \cdot m^2 \cdot mol^{-1}$
M	Magnetization	$A \cdot m^{-1}$
M_T	Total magnetization	$A \cdot m^2$ or $J \cdot T^{-1}$
N	Total atoms	-
$\dot{N}$	Atoms per mole	$atoms \cdot mol^{-1}$
N_s	Number of spins (atoms) per kg $\left(N_A / MW\right)$	$atoms \cdot kg^{-1}$
p	Length to diameter ratio	-
P_i	Probability of atom with energy ε_i	-

s	Mass specific entropy	$J \cdot kg^{-1} \cdot K^{-1}$
s_q	Spin angular momentum quantum number	-
$\vec{S}$	Spin angular momentum	$J \cdot s$ or $eV \cdot s$
s_{elec}	Mass specific electronic entropy	$J \cdot kg^{-1} \cdot K^{-1}$
s_H	Mass specific magnetic entropy	$J \cdot kg^{-1} \cdot K^{-1}$
s_{Lat}	Mass specific lattice entropy	$J \cdot kg^{-1} \cdot K^{-1}$
S_{Elec}	Electronic entropy	$J \cdot K^{-1}$
S_H	Magnetic entropy	$J \cdot K^{-1}$
S_{Lat}	Lattice entropy	$J \cdot K^{-1}$
T	Temperature	K
T_C	Curie temperature	K
T_D	Debye temperature	K
T_{peak}	Temperature of ΔT_{ad} peak	K
U	Internal energy	J
U_H	Magnetic contribution to internal energy	J
V	Volume	m^3
x	Magnetic to thermal energy ratio	-
Z	Partition function	-

Greek

β	Volume change coefficient	-
ΔT_{ad}	Adiabatic temperature change	K
$\Delta T_{ad,CC}$	ΔT_{ad} calculated with cooling low field and cooling high field entropy data	K
$\Delta T_{ad,CH}$	ΔT_{ad} calculated with cooling low field and heating high field entropy data	K
$\Delta T_{ad,CH}$	ΔT_{ad} calculated with cooling low field and heating high field entropy data	K
$\Delta T_{ad,HC}$	ΔT_{ad} calculated with heating low field and cooling high field entropy data	K
$\Delta T_{ad,HH}$	ΔT_{ad} calculated with heating low field and heating high field entropy data	K
ΔT_{peak}	Maximum value of ΔT_{ad}	K
ε_i	Energy level (Eigen value)	J
ζ	Spin-orbit parameter	-
$\mathcal{H}_D$	Dirac Hamiltonian	-
$\mathcal{H}_{S,L}$	Zeeman Hamiltonian	-
λ	Mean field parameter	$T \cdot \left(J \cdot T^{-1} \right)^{-1}$
η	Transition parameter	-
$\mathcal{N}$	Demagnetizing factor	-
$\mathcal{N}_l$	Axial demagnetizing factor of cylinder	-
$\mathcal{N}_p$	Demagnetizing factor of packed particles	-
$\mathcal{N}_r$	Radial demagnetizing factor of cylinder	-

$\mathcal{N}_{rp}$	Radial demagnetizing factor of cylinder of packed particles	-
Ψ_i	Wave function (Eigen function)	-
μ_z	Magnetic moment parallel component to $\vec{B}$	$J \cdot T^{-1}$

Acknowledgments

Thank you for your guidance through this program Andrew. I have learned a lot of applicable skills during my time here from you, the hands on experience in the lab, and working with BASF. You gave me the opportunity to travel more than I have ever been able to; France, Japan, Montreal, The Netherlands, and Germany, and I am grateful for this. Who can say they've worked out with their supervisor? It has been a great time here for me, thank you!

Dedication

I would like to dedicate this to my Mom and Dad. I have so many good memories thanks to you two. Thank you for all the family ski trips, sailing adventures and Kelowna summers. I couldn't have asked for better parents.

Chapter 1 – Introduction

Motivation for the field of room temperature magnetic refrigeration is presented. The basics of magnetic refrigeration including the magnetocaloric effect, magnetocaloric materials, and the active magnetic regenerative cycle are defined and explained. Material properties of magnetocaloric materials that include adiabatic temperature change and hysteresis are also discussed to introduce the topics of this thesis.

1.1. Increasing demand for cooling technologies

The demand for cooling technologies is growing. Figure 1-1 and Figure 1-2 show this growth in the United States [1]. Not only is the total energy usage by electricity in the United States increasing, but the share consumed by cooling technologies is also forecasted to increase. Figure 1-3 displays the Cooling Degree Days (CDD) of each country. A CDD is defined as the difference between the daily mean environmental temperature and a human comfort temperature taken to be 18 ^{0}C provided the environmental temperature is above the comfort temperature [2]. This daily value is summed up for an entire year to give the number of CDDs in a year for each country. The CDD gives an idea of the energy demands of different countries for cooling technologies. It can be seen in Figure 1-3 that both developing countries China and India have more CDD than the developed United States. This further emphasizes that the energy demand required by cooling technologies will continue to grow. Therefore improving the efficiency of cooling technologies will decrease environmental impact and reduce electricity costs greatly. Magnetic refrigeration is an alternative cooling technology to vapour compression that could possibly be more efficient [3].

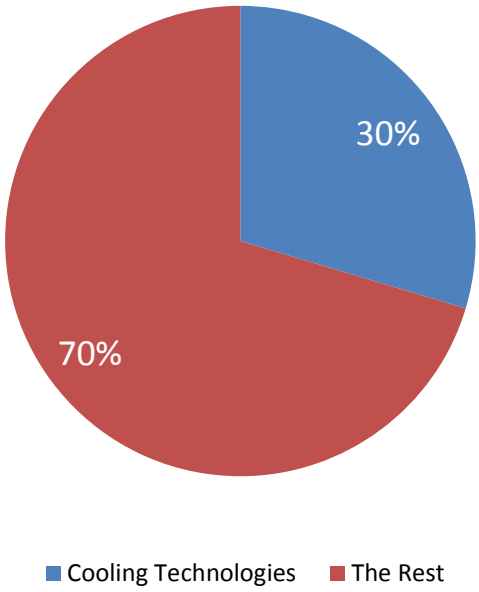

Figure 1-1 – The percentage of delivered residential energy consumption by electricity in 2011 of cooling technologies. The total energy delivered by electricity in 2011 was 4.9 quadrillion BTU [1].

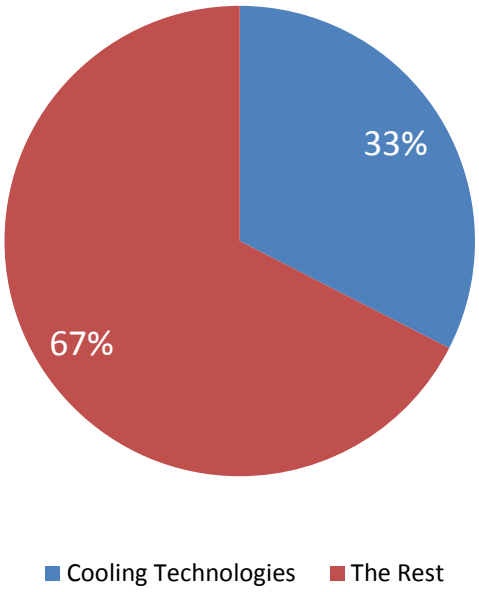

Figure 1-2 – The projected percentage of delivered energy consumption by electricity in 2040 of cooling technologies. The total energy delivered by electricity in 2040 is forecasted to be 6.0 quadrillion BTU [1].

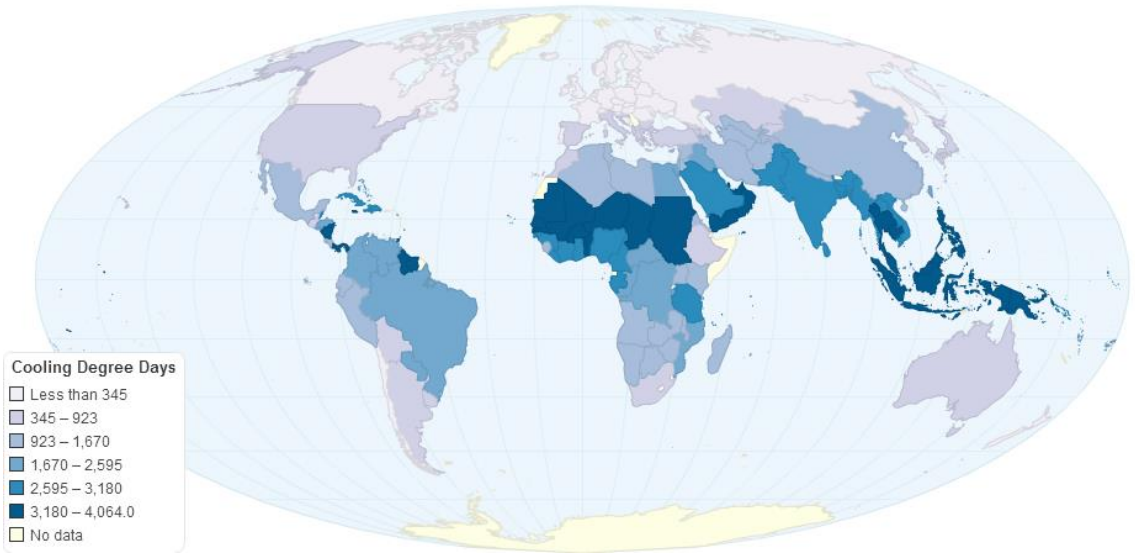

Figure 1-3 – Cooling degree days of each country [4].

1.2. Magnetic refrigeration

Magnetic refrigeration (MR) is an alternative cooling or heat pump technology to vapour compression (VC). It has been proposed that MR has the potential to be more efficient than VC [3], [5]. The magnetocaloric effect (MCE) is a thermomagnetic effect that is utilized by magnetic refrigeration to pump heat. The MCE is defined as an adiabatic temperature change or an isothermal entropy change with the application of a magnetic field to a magnetocaloric material (MCM) [6]. Because the MCE produces a small temperature change, approximately 3 Kelvin per Tesla, an active magnetic regenerative (AMR) cycle is employed to generate larger temperature spans [7]. Figure 1-4 shows the similarities between MR and VC. The four steps of VC are compression, condensation, expansion, and evaporation. MR also has four steps which include magnetization, heat rejection, demagnetization, and heat absorption. The four steps of the MR process will be discussed in Section 1.4.

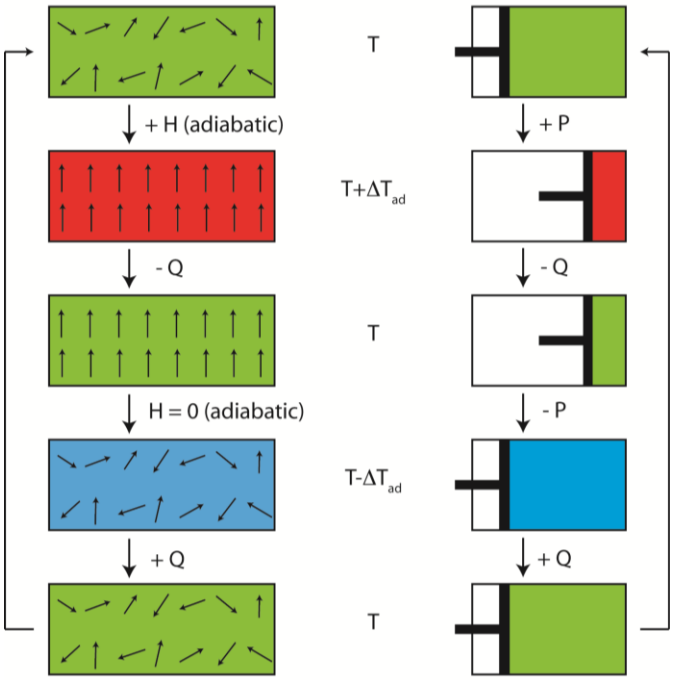

Figure 1-4 – The left process represents the steps of MR while the right process represents GCR. The colours represent the temperature of the MCM on the left and the refrigerant on the right, green indicating starting temperature, blue indicating colder temperature and red indicating hotter temperature. H represents a magnetic field, Q represents heat (negative indicates heat leaving the system), and ΔT_{ad} represents the adiabatic change in temperature due to the MCE.

1.3. The Magnetocaloric Effect

The MCE can be defined by an adiabatic temperature change $\left(\Delta T_{ad}\right)$ or an isothermal entropy change $\left(\Delta S_H\right)$ (see Figure 1-5). Adiabatic temperature change is physical and can be measured while entropy cannot be directly measured therefore ΔT_{ad} will be focussed on here. To measure the MCE of a MCM in terms of ΔT_{ad} a sample is thermally isolated therefore $dQ = 0$. If reversible, the second law of thermodynamics states $dQ = TdS$, therefore if $dQ = 0$ then $dS = 0$. Total entropy of a material is the sum of magnetic, lattice, and electronic entropies. The sample is then exposed to a magnetic

field which aligns the magnetic dipoles of the material causing a decrease in magnetic entropy. Since the total entropy is constant, $dS = 0$, the lattice entropy must increase to maintain the total entropy [6]. This increase in lattice entropy causes an increase in temperature. This temperature increase is the adiabatic temperature change. Figure 1-6 shows the temperature change of commonly used MCMs caused by the MCE when the magnetic field varies from zero to 1.1 Tesla. Due to this small temperature change an active magnetic regenerative (AMR) cycle is implemented to increase the temperature span that can be developed by MCMs.

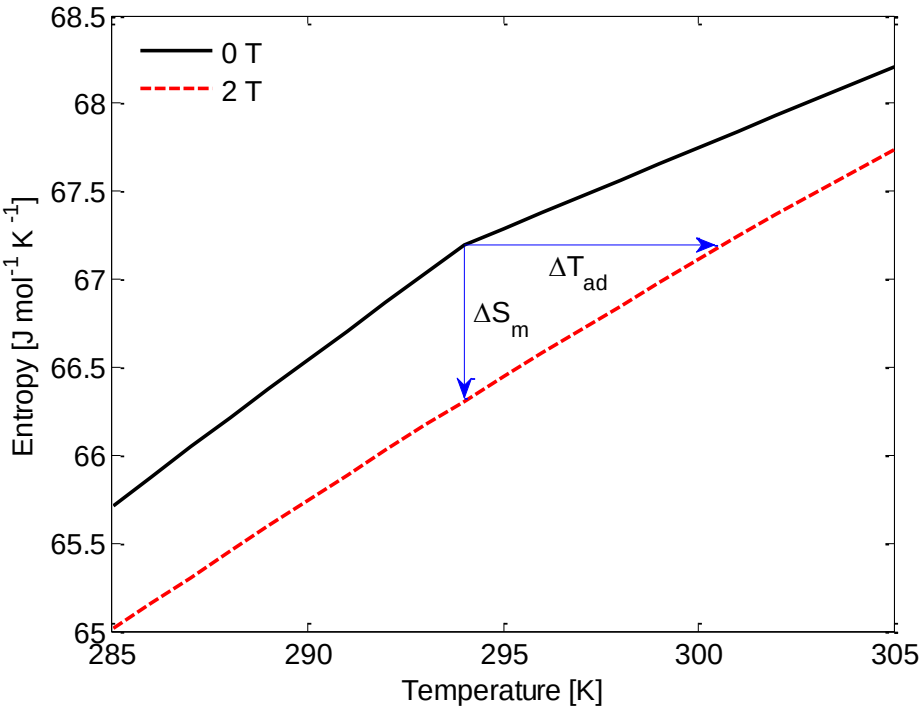

Figure 1-5 – The entropy curves of Gadolinium at zero and two Tesla. By plotting the high and low field entropy curves, the adiabatic temperature change and isothermal entropy change can be determined. The reference temperature for both these derived properties is the temperature at low magnetic field.

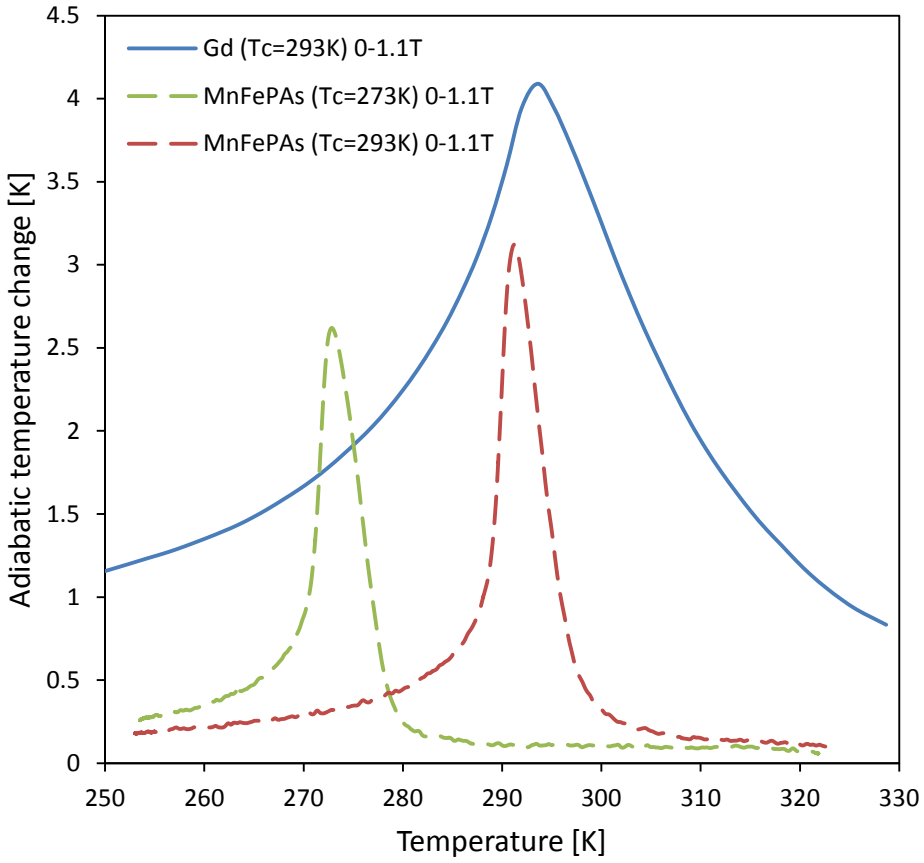

Figure 1-6 – The adiabatic temperature change of Gadolinium and two $MnFeP_{1-x}As_x$ compounds are displayed here. The Gadolinium data is from AMES laboratory, and the $MnFeP_{1-x}As_x$ data is from BASF. Gadolinium is a second order MCM characterized by the broad adiabatic temperature change peak. $MnFeP_{1-x}As_x$ compounds are first order MCMs characterized by a narrow adiabatic temperature change peak.

1.4. The active magnetic regenerative (AMR) cycle

The AMR cycle combines passive regenerator technology with the MCE by constructing a regenerator out of MCM. Passive regenerators are made up of a variety of solid matrix structures including packed spheres, parallel plates and meshes. These matrices are made up of materials with high heat transfer properties. Fluid is then oscillated through these matrices. In one direction the fluid rejects heat to the regenerator and the exiting fluid is colder than the entering fluid. When the flow is reversed the colder entering fluid then absorbs the heat the regenerator just acquired and in doing so

the exiting fluid is hotter than the entering fluid. A passive regenerator helps maintain a temperature difference between two fluid reservoirs by operating in this fashion. To make the regenerator 'active' the solid matrix material is replaced with one or many MCM(s). By timing the application and removal of a magnetic field the MCE and passive regenerator effect work together. The AMR cycle can be broken down to four processes displayed in a T-s diagram in Figure 1-7; adiabatic magnetization $(b \to c')$, fluid flow from cold to hot side $(c' \to d)$, adiabatic demagnetization $(d \to a')$, and fluid flow from hot to cold side $(a' \to b)$. When blowing fluid from the cold to hot side of the device, the material is magnetized causing it to be hotter, the fluid absorbs heat and rejects it to the hot side. The AMR is then cooled by demagnetization and fluid is blown from the hot to cold side rejecting its heat to the AMR. Exiting the cold side of the AMR the fluid is at its coldest point and can absorb some heat within the cold side of the device. The AMR cycle enables MR devices to attain larger temperature spans than the ΔT_{ad} of the MCM.

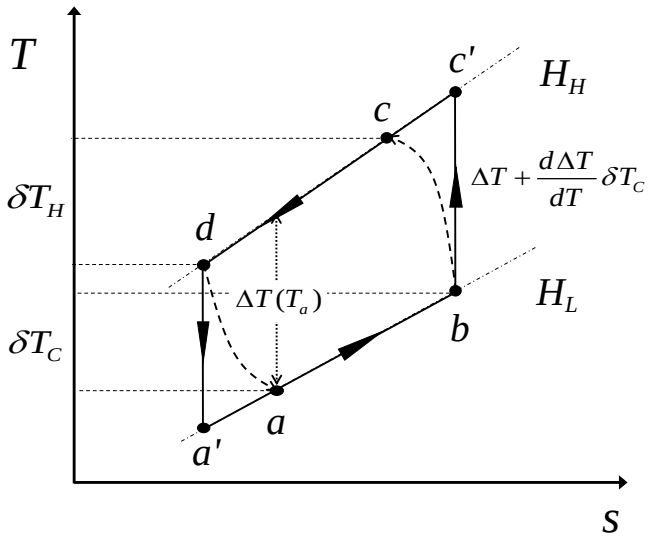

Figure 1-7 – T-s diagram of the MCM in an AMR cycle. H_H and H_L are high and low fields, respectively. *a'* and *c'* represent the temperature of the solid refrigerant after a field change while *a* and *c* represent the equilibrium temperature of the solid and fluid

1.5. Magnetocaloric materials

Magnetocaloric materials are materials that exhibit a thermal response to the application and removal of a magnetic field. As shown in Figure 1-6 there are two classes of ordinary MCMs; first and second order materials. Ordinary MCMs undergo a transition from ferromagnetic to paramagnetic at the Curie temperature and heat up with the application of a magnetic field. MCMs are in an ordered magnetic state (often ferromagnetic) at temperatures colder than the Curie temperature and paramagnetic at temperatures hotter than the Curie temperature. A material is ferromagnetic when the dipoles of the material are aligned in the absence of an applied field. Permanent magnets are ferromagnetic. The dipoles of a paramagnetic material are not aligned but are susceptible to a magnetic field. The phase transition causes a peak in the specific heat and adiabatic temperature change. The nature of the phase transition defines the material class. Second order MCMs are characterized by broad specific heat and ΔT_{ad} peaks while first order MCMs are characterized by narrow peaks as can be seen in Figure 1-6. The temperature of the phase transition is known as the Curie temperature.

1.6. Curie Temperature

The Curie temperature of a material is the temperature at which the dipoles of the material have enough thermal energy to become disordered. Below the Curie temperature the material is ferromagnetic. Above the Curie temperature the material is paramagnetic. This transition occurs at a temperature that closely corresponds with the temperature of the peak in both specific heat and ΔT_{ad}. In this thesis, the Curie temperature will be defined as the *heating* peak specific heat temperature at zero field. Figure 1-8 and Figure 1-9 show that the peak specific heat temperature does not change with temperature for 2nd

order materials whereas the peak specific heat temperature shifts hotter with increasing magnetic field strength for 1st order materials. Figure 1-10 and Figure 1-11 show the same trend with the peak ΔT_{ad} temperature with increasing field. Because of the shifting peaks, it is important to have a concise definition of Curie temperature when discussing first order materials.

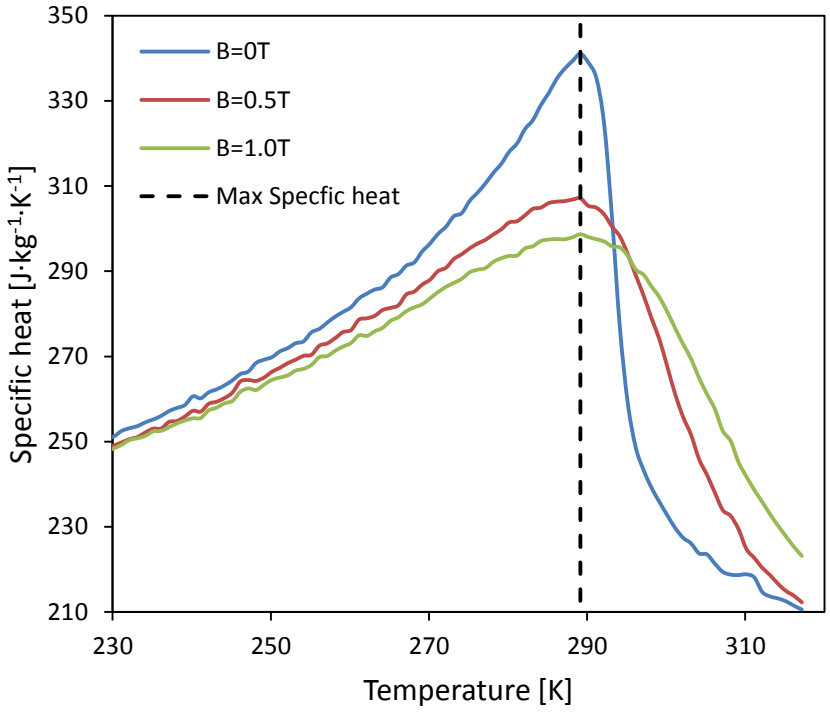

Figure 1-8 – Gadolinium (2nd order) specific heat data [8].

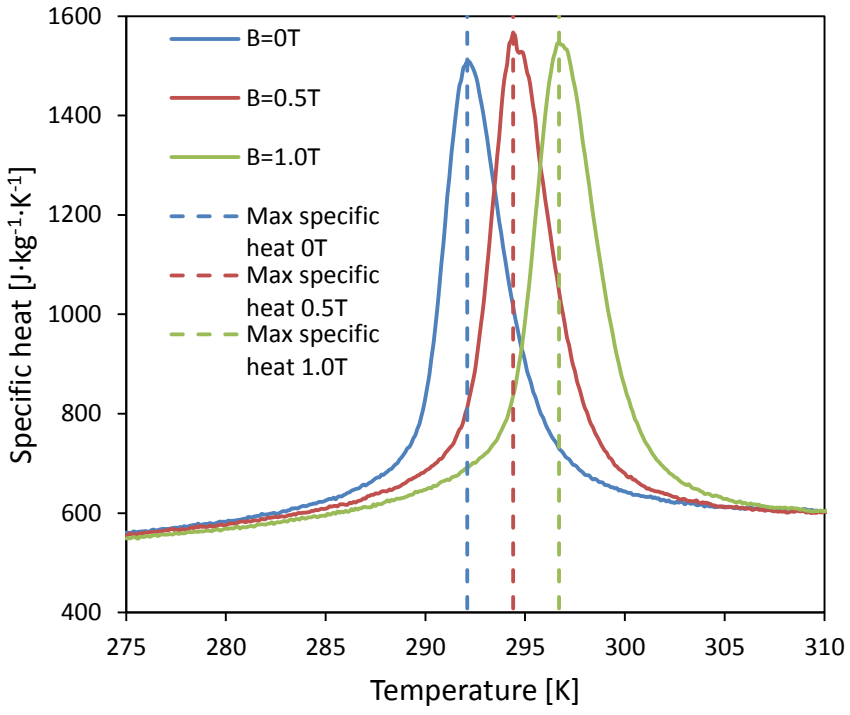

Figure 1-9 - $MnFeP_{1-x}As_x$ (1st order) specific heat data [9].

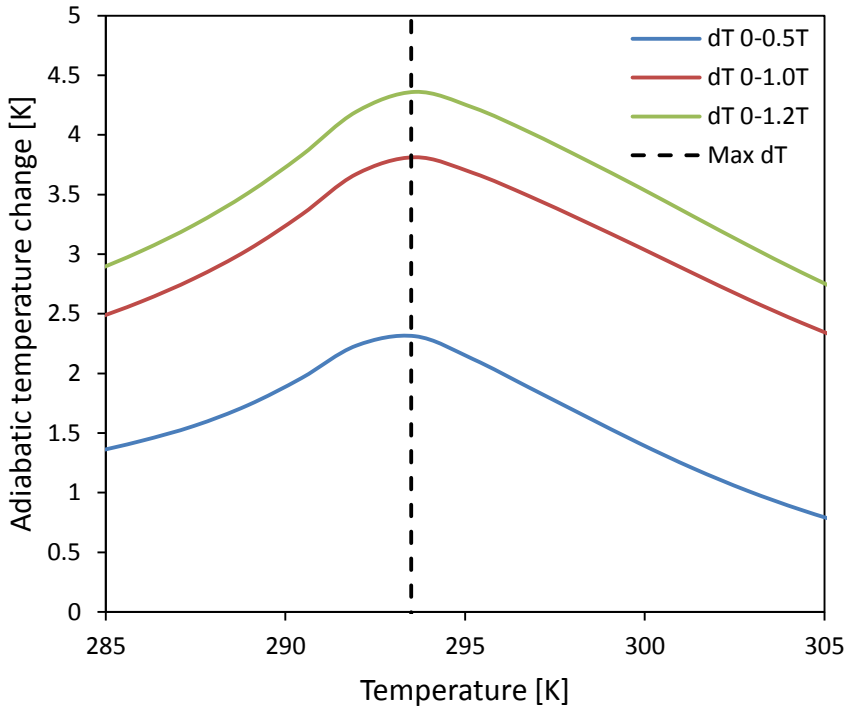

Figure 1-10 – Gadolinium ΔT_{ad} data corrected for demagnetization [10].

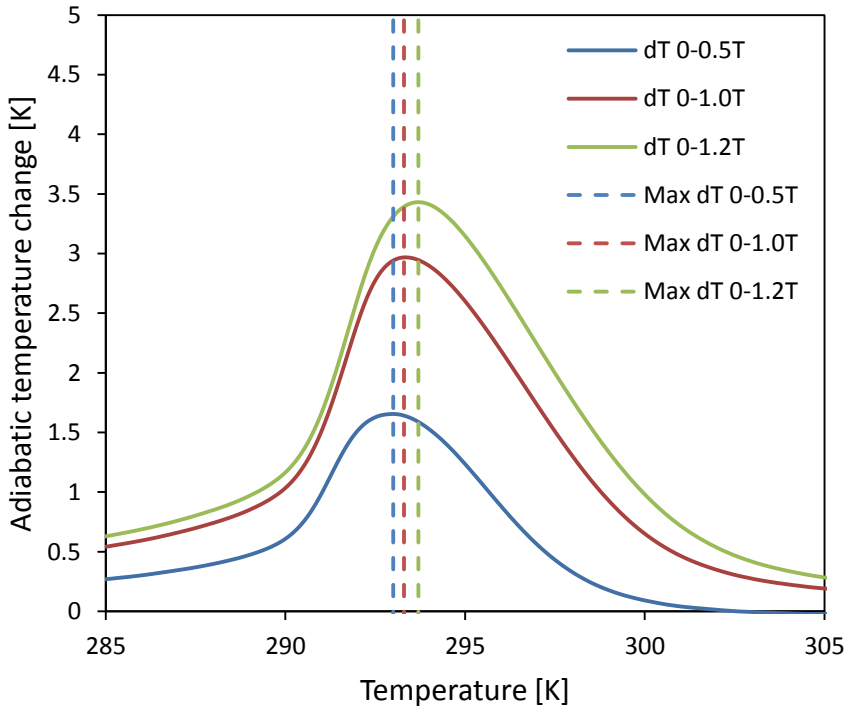

Figure 1-11 - $MnFeP_{1-x}As_x$ calculated ΔT_{ad} data corrected for demagnetization.

1.7. Investigated material: $MnFeP_{1-x}As_x$ alloys

Favourable materials in magnetic refrigeration have a large thermal response to the application of a magnetic field. $MnFeP_{1-x}As_x$ is a promising first order material for magnetic refrigeration applications because of a tunable Curie temperature [11], low material cost [12] and large magnetocaloric properties [3]. $MnFeP_{1-x}As_x$ alloys can exhibit substantial thermal and magnetic hysteresis [13]. Hysteresis is the material's property dependence on the history of processes. The magnitude of this hysteresis can be roughly tuned during material processing [13] therefore understanding the impact hysteresis has on the performance of this material is of value. Thermal hysteresis is studied because the data collection method exposes it. For the remainder of this document hysteresis will refer to thermal hysteresis.

Material data from nine $MnFeP_{1-x}As_x$ alloys are utilized in this study. By changing the relative amounts of phosphorous and arsenic the Curie temperature of the material can be shifted hotter or colder (tuned) [11]. The exact compositions of the materials tested are unknown. For each material the known data are specific heat, magnetization and ΔT_{ad} for a range of temperatures, at various applied magnetic fields and for *heating* and *cooling* processes. As described in Section 1.6 the samples are identified by the temperature of the *heating* peak specific heat temperature at zero field which is defined as the Curie temperature. The temperature where the peak ΔT_{ad} is found depends upon the change in applied field. Table 1-1 shows the Curie points and temperature of peak ΔT_{ad} for a 0 – 1.1T field change.

Table 1-1– The alloy labels and respective Curie temperatures are presented here.

Sample No.	1	2	3	4	5	6	7	8	9
Curie Temp. [K]	271	282.7	286.6	288.5	292.1	295.5	298.7	301.9	312
Temp. of the peak ΔT_{ad} [K]	272.8	284.1	288.6	291.2	294.5	298.5	301.6	304.7	315.9

1.8. Objectives

Due to the large operating space of AMR devices, modelling is critical to predict results, optimize device parameters and regenerator design, and understand the physics of the system. Modeling requires accurate material data including specific heat, magnetization and ΔT_{ad}. Adiabatic temperature change can be attained directly from measurement or indirectly through calculation from specific heat data from near zero Kelvin for a reversible material. If low temperature data is not attained, ΔT_{ad} can be calculated using specific heat and magnetization data. This study tries to answer the following question:

- Can ΔT_{ad} be accurately calculated from specific heat and magnetization data for $MnFeP_{1-x}As_x$ alloys?

To answer this question calculated values are compared against measured values to determine the accuracy of attaining ΔT_{ad} from the indirect method. The measured values are considered to be an indicator of the material's behaviour in AMR devices because the conditions during ΔT_{ad} measurements closely resemble the conditions of an AMR device [13]. The calculation procedures are validated using Gadolinium data attained from mean field theory (MFT) and data from Ames Laboratory [8].

Specific heat and magnetization data are collected under *heating* and *cooling* processes. The data are presented in terms of applied field strength, H_a, and internal field, H_{in}. These values will be presented in units of Tesla in agreement with the convention of the field of magnetic refrigeration. Four indirect ΔT_{ad} curves, presented in Table 1-2, can be calculated using combinations of specific heat data due to the thermal hysteresis of $MnFeP_{1-x}As_x$ alloys. Calculated ΔT_{ad} curves for a sample $MnFeP_{1-x}As_x$ alloy are plotted in Figure 1-12. This study attempts to answer the following secondary questions:

- Which ΔT_{ad} calculation method agrees best with measured ΔT_{ad} ?
- Does hysteresis impact the ΔT_{ad} of $MnFeP_{1-x}As_x$ alloys?

As can be seen in Figure 1-12 combining *heating* low and high field data (HH) and *cooling* low and high field data (CC) give similar ΔT_{ad} peaks with respect to each other. Combining *heating* low field data with *cooling* high field data (HC) reduces the ΔT_{ad} peak while combining *cooling* low field with *heating* high field data (CH) increases the ΔT_{ad} peak. Since high ΔT_{ad} is desirable in MR the HC curve is the worst case scenario while the CH curve is the best case scenario. Determining which indirect ΔT_{ad} curve coincides best with direct measurement could shed light on the effect of hysteresis on the behaviour of $MnFeP_{1-x}As_x$ alloys.

Table 1-2 –The ΔT_{ad} labeling convention is outlined here.

Protocol	Low field entropy curve	High field entropy curve	ΔT_{ad} label
1	Heating	Heating	HH
2	Cooling	Cooling	CC
3	Heating	Cooling	HC
4	Cooling	Heating	CH

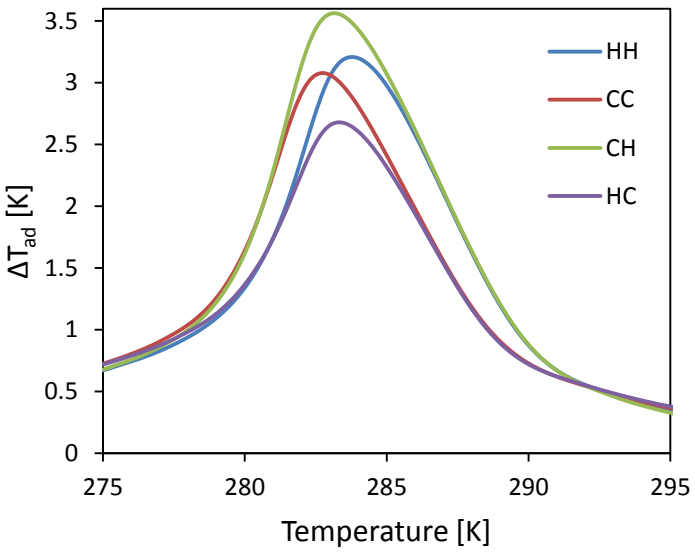

Figure 1-12 – Calculated ΔT_{ad} curves of a $MnFeP_{1-x}As_x$ alloy, sample 2.

1.9. Summary

BASF has provided specific heat, magnetization, and ΔT_{ad} data of nine $MnFeP_{1-x}As_x$ alloys that are utilized in this study to compare calculated ΔT_{ad} against measured ΔT_{ad}. Because specific heat and magnetization data are collected under *heating* and *cooling* processes and $MnFeP_{1-x}As_x$ alloys exhibit thermal hysteresis, the impact of hysteresis on ΔT_{ad} is investigated. Chapter 2 describes the theory used to calculate ΔT_{ad} from specific heat and magnetization data. Figure 1-13 gives a visual representation of calculation process. The calculation methods are validated by applying the same calculations to mean field theory (MFT) calculated Gadolinium data and comparing the results to measured Gadolinium data from AMES Laboratory. MFT, also described in Chapter 2, provides a method to calculate material properties including magnetization, specific heat, and entropy.

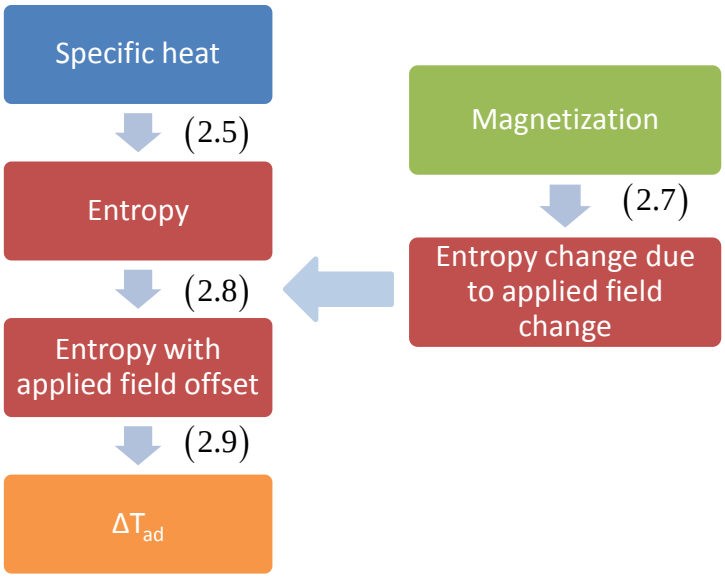

Figure 1-13 – A flow chart describing the calculation process of ΔT_{ad} from specific heat and magnetization. The colour boxes represent data while the numbers in brackets correspond to equations described in the Chapter 2 – Theory.

Experimental methods and post processing of the data are presented in Chapter 3. The Data Collection section outlines the devices used and sample specifics of the three data types (specific heat, magnetization and ΔT_{ad}). Post processing includes smoothing, magnetic field interpolation, and correcting for demagnetization.

Chapter 4 presents MFT calculated and Ames measured Gadolinium properties including magnetization, specific heat and entropy. Calculated ΔT_{ad} of $MnFeP_{1-x}As_x$ alloys are also presented and compared against measured ΔT_{ad} in Chapter 4. Metrics including peak magnitude, peak temperature, and full width at half maximum are presented to compare calculated and measured ΔT_{ad}. Chapter 5 discusses results presented in Chapter 4. Conclusions and recommendations for the future are covered in Chapter 6.

Chapter 2 – Theory

The thermodynamics linking specific heat and magnetization to ΔT_{ad} are explained. The background and method of mean field theory (MFT) are presented. From the MFT method, magnetic specific heat and entropy can be calculated. The Debye approximation and Sommerfeld theory are also presented to calculate the lattice and electronic portions, respectively, of specific heat and entropy. Combining these three theories, the total specific heat and entropy can be calculated. From entropy curves ΔT_{ad} can be determined. MFT data is used to validate calculation methods, outlined in Figure 1-13, that are used to calculate ΔT_{ad} of $MnFeP_{1-x}As_x$ alloys from specific heat and magnetization data. Demagnetization effects are also discussed.

2.1. Thermodynamics

The calculation of ΔT_{ad} from specific heat and magnetization is discussed. The path outlined by the flow chart in Figure 1-13 will be described in detail here. Specific heat at a constant parameter x is defined by [14] as

$$c_x = \left(\frac{\delta q}{dT} \right)_x \tag{2.1}$$

where δq is the quantity of heat that changes the temperature of the system by dT. In this analysis the constant parameter x is applied magnetic field H_a. Combining this definition with a reversible process $\left(ds = \delta q / T \right)$ yields

$$c_{H_a} = T\left(\frac{\partial s}{\partial T}\right)_{H_a}. \tag{2.2}$$

Rearranging Equation (2.2) gives entropy as a function of specific heat and temperature at constant applied magnetic field

$$s\left(T, H_a\right) = \int_0^T \frac{c_{H_a}\left(T', H_a\right)}{T'} dT'. \tag{2.3}$$

where T' is a dummy variable of integration. Often, specific heat measurements are taken in some finite interval of temperature, $\left(T_1, T_2\right)$. Figure 2-1 gives a visual representation of the reference entropy, s_0 and the change in entropy, Δs, relative to the reference. These two terms make up the total entropy

$$s\left(T, H_a\right) = s_0\left(T_1, H_a\right) + \Delta s\left(T_1 \to T, H_a\right) = \int_0^{T_1} \frac{c_{H_a}\left(T, H_a\right)}{T} dT + \int_{T_1}^T \frac{c_{H_a}\left(T', H_a\right)}{T'} dT'. \tag{2.4}$$

The first term in Equation (2.4) cannot be calculated because there is no data in that temperature range. However, change in entropy from T_1 to T, where $T_1 < T \le T_2$, can be calculated

$$\Delta s\left(T_1 \to T, H_a\right) = \int_{T_1}^T \frac{c_{H_a}}{T'} dT'. \tag{2.5}$$

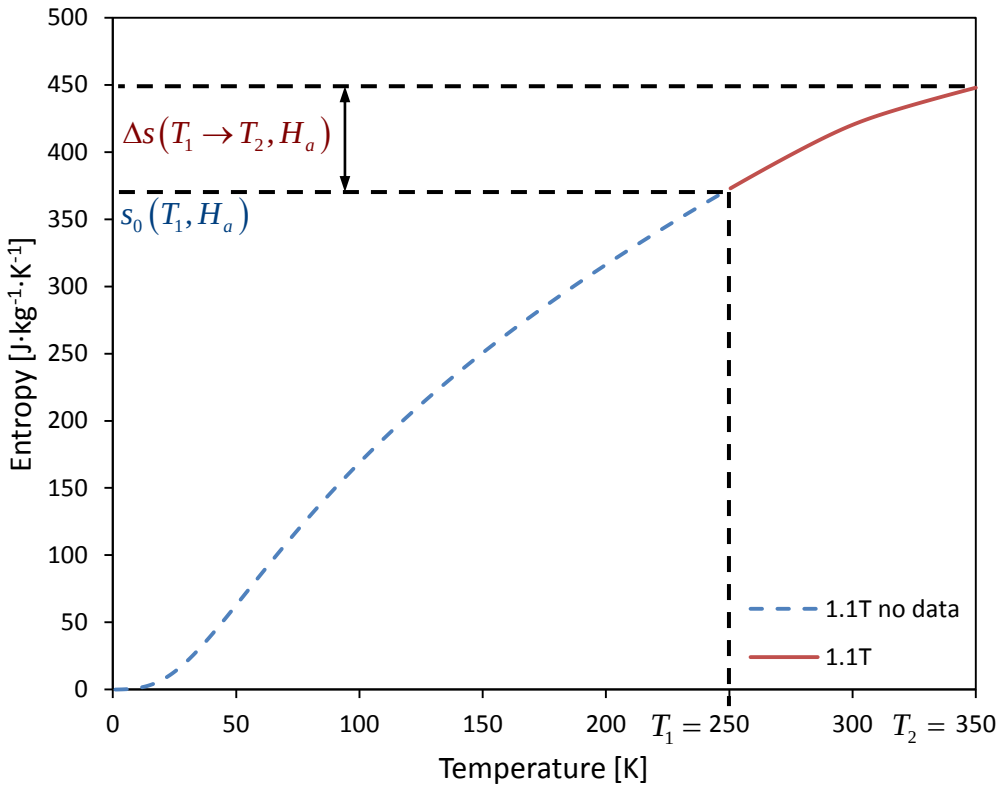

Figure 2-1 – Gadolinium entropy data obtained from integrating MFT specific heat data are plotted to illustrate the different components to the entropy integration. The red line represents entropy contribution from the Δs term that can be calculated. The blue dashed line represents the entropy contribution from the s_0 term that cannot be calculated because there is no data for this temperature range.

The above calculation is sufficient to determine the entropy difference between any two temperatures within T_1 and T_2 at a constant field. However, this analysis is concerned with the change in entropy at varying temperatures and fields. As can be seen in Figure 2-2, Equation (2.5) will yield an entropy value of zero at the lower temperature bound regardless of field strength. The following Maxwell relation can be used to find the difference in entropy between field strengths at T_1

$$\left(\frac{\partial s}{\partial H_a}\right)_T = \left(\frac{\partial m}{\partial T}\right)_{H_a}. \tag{2.6}$$

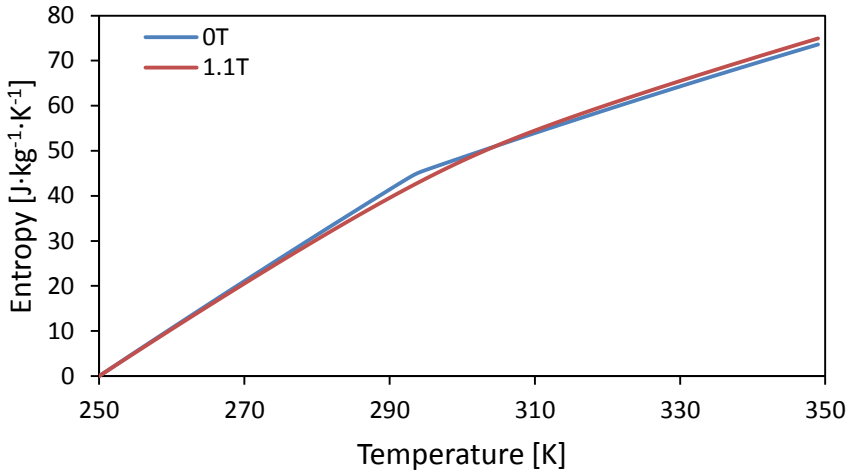

Figure 2-2 – Gadolinium change in entropy data for two field strengths using T=250K as the reference temperature. Note that at T=250K, both field strengths have the same entropy which is not possible.

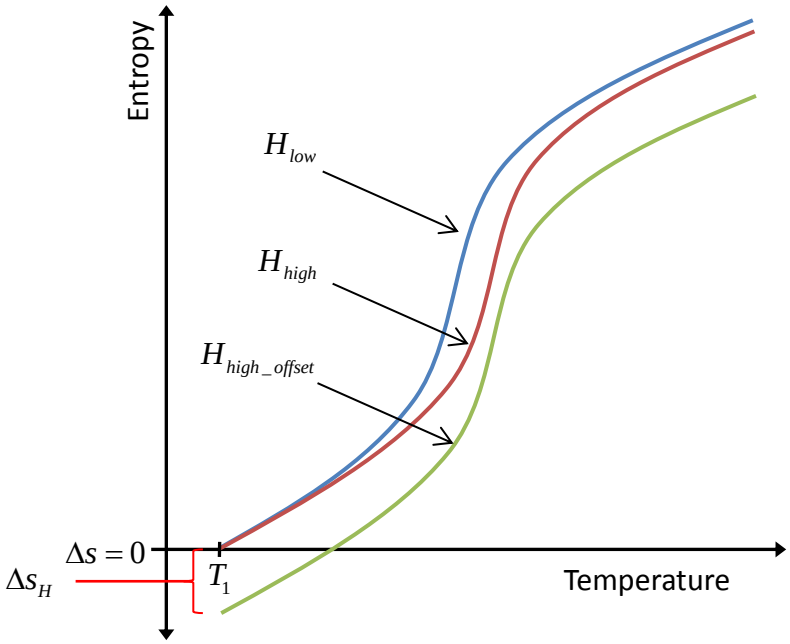

Figure 2-3 – Representative entropy curves are plotted to show the effect of adding the magnetic entropy correction, Δs_H, to the entropy calculation shown in Equation (2.8).

A derivation of the Maxwell relation in Equation (2.6) can be seen in Appendix A – Isothermal field induced entropy change derivation. Rearranging Equation (2.6) yields an

expression for the change in entropy at a constant temperature due to a change in applied magnetic field

$$\Delta s_H\left(T, H_{a,i} \to H_{a,f}\right) = \int_{H_{a,i}}^{H_{a,f}} \left(\frac{\partial m}{\partial T}\right)_{H_a} dH_a. \tag{2.7}$$

The result of adding this entropy change due to field can be seen in Figure 2-3. Combining Equations (2.5) and (2.7), and using $s\left(T_1, H_a = 0\right) = 0$ as the reference entropy, the following expressions for entropy at non zero magnetic fields is attained

$$\Delta s\left(T_1 \to T, 0 \to H_{a,f}\right) = \int_{T_1}^{T} \frac{c_{H_a}\left(T', H_{a,f}\right)}{T'} dT' + \int_0^{H_{a,f}} \left(\frac{\partial m}{\partial T}\right)_{H_a} dH_a. \tag{2.8}$$

The above equation results in an offset in non-zero field entropy curves. This offset is applied to the entire entropy curve and increases in magnitude with increasing field strength. Figure 2-4 and Figure 2-5 show the heating entropy curves of a $MnFeP_{1-x}As_x$ alloy with and without the magnetic entropy correction.

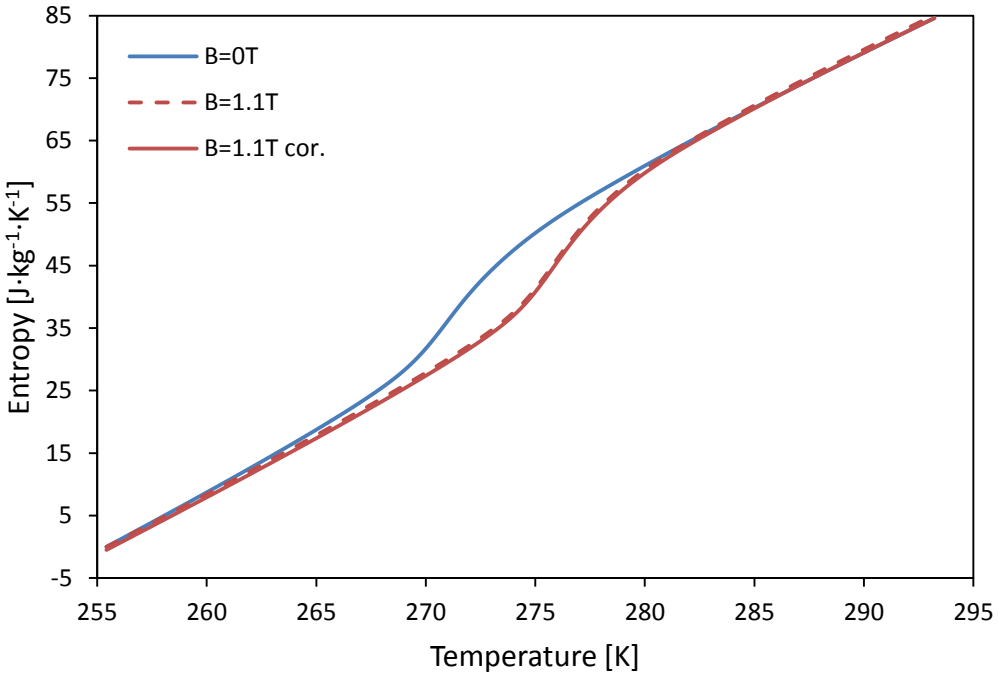

Figure 2-4 – Example $MnFeP_{1-x}As_x$ alloy entropy curves at 0T and 1.1T. The solid red line represents the corrected high field entropy curve calculated using Equation (2.8). The dashed red line represents high field entropy calculated using Equation (2.5).

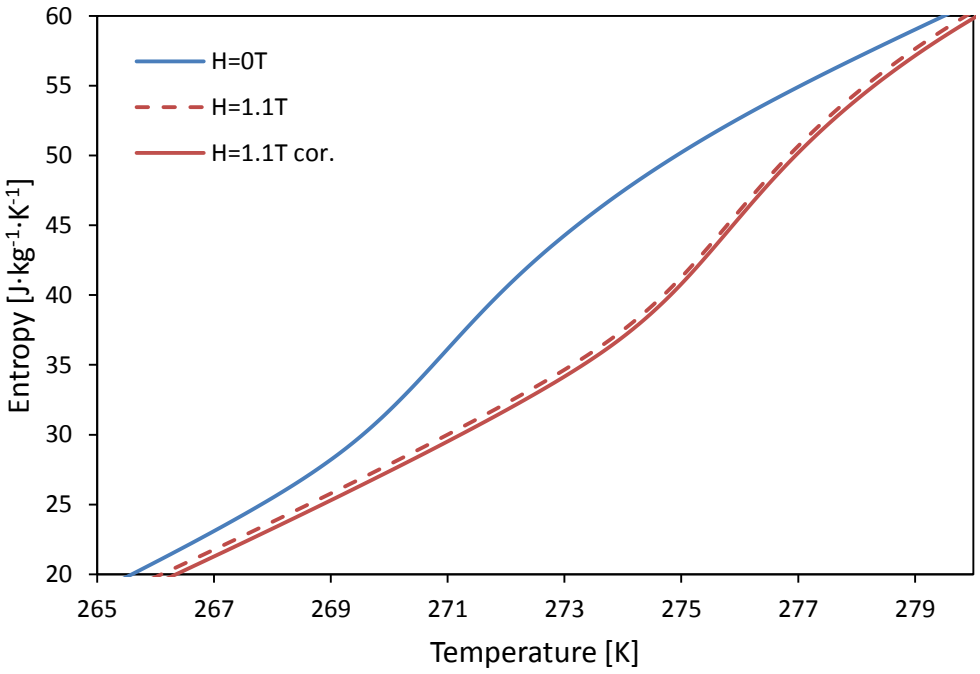

Figure 2-5 – Focussing on a smaller temperature range makes the magnetic entropy correction more visible.

ΔT_{ad} is calculated from entropy curves by determining the temperature difference along isentropes. This is done by sweeping through all entropy values and finding the temperature difference between high and low field for each isentrope

$$\Delta T_{ad}\left(T_i, H_{a,i} \rightarrow H_{a,f}\right) = T_f\left(s\left(T_f, H_{a,f}\right)\right) - T_i\left(s\left(T_i, H_{a,i}\right)\right) \tag{2.9}$$

where $s\left(T_f, H_{a,f}\right) = s\left(T_i, H_{a,i}\right)$. A schematic of this can be seen in Figure 2-6.

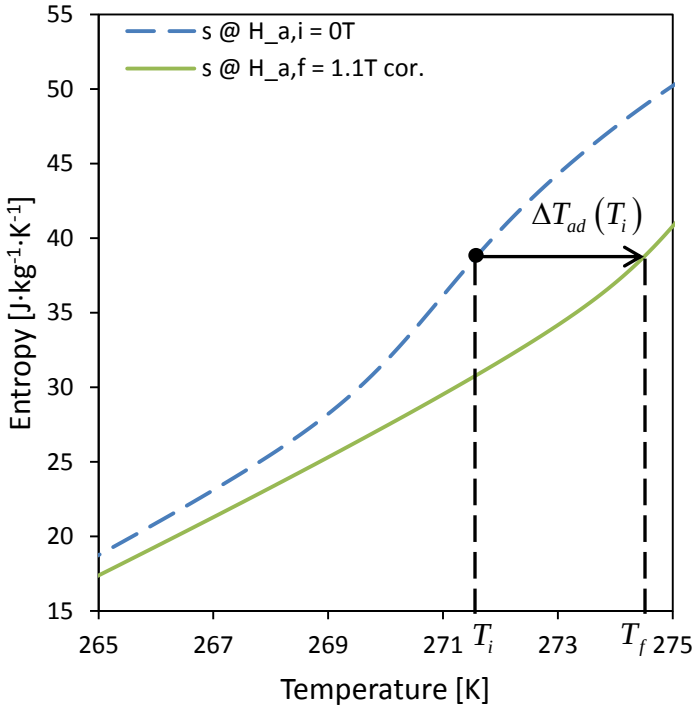

Figure 2-6 – A visual representation of the ΔT_{ad} calculation is given above. Note that the ΔT_{ad} is defined as a function of the temperature at low magnetic field.

2.2. Mean field theory

Mean field theory (MFT) uses the quantum treatment of atoms to determine the magnetization M of a sample of material containing N atoms. Provided with the quantum numbers and Curie temperature for a material, the magnetization at any given temperature and field can be determined.

For an electron orbiting around one proton under a uniform magnetic field where $\vec{B}$ runs along the z direction the Dirac Hamiltonian is [15]

$$\mathcal{H}_D = mc^2 + \frac{\vec{p}^2}{2m} - \frac{\vec{p}^4}{8m^3c^2} - e\phi + \frac{\mu_B}{\hbar}\left(2\vec{S} + \vec{L}\right)\cdot\vec{B} + \frac{e^2}{8m}\vec{B}^2\vec{r}_\perp^2 + \frac{\hbar^2}{4m^2c^2}\frac{\partial(e\phi)}{\partial r}\frac{\partial}{\partial r} - \frac{1}{2m^2c^2}\frac{1}{r}\frac{\partial(e\phi)}{\partial r}\vec{S}\cdot\vec{L} \tag{2.10}$$

which satisfies the equation

$$\mathcal{H}_D\Psi_i = \varepsilon_i\Psi_i \tag{2.11}$$

where ε_i are the eigenvalues or energy levels of the electron described by the wave functions Ψ_i. The fifth term in Equation (2.10) is the Zeeman interaction, the interaction between spin and orbital momenta with magnetic field. This is also known as the Zeeman Hamiltonian [15]

$$\mathcal{H}_{S,L} = \frac{\mu_B}{\hbar}\left(2\vec{S} + \vec{L}\right)\cdot\vec{B} \tag{2.12}$$

where $\vec{S}$ is the spin angular momentum, $\vec{L}$ is the orbital angular momentum, $\vec{B}$ is the magnetic field, μ_B is the Bohr magneton, and $\hbar$ is the reduced Planck constant or Dirac constant. Figure 2-7 shows the angular momenta associated with the spin and orbit of an electron and the associated magnetic moments. The eigenvalues of the Zeeman Hamiltonian are [15]

$$\varepsilon_{m_j} = \mu_z B = g m_j \mu_B B \tag{2.13}$$

or

$$\varepsilon_{m_j} = \mu_z \mu_0 H = g m_j \mu_B \mu_0 H \tag{2.14}$$

where μ_z is the magnetic moment component parallel to $\vec{B}$, g is the Landé factor, m_j is the z component of $\vec{J}$ (see Figure 2-8) and can range in value from $m = -j$ to $m = +j$, μ_B is the Bohr magneton, B is the magnetic field $\left(\vec{B} = B\hat{k}\right)$ and H is the magnetic field strength $\left(B = \mu_0 H\right)$. These eigenvalues are the energy levels of one electron around one proton. The Landé factor is given by [14], [15]

$$g = 1 + \frac{j(j+1) - l(l+1) + s_q\left(s_q+1\right)}{2j(j+1)}$$

$$or \tag{2.15}$$

$$g = \frac{3}{2} + \frac{s_q\left(s_q+1\right) - l(l+1)}{2j(j+1)}$$

where j is the total angular momentum quantum number, l is the orbital angular momentum quantum number, and s_q is the spin angular momentum quantum number. The subscript is to avoid confusion between spin angular momentum and mass specific entropy.

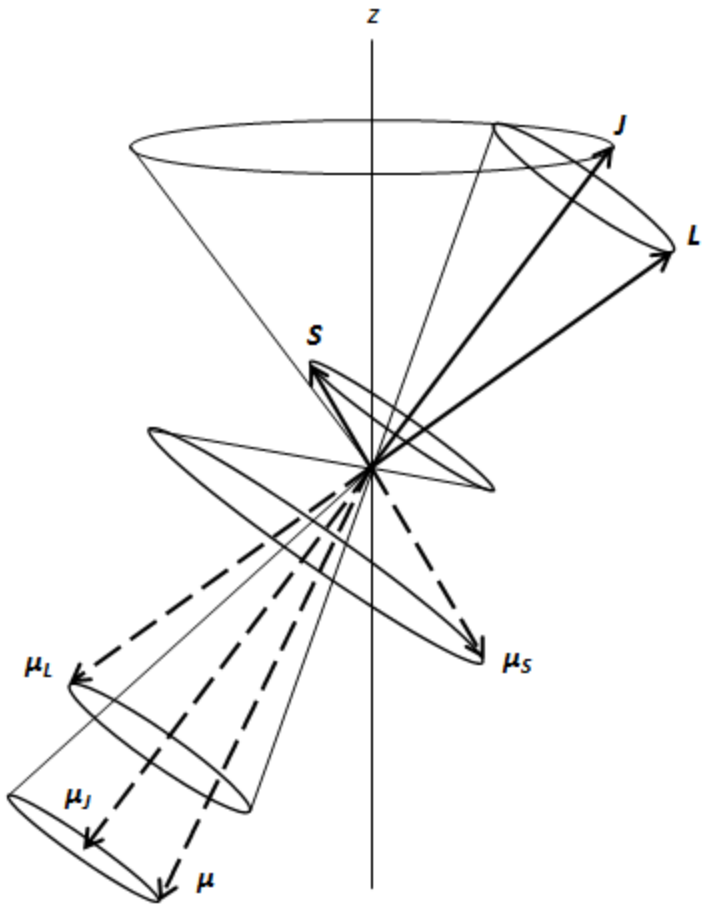

Figure 2-7 – The total angular momentum $\vec{J}$ is the sum of the orbital $\vec{L}$ and spin $\vec{S}$ angular momenta. The momentum vectors have a magnitude of $\hbar\sqrt{x(x+1)}$ where $x = s_q, l, j$. The magnetic moments associated with these momenta are also displayed. Note that μ is the total angular momentum and has a component parallel and perpendicular to $\vec{J}$, but only the parallel component contributes to the magnetic moment [15].

The above treatment is also used to find the energy level of atoms because the spin and orbital momentum of each electron contained in the incomplete shells of an atom couples to produce an effective spin and orbital momentum. Electrons contained in complete shells do not add to the effective momenta. The effective spin and orbital momenta of an atom are

$$\vec{S} = \sum_i \vec{S}_i, \tag{2.16}$$

$$\vec{L} = \sum \vec{L}_i. \tag{2.17}$$

where $\vec{S}_i$ and $\vec{L}_i$ are the spin and orbital momenta of individual electrons. Note that $\vec{S}$, $\vec{L}$ and $\vec{J}$ are vectors representing the spin, orbital, and total momenta while s_q, l and j are the spin, orbital, and total quantum numbers. They are related by the following equations

$$\left\|\vec{S}\right\| = \hbar\sqrt{s_q\left(s_q+1\right)}, \tag{2.18}$$

$$\left\|\vec{L}\right\| = \hbar\sqrt{l\left(l+1\right)}, \tag{2.19}$$

$$\left\|\vec{J}\right\| = \hbar\sqrt{j\left(j+1\right)}. \tag{2.20}$$

The relation between $\vec{L}$ and l is displayed in Figure 2-8.

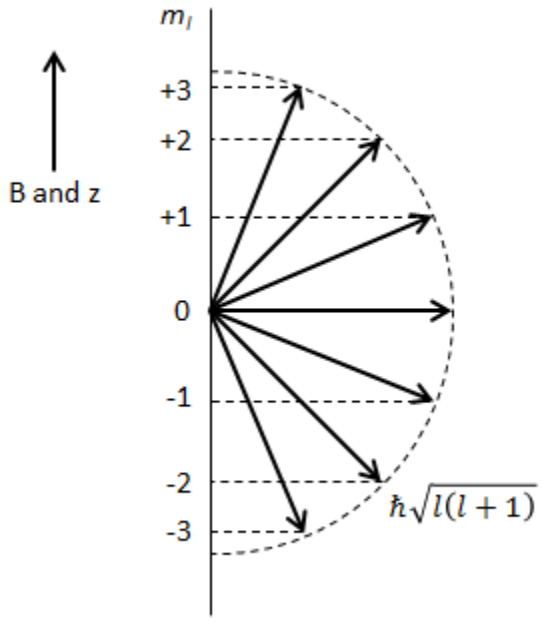

Figure 2-8 – Vector model of Gadolinium with an applied magnetic field in the z direction. The arrows represent the possible orbital momentum $\vec{L}$ vectors while the values along the m_l axis represent the associated possible values of the orbital momentum quantum number l [16].

The effective spin and orbital angular momentum quantum numbers of an atom can be determined using Hund's rules [15]:

1. Due to the Pauli Exclusion Principle two electrons can occupy the same spatial orbit with opposing spins. Orbitals are filled such that each orbit will contain one electron before any orbital contains two electrons to minimize the electron repulsion. In other words, energy is minimized when the effective spin $\vec{S}$ is maximized.
2. Electron repulsion due to orbital momentum will be lower with lower chances of electrons colliding with each other. The chance of electrons coming in contact with each other is minimized if they precess about the nucleus in the

same sense. Therefore energy is minimized when the effective orbital momentum $\vec{L}$ is maximized.

3. Spin orbit coupling is given by $\mathcal{H}_{SL} = \zeta \vec{S} \cdot \vec{L}$ where ζ is the spin-orbit parameter. The spin-orbit parameter is positive when the shell is less than half full and negative when the shell is more than half full. Therefore to minimize the spin-orbit coupling $\vec{S}$ and $\vec{L}$ are anti-parallel if the shell is less than half full, $\vec{J} = \vec{L} - \vec{S}$, and parallel if the shell is more than half full, $\vec{J} = \vec{L} + \vec{S}$.

To illustrate Hund's rules the quantum momentum numbers of a Gadolinium ion, Gd^{3+} are determined based on its incomplete electron shell, $4f^7$. The 4 indicates the principle quantum number n, the f indicates the subshell, and the 7 indicates the number of electrons contained in the subshell. Electron shell theory states that the 4f subshell can hold up to 14 electrons. Table 2-1 shows the orbitals of the 4f subshell with the 7 electrons placed based on Hund's first rule. The value of the spin quantum number s_i of an electron is +0.5 for spin up and -0.5 for spin down. The effective spin quantum number of Gadolinium is then $s_q = \sum_i s_i = \frac{1}{2}+\frac{1}{2}+\frac{1}{2}+\frac{1}{2}+\frac{1}{2}+\frac{1}{2}+\frac{1}{2} = \frac{7}{2}$. In this case all the spatial orbits are occupied by one electron so there is only one option for the value of $l = +3+2+1+0-1-2-3 = 0$. Since the orbital quantum number is zero, the third rule is irrelevant and $j = s_q = \frac{7}{2}$.

Table 2-1 – Orbital diagram of the $4f^7$ subshell of Gadolinium. The numbers represent the orbital quantum number m_l and each arrow represents an electron and its spin.

+3	+2	+1	0	-1	-2	-3
↑	↑	↑	↑	↑	↑	↑

The energy of a paramagnetic atom can then be determined using Equation (2.13) with the z component m_j of the effective total angular momentum $\vec{J}$ of the atom. The effective magnetic moment of an individual atom exposed to a uniform magnetic field is then

$$\mu_z = g m_j \mu_B. \tag{2.21}$$

The value of m_j depends on the temperature and field the atom is exposed to. The temperature determines how much energy the atom has to occupy different energy levels while the field strength determines the separation energy between ground-state and excited levels. For N atoms of a given paramagnetic material the populations of atoms occupying different energy levels at a given temperature and field can be determined by assuming a Boltzmann distribution. The probability P_i of an atom with energy ε_i is determined by [16]

$$P_i = \frac{e^{-\varepsilon_i / k_B T}}{\sum_i e^{-\varepsilon_i / k_B T}} \tag{2.22}$$

where k_B is the Boltzmann constant. The total magnetization M_T of N atoms is determined by taking the statistical average of the magnetic moment μ_z. Table 2-2 gives a summary of the different magnetization properties that can be calculated by using different parameters regarding the quantity of atoms. The statistical average is achieved by summing all magnetic states with each state weighted by the probability that it is occupied [16]

$$M_T = N \langle \mu_z \rangle = N \frac{\sum_{m=-j}^{j} -g m_j \mu_B e^{-g m \mu_B \mu_0 H / k_B T}}{\sum_{m=-j}^{j} e^{-g m \mu_B \mu_0 H / k_B T}}. \tag{2.23}$$

After a derivation that can be seen on page 12 of [16] Equation (2.23) leads to a simple expression for total magnetization with units $J \cdot T^{-1}$ or $A \cdot m^2$;

$$M_T = Ng\mu_B jB_J\left(x\right) \tag{2.24}$$

where $B_J\left(x\right)$ is the Brillouin function displayed in Figure 2-9 and given by

$$B_J\left(x\right) = \frac{2j+1}{2j}\coth\frac{\left(2j+1\right)x}{2j} - \frac{1}{2j}\coth\frac{x}{2j}. \tag{2.25}$$

The parameter x is the ratio of magnetic to thermal energy given by

$$x = \frac{gj\mu_B\mu_0 H_{tot}}{k_B T}. \tag{2.26}$$

Table 2-2 – The labeling convention of different magnetization quantities is presented below.

Label	Magnetization type	Units	Related 'N'	'N' formula	Units
M_T	Total magnetization	$A \cdot m^2$ or $J \cdot T^{-1}$	N	$\frac{N_A \cdot m_{sample}}{MW}$	*unitless*
m	Mass specific magnetization	$A \cdot m^2 \cdot kg^{-1}$	N_s	$\frac{N_A}{MW}$	$atoms \cdot kg^{-1}$
$\dot{m}$	Molar specific magnetization	$A \cdot m^2 \cdot mol^{-1}$	$\dot{N}$	N_A	$atoms \cdot mol^{-1}$

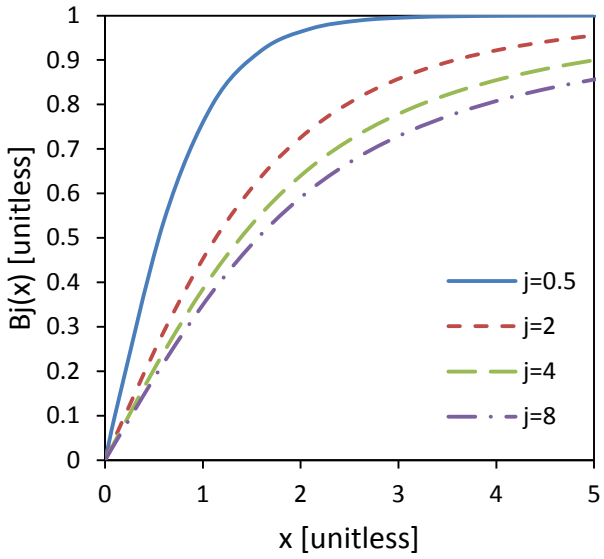

Figure 2-9 – The Brillouin function plotted against the ratio x for different j values.

The treatment above is conducted for a paramagnetic material where it is assumed that the material only experiences the applied magnetic field $H_{tot} = H$. In MFT modeling, it is assumed that ferromagnetic materials experience the following magnetic field

$$H_{tot} = H + \lambda M_T \tag{2.27}$$

where M_T is the magnetization of the system with units of $A \cdot m^2$ and λ is the mean field parameter with units of m^{-3} [15], the molecular field constant [17] or the Weiss constant [16]. The mean field parameter indicates the strength of the magnetization interaction and is given by

$$\lambda = \frac{3k_B T_c}{Ng^2 j\left(j+1\right)\mu_0 \mu_B^2}. \tag{2.28}$$

where T_c is the Curie temperature of the material. Combining equations (2.24), (2.26), (2.27), and (2.28) the ratio of magnetic to thermal energy x for a ferromagnetic material is given by

$$x = \frac{gj\mu_B\mu_0 H}{k_B T} + \frac{3jT_c}{T(j+1)} B_J(x). \tag{2.29}$$

The first term in the ferromagnetic x is the result of the applied magnetic field while the second term comes from the magnetization of the material.

2.3. Magnetic entropy and specific heat

Statistical mechanics is needed to attain an expression for the magnetic entropy of a collection of N atoms. In statistical mechanics the Helmholtz free energy is given by [15]

$$F = -k_B T \ln Z \tag{2.30}$$

where Z is the partition function that describes the statistical properties of a system in thermodynamic equilibrium and is given by

$$Z_j(x) = \sum_{m_j=-j}^{j} e^{m_j x/j} = \frac{\sinh\left(\frac{2j+1}{2j}x\right)}{\sinh\left(\frac{1}{2j}x\right)} \tag{2.31}$$

where x is the ratio of magnetic to thermal energy and is given in Equation (2.29) and j is the total angular momentum quantum number. Entropy is related to Helmholtz free energy by the following equation

$$S = -\left(\frac{\partial F}{\partial T}\right)_H. \tag{2.32}$$

Using the product rule, the chain rule and the following derivative

$$\frac{\partial}{\partial x}\ln Z = B_j(x), \tag{2.33}$$

the magnetic component of entropy for N atoms is

$$S_H(T,H) = Nk_B\left(\ln Z_j(x) - xB_j(x)\right). \tag{2.34}$$

Assuming that a material is simple magnetic (no other work modes) the specific heat at a constant magnetic field is given by

$$C_H = T\left(\frac{\partial S}{\partial T}\right)_H. \tag{2.35}$$

The relation between Helmholtz free energy and internal energy along with this definition of specific heat are used to determine the magnetic contribution to specific heat. Helmholtz free energy is related to internal energy by

$$F = U - TS. \tag{2.36}$$

Taking the partial temperature derivative of both sides of the above equation and using Equations (2.32) and (2.35) results in

$$C_H = \left(\frac{\partial U}{\partial T}\right)_H. \tag{2.37}$$

The magnetic contribution to internal energy is given by [16] (pg. 91)

$$U_H = -\int \mu_0 H_{tot}\, dM \tag{2.38}$$

where H_{tot} is defined in Equation (2.27). Substituting Equation (2.27) into Equation (2.38) leads to

$$U_H = -\mu_0 H M_T - \frac{1}{2}\mu_0 \lambda {M_T}^2. \tag{2.39}$$

Combining Equations (2.37) and (2.39) an expression for the magnetic contribution of heat capacity is found to be

$$C_H(T,H) = -\mu_0 H \frac{\partial M_T}{\partial T} - \frac{1}{2}\mu_0 \lambda \frac{\partial {M_T}^2}{\partial T} \tag{2.40}$$

where λ is the mean field parameter given by Equation (2.28). The first term in the above equation is the contribution to heat capacity due to the applied magnetic field while the second term is the contribution from spontaneous magnetization of the material.

2.4. Lattice entropy and specific heat

The lattice contribution to entropy can be determined by the Debye model [18]:

$$S_{Lat}(T) = NR\left[-3\ln\left(1-e^{-T_D/T}\right)+12\left(\frac{T}{T_D}\right)^3\int_0^{T_D/T}\frac{x^3}{e^x-1}dx\right] \tag{2.41}$$

where N is the number of atoms, R is the universal gas constant, T_D is the Debye temperature in Kelvin, and T is the temperature in Kelvin. The Debye temperature is a material property and is the highest temperature achieved due to a single normal mode of vibration. The lattice contribution to specific heat based on the Debye approximation is given by [19]

$$C_{Lat}(T) = 9Nk_B\left(\frac{T}{T_D}\right)^3\int_0^{T_D/T}\frac{e^x x^4}{\left(e^x-1\right)^2}dx. \tag{2.42}$$

2.5. Electronic entropy and specific heat

Electronic entropy and specific heat are both given by [20]

$$S_{Elec}(T) = C_{Elec}(T) = \frac{m_{sample}}{MW}\gamma_E T \tag{2.43}$$

where γ_E is the Sommerfeld or electric constant and is a material property.

2.6. First order MFT

First order MCMs can be approximated using MFT and the Bean Rodbell model. The central assumption of the Bean-Rodbell model is

$$T_c = T_0\left[1+\beta\left(\frac{v-v_o}{v_o}\right)\right] \tag{2.44}$$

where T_c is the Curie temperature, T_0 is the Curie temperature in the absence of deformation, v is the volume, v_o is the volume in the absence of exchange interactions, and β is coefficient that relates volume change to Curie temperature [21]. The free energy per unit volume including exchange interaction is given by [21]

$$\begin{aligned} G = &-\frac{3}{2}\left(\frac{j}{j+1}\right)Nk_BT_cx^2 - HM_sx + \frac{1}{2K}\left(\frac{v-v_0}{v_0}\right)^2 \\ &-Nk_BT\left[\ln\left(2j+1\right)-\frac{3}{2}\left(\frac{j}{j+1}\right)x^2-\frac{9}{20}\frac{\left[\left(2j+1\right)^4-1\right]}{\left[2\left(j+1\right)\right]^4}x^4-O\left(x^6\right)+\cdots\right]+P\left(\frac{v-v_0}{v_0}\right). \end{aligned} \tag{2.45}$$

By inserting Equation (2.44) into Equation (2.45) and minimizing the free energy with respect to volume an expression for the equilibrium volume is attained:

$$\left(\frac{v-v_0}{v_0}\right) = \frac{3}{2}\frac{j^2}{j\left(j+1\right)}Nk_BKT_0\beta x^2 - PK. \tag{2.46}$$

Recall from the previous MFT section the ratio of thermal to magnetic energy of a second order material

$$x = \frac{gj\mu_B\mu_0H}{k_BT} + \frac{3jT_c}{T\left(j+1\right)}B_J\left(x\right). \tag{2.47}$$

By substituting Equations (2.44) and (2.46) into Equation (2.47) an expression for the ratio of thermal to magnetic energy of first order materials is attained [22]:

$$x = \frac{1}{T}\left[3T_0 \left(\frac{j}{j+1} \right) B_J + \frac{g\mu_B j}{k} \mu_0 H + \frac{9}{5}\left(\frac{(2j+1)^4 - 1}{(2j+2)^4} \right) T_0 \eta B_J^3 \right] \tag{2.48}$$

where η is a parameter that controls the order of the transition and is defined as

$$\eta = \frac{5}{2} \frac{\left[4j(j+1) \right]^2}{\left[(2j+1)^4 - 1 \right]} N k_B K T_0 \beta^2 \tag{2.49}$$

where K is the compressibility factor. The last term in Equation (2.48) is a result of elastic deformation. When $\eta > 1$ the magnetic transition is first order, when $\eta < 1$ the magnetic transition is second order, and when $\eta = 0$ the elastic deformation term becomes zero and the thermal to magnetic ratio reverts back to Equation (2.47). Values of the parameter η for $MnFeP_{1-x}As_x$, are presented in [23], and a listed here in Table 2-3.

Table 2-3 – Values of parameter η for various $MnFeP_{1-x}As_x$ materials of Curie temperatures.

x	0.35	0.45	0.55	0.65
$T_c(K)$	213	240	300	332
$T_0(K)$	200	229	293	322
η	1.87	1.80	1.75	1.46

2.7. MFT Summary

A flow chart outlining the calculation method of MFT can be seen in Figure 2-10. The total entropy and specific heat of a material at a given temperature and applied magnetic field can be calculated by summing up the magnetic, lattice, and electronic components:

$$S(T,B) = S_H(T,B) + S_{Lat}(T) + S_{Elec}(T), \tag{2.50}$$

$$C(T,B) = C_H(T,B) + C_{Lat}(T) + C_{Elec}(T). \quad (2.51)$$

The magnetic component is calculated by the mean field theory, the lattice component is calculated by the Debye approximation and the electronic component is determined using the Sommerfeld model.

The Brillouin function and the magnetic to thermal energy ratio x are calculated first based on the material properties using Equations (2.25) and (2.29) respectively. Magnetization, magnetic entropy, and magnetic specific heat are then calculated using Equations (2.24), (2.34), and (2.40) respectively. The lattice entropy and specific heat are calculated using Equations (2.41) and (2.42). Using Equation (2.43) electronic entropy and specific heat are calculated. Equation (2.50) and (2.51) calculate the total entropy and specific heat. To attain the mass specific entropy and specific heat, number of atoms N is replaced with number of atoms per kilogram N_s in all specific heat and entropy formulas.

As can be seen in Figure 2-10 there are two calculation paths to calculated ΔT_{ad}. MFT can directly calculate specific heat and entropy from magnetization data. The two paths are taken in this study for two reasons. Determining entropy through two calculation paths gives confidence to both methods if both methods yield the same result. This is of value because Equation (2.8) is used to calculate entropy of $MnFeP_{1-x}As_x$ alloys from specific heat data. Calculating specific heat directly from magnetization data also gives confidence to the MFT execution since the calculated specific heat data can be compared to measured data from Ames Laboratory.

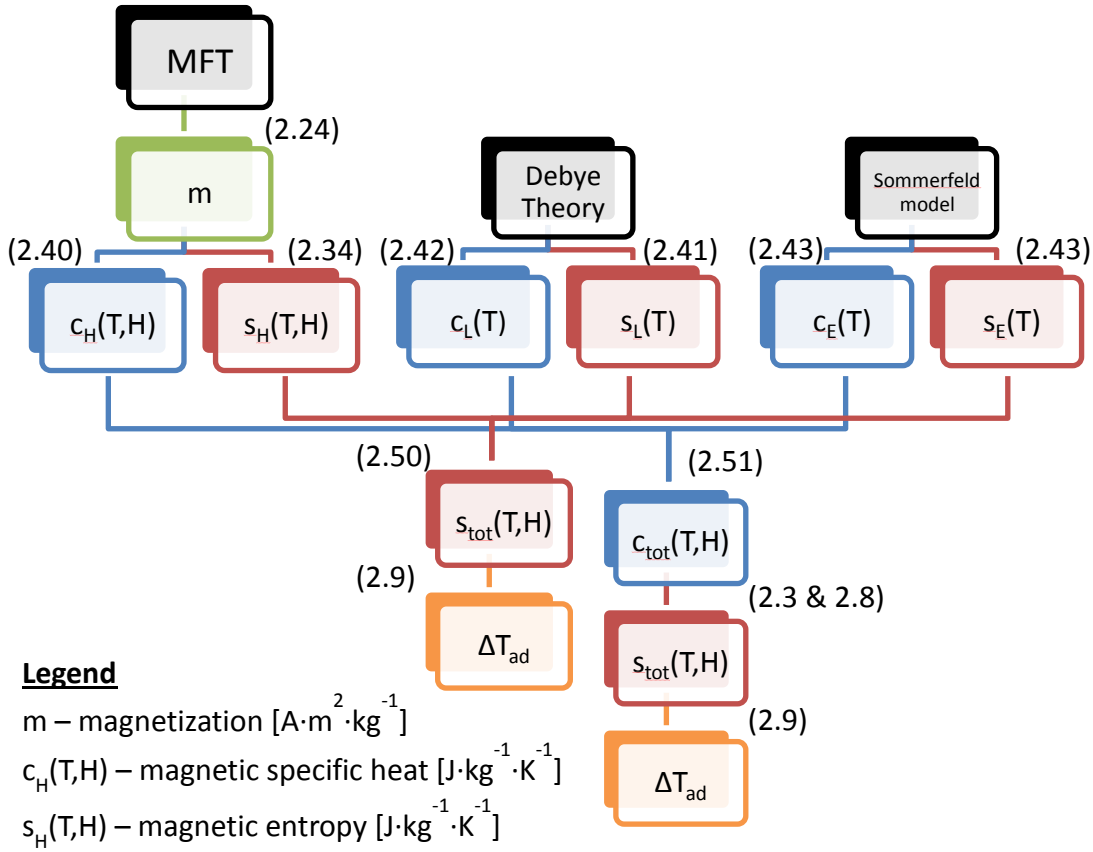

Figure 2-10 – A flow chart describing the progression of calculating material properties using MFT. This chart progression flows top to bottom. The numbers in brackets between the coloured boxes correspond to equation numbers. The equations are applied to the data in the box above to yield the resultant data in the box below. Note that all data on this flow chart is mass specific rather than total as can be seen by the lower case letters.

2.8. Demagnetization

MFT calculates material properties based on the internal field. Measured material properties are often presented in terms of applied field when the properties are functionally dependent on the internal field. To ensure all measured and calculated data is presented in terms of internal field, a correction for demagnetization must be carried out.

A material within an applied magnetic field experiences a lower internal field due to a demagnetizing field H_d . The internal field H_{in} is given by [14]

$$H_{in} = H_a - H_d. \tag{2.52}$$

Mean field theory calculates material properties based on internal field, not applied field. The demagnetizing field can be related to magnetization by

$$H_d = \mathcal{N} \cdot M \tag{2.53}$$

where $\mathcal{N}$ is the demagnetizing factor. The demagnetizing factor is unitless.

The strength of the demagnetizing field is related to the shape of the sample and its orientation relative to the magnetic field. A solid cylindrical sample with an applied magnetic field in the axial direction has a demagnetization factor of [24]

$$\mathcal{N}_l = 1 - \frac{4}{3\pi p}\left\{\left(1+p^2\right)^{1/2} \cdot \left[p^2 K\left(k\right) + \left(1-p^2\right)E\left(k\right)\right] - 1\right\} \tag{2.54}$$

where $K\left(k\right)$ and $E\left(k\right)$ are complete elliptic integrals of the first and second kind, and $p = L/2r$ is the length to diameter ratio of the cylinder. The first and second kind of complete elliptic integrals are given by [25]

$$K(k)=\int_0^{\pi/2}\frac{d\theta}{\sqrt{1-k^2\sin^2\theta}}=\int_0^1\frac{dt}{\sqrt{\left(1-t^2\right)\left(1-k^2t^2\right)}}$$
$$E(k)=\int_0^{\pi/2}\sqrt{1-k^2\sin^2\theta}\,d\theta=\int_0^1\frac{\sqrt{1-k^2t^2}}{\sqrt{1-t^2}}dt \tag{2.55}$$

where the second equations are derived by substituting $t=\sin\theta$ and k is the elliptic modulus and is given by [24]

$$k^2=\left(1+\frac{1}{4}p^2\right)^{-1}. \tag{2.56}$$

Elliptic integrals are used to calculate the arc length of an ellipse, or in the case of an ellipsoid, arc lengths. The sum of the demagnetizing factors along the three principle axes must equal one [14] therefore

$$\mathcal{N}_x+\mathcal{N}_y+\mathcal{N}_z=1. \tag{2.57}$$

Converting to cylindrical coordinates and due to symmetry the following relation between demagnetizing factors is obtained [14] (page 36)

$$2\mathcal{N}_r+\mathcal{N}_l=1. \tag{2.58}$$

By combining Equations (2.54) and (2.58) the demagnetizing factor $\mathcal{N}_r$ is determined for an applied magnetic field in the radial direction relative to a solid cylindrical sample.

A correction must be made to the demagnetizing factor if a sample is made of up particulate. According to [14] a sample of particles packed isotropically with a packing fraction f in a sample holder with a demagnetizing factor $\mathcal{N}$ will have a demagnetizing factor of

$$\mathcal{N}_p\simeq\frac{1}{3}+f\left(\mathcal{N}-\frac{1}{3}\right). \tag{2.59}$$

The packing fraction of a sample of particles within a volume is the fraction of that volume occupied by material. The specific corrections executed on the specific heat and magnetization data of the $MnFeP_{1-x}As_x$ alloys are explained in Section 3.4, Section 3.5, and Section 3.6.

2.9. Summary

The calculation of ΔT_{ad} from specific heat and magnetization assuming a reversible process is outlined in this chapter. MFT combined with the Debye and Sommerfeld models provide a way to simulate material data including magnetization, specific heat, and entropy.

MFT is used to calculate Gadolinium material properties. The implementation of MFT is validated by comparing the MFT results to measured specific heat and ΔT_{ad} data. These results are presented in Section 4.1. The same methods used calculate ΔT_{ad} from MFT calculated Gadolinium specific heat and magnetization data are also used on $MnFeP_{1-x}As_x$ alloy data. The confidence in the implementation of three calculations required to calculate ΔT_{ad} from specific heat and magnetization data is therefore improved. These calculations are described in Equation(2.7), Equation (2.8) and Equation (2.9).

The next chapter presents the experimental methods used to collect the raw specific heat, magnetization and ΔT_{ad} data of $MnFeP_{1-x}As_x$ alloys. Post processing methods including smoothing, interpolation, and demagnetization correction are presented in the next chapter.

Chapter 3 – Methods

Measured specific heat, magnetization, and ΔT_{ad} data are provided by BASF for nine alloys in the $MnFeP_{1-x}As_x$ family. Experimental methods including measurement devices, sample geometries, and uncertainties are presented. Sample geometries are required to determine the internal field experienced by the sample. Measurement uncertainties are necessary as they form the basis on which the calculated ΔT_{ad} uncertainties are determined.

Post processing methods are described which include smoothing, interpolation, and correcting for demagnetization. Smoothing outlined in this chapter is necessary to reduce the noise in magnetization and ΔT_{ad} data. To ensure all data sets cover the same internal field range interpolation and demagnetization corrections are applied.

Hysteresis is defined and presented in this chapter. The hysteresis paths of low and high field entropy data that yield four different calculated ΔT_{ad} curves are described. The calculated ΔT_{ad} curves will be compared to measured data in Chapter 4.

The propagation of uncertainties through the ΔT_{ad} calculation process is presented. It is important to track this to ensure the errors from the original measurement do not translate to uncertainties larger than the differences between the different calculated ΔT_{ad} curves or the differences between measured and calculated curves.

Four flow charts outlining the processes imparted on each data type involved in this study are presented. The processes presented in these flow charts are described in detail in this chapter. The coloured boxes represent data and the numbers in brackets between the boxes correspond to Chapter Sections that describe the process executed on

the data. Figure 3-1 displays a blue flow chart outlining the processes executed on specific heat data. Figure 3-2 displays a similar green flow chart outlining the processes executed on magnetization data. The processes executed on entropy data, calculated from specific heat data, are displayed in the red flow chart in Figure 3-3. Finally, the processes conducted on calculated ΔT_{ad} data are displayed in an orange flow chart in Figure 3-4. These flow charts provide more detail than the master flow chart presented in Figure 1-13. The flow charts are colour coded to relate to Figure 1-13.

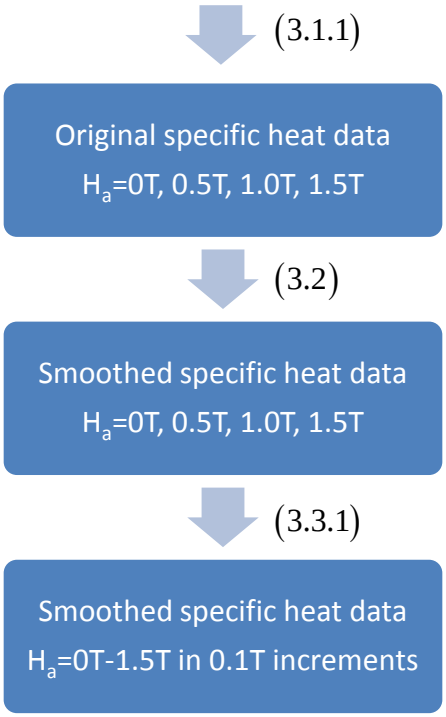

Figure 3-1 – A flow chart describing the processing of the specific heat data is presented. The numbers in brackets are related to sections of this document that explain the processes.

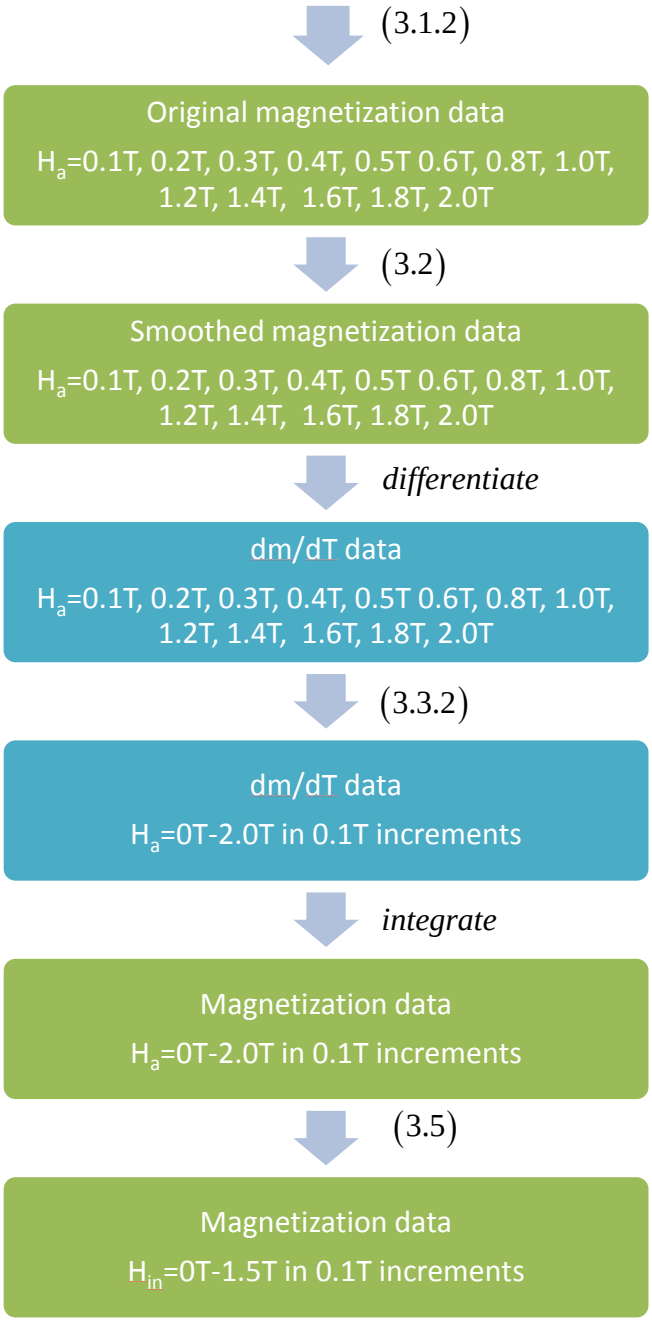

Figure 3-2 – A flow chart describing the processing of the magnetization data is presented. The numbers in brackets are related to sections of this document that explain the processes. The differentiation and integration of magnetization data with respect to temperature do not have a sections devoted them.

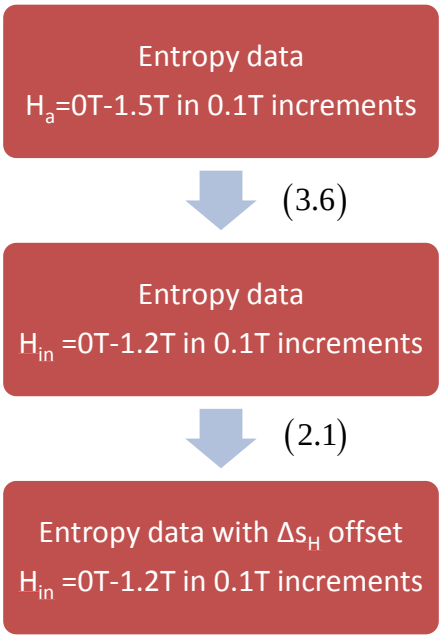

Figure 3-3 – A flow chart describing the processing of the entropy data is presented. The numbers in brackets are related to sections of this document that explain the processes.

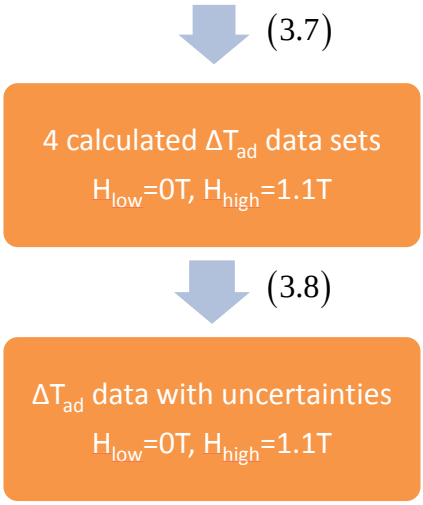

Figure 3-4 – A flow chart describing the processing of the ΔT_{ad} data is presented. The numbers in brackets are related to sections of this document that explain the processes.

3.1. Data Collection

Material data consisting of specific heat, magnetization and ΔT_{ad} for nine different $MnFeP_{1-X}As_X$ alloys are analysed. Because this material exhibits thermal hysteresis, material properties are measured for both *heating* and *cooling* processes. A cooling process is one where the ambient temperature is initially set higher than the Curie temperature of the material and slowly cooled to a temperature lower than the Curie temperature while measurements are taken. A heating process is the opposite. Specific heat measurements are taken by a custom BASF magnetic differential spanning calorimeter device (mDSC), magnetization is measured by a commercial vibrating sample magnetometer (VSM) and ΔT_{ad} is measured by a custom BASF ΔT_{ad} device. The various devices, samples and measurement techniques are described in the following sections.

3.1.1. Specific heat

A differential scanning calorimeter (DSC) measures specific heat. A simplified schematic of a DSC is displayed in Figure 3-5. In this application it is used to measure the specific heat at fixed applied fields under heating and cooling processes. A sample is placed in a test pan, while the other test pan is left empty as a reference. Each pan has a computer controlled heater and a thermocouple to monitor the temperature. The computer uses these heaters to control the rate of change of temperature of both pans. The rate of change of temperature is kept constant for both pans and for the entire process (for example 10 degree Celsius per minute). The DSC measures the difference in heat flow required to keep the temperature change rate the same for both the sample and the

reference at each temperature. Specific heat is determined by dividing the difference in heat flow by the rate of change in temperature [26].

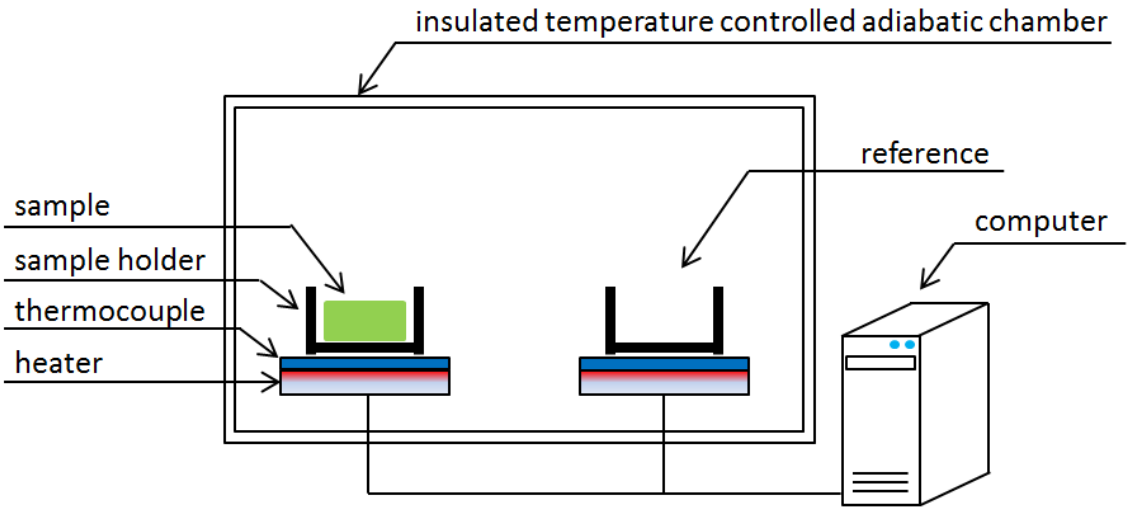

Figure 3-5 – A schematic of a DSC. The computer uses the data from the thermocouples to ensure that both the sample and reference are changing temperature at the same rate by adjusting the power delivered to each heater.

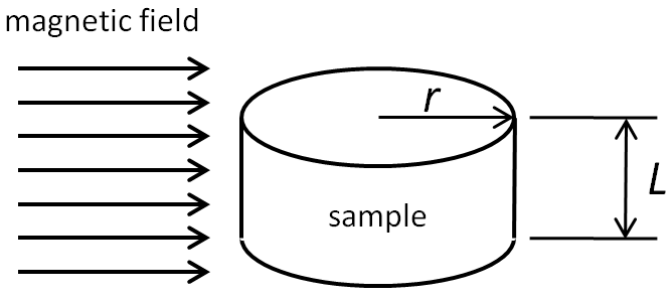

Figure 3-6 – Sample-field orientation of in-field specific heat and magnetization measurements.

Specific heat measurements are taken with a mDSC developed by INRIM for BASF. A sample can experience zero to 1.5 Tesla in this device. Typically the measured field strengths are 0.5 T, 1.0 T, and 1.5 T. Figure 3-6 shows the orientation of the

magnetic field lines relative to the cylindrical samples. The field is kept constant while the temperature is swept in a heating or cooling process at 3 Kelvin per minute. Each sample is initially thermally cycled up and down twice from -80 °C degrees Celsius to 120 °C at a rate of ±10 °C/min to avoid the *virgin effect*. The virgin effect is a name given to describe the different behaviour this material exhibits during the first cycle. The first cooling process for example can yield a specific heat peak location up to 30-40 Kelvin lower and a broader transition than subsequent cooling measurements. Cylindrical aluminum crucibles, see Figure 3-7, of internal length 1.2 mm and internal radius 2.3 mm house the samples. The magnetic field lines run in the radial direction relative to the cylindrical sample holder as can be seen in Figure 3-9. Samples are composed of 50±2 mg of crushed particles less than 150 microns in size. The reported relative uncertainty in the specific heat measurements is four percent [9].

Figure 3-7 – From left to right the above image shows a dime, the mDSC sample holder, and the mDSC sample lid. The lid sits on top of the crucible in the orientation shown such that it reduces the volume of the crucible by a small amount.

3.1.2. Magnetization

The VersaLab VSM measures magnetization. The VSM was invented by Simon Foner in 1955 [27]. In this application it is used to measure the magnetization at constant

fields while the temperature is swept from cold to hot and then reversed at one Kelvin per minute. Magnetization samples are composed of 15 mg of crushed particles less than 150 microns in size. The samples are placed in a cylindrical sample holder which is placed in the magnetic field volume. The cylindrical sample has a length of 1 mm and a radius of 1.25 mm. The magnetic field lines are oriented in the radial direction relative to the cylindrical sample, see Figure 3-6. A picture of the sample holder can be seen in Figure 3-8. Pick-up coils surround the sample and are also within the magnetic field volume. As the sample is vibrated (moved up and down) the stray magnetic field from the induced magnetization changes and is measured by the pick-up coils in terms of induced voltage/current due to Faraday's Law of Induction. This current is proportional to the magnetization of the sample. The accuracy of the instrument is listed at better than 1 percent [28].

Figure 3-8 – The above image shows (from left to right) a connected VSM sample holder, a disconnected VSM sample holder, and a dime. The pink material in the connected sample holder illustrates how the sample would be contained in the VersaLab VSM.

3.1.3. Adiabatic temperature change

A BASF ΔT_{ad} device measures adiabatic temperature change. Two sample plates, approximately 10 mm by 5 mm by 1 mm, are required to take a sample measurement (Figure 3-9). A centre groove is cut into both plates along the 10 mm side to make room for a type E thermocouple that is sandwiched between the two plates to measure the temperature change of the sample. The thermocouple is glued in place with a minimal amount of thermo-conductive epoxy glue. Four layers of packing tape insulate the assembly. The sample orientation relative to the magnetic field lines can be seen in

Figure 3-9. The sample is oriented in this position to minimize demagnetization effects. Sample assemblies are moved in and out of a 1.1T field at a cycle frequency of 0.1 Hz. At the same time the temperature is swept from $T < T_C$ to $T > T_C$ (*heating*) and then $T > T_C$ to $T < T_C$ (*cooling*) a rate of 0.5 Kelvin per minute using a temperature controlled chamber. The ΔT_{ad} peak location and magnitude attained from the BASF device has standard deviations of 0.5 K and 0.2 K respectively.

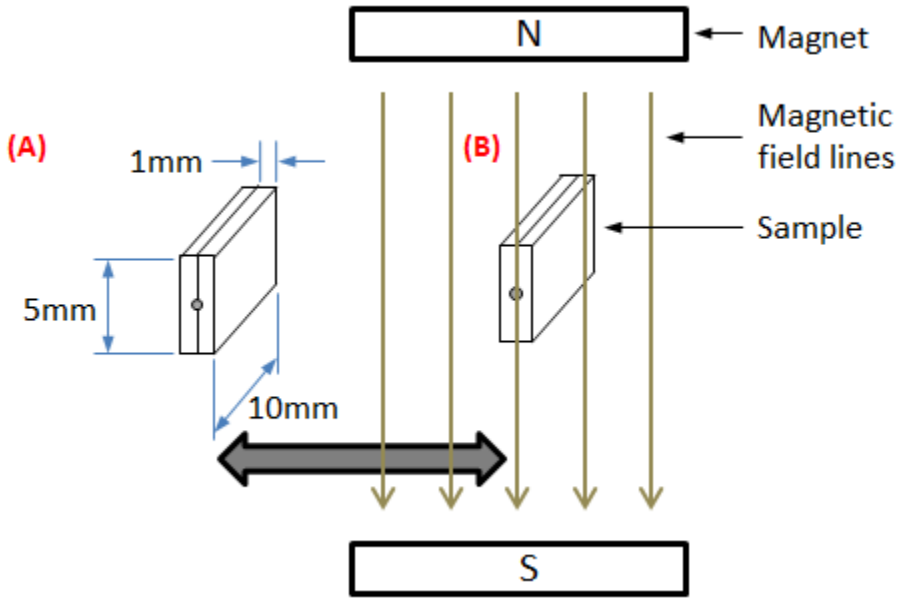

Figure 3-9 – Schematic of sample size and orientation in BASF ΔT_{ad} device to measure adiabatic temperature change. The magnetic field lines are parallel to the 5 mm side of the sample. (A) represents the low field position and (B) represents the high field position.

3.2. Smoothing

To reduce noise a smoothing spline is applied to magnetization and measured ΔT_{ad} data sets. Specific heat data are not smoothed because it is integrated to attain entropy and the effects of noise are reduced. Magnetization data is differentiated which is

more sensitive to noise; therefore it is smoothed. Adiabatic temperature change data is smoothed to improve the ease in determining data metrics which include the magnitude of the peak, the temperature of the peak, and the full width half maximum.

The smoothing spline is constructed in MATLAB by minimizing

$$p\sum_i w_i\left(y_i - s\left(x_i\right)\right)^2 + \left(1-p\right)\int\left(\frac{d^2 s}{dx^2}\right)^2 dx \tag{3.1}$$

where p is the smoothing parameter, w is the weighting factor, y_i is the original dependent variable, x_i is the independent variable, and s is the smoothed data. The smoothing parameter is defined between 0 and 1. A smoothing parameter of $p = 0$ produces a least squares straight line fit to the data while a value of $p = 1$ produces a cubic spline that runs through each original data point. No weighting is used so $w_i = 1$ for all points.

A smoothing parameter of 0.95 is used for magnetization data. This number is determined by trial and error. A smoothing parameter greater than 0.95 is not sufficient to reduce the noise while a smoothing parameter less than 0.95 reduces the slope of the magnetization curves yielding lower peaks in the magnetization temperature derivative data. The percent difference between smoothed and raw data for a sample material that is representative of all nine materials is displayed in Figure 3-10. The percent difference is calculated using the following relationship

$$percent\_diff = 100 \cdot \frac{m_{smoothed} - m_{raw}}{m_{raw}}. \tag{3.2}$$

As can be seen in Figure 3-10 two data points have a percent difference greater than 1% which is considered acceptable since each field strength has over 500 data points and

there are 13 field strengths per sample. The smoothing therefore has a small effect on the magnetization data as shown in Figure 3-10, but as can be seen in Figure 3-11 and Figure 3-12 the difference in the temperature derivative of raw and smoothed magnetization data is significant.

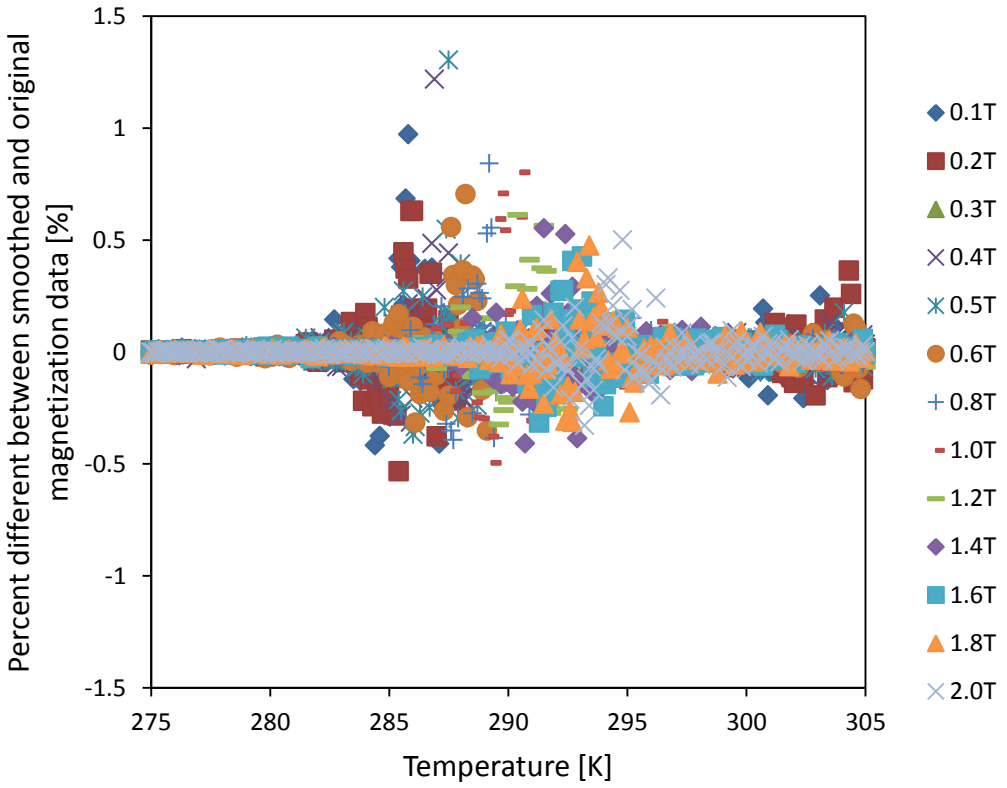

Figure 3-10 – The percent difference between smoothing and raw heating magnetization data for a sample material is presented here.

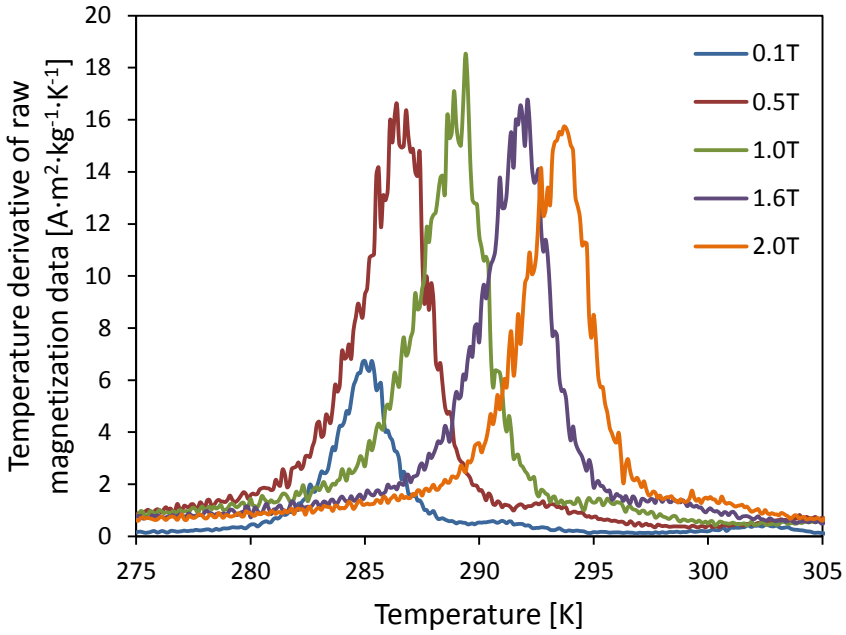

Figure 3-11 – The temperature derivative of raw magnetization data.

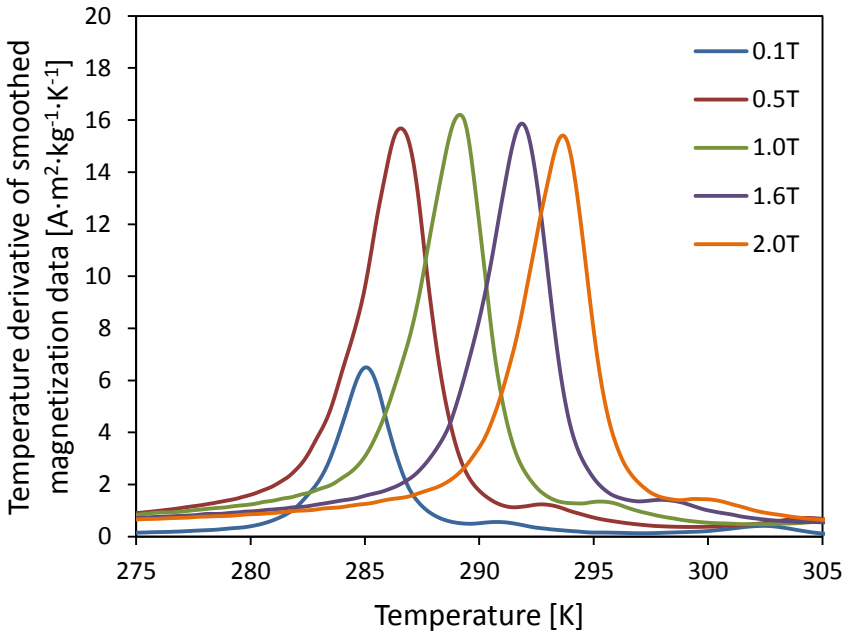

Figure 3-12 – The temperature derivative of smoothed magnetization data.

The measured ΔT_{ad} data is smoothed to enable the calculation of magnitude and location of the temperature change peak as well as the full width half maximum value (FWHM). A smoothing parameter of 0.99 is used. A higher smoothing parameter is used for adiabatic temperature data to avoid reducing the peak of the curves. Figure 3-13 and Figure 3-14 show the raw and smoothed ΔT_{ad} data and the percent difference between the two. As can be seen in Figure 3-13, the percent differences between raw and smoothed data here are larger than with the magnetization data. This is due to noisier data and the smaller magnitude of ΔT_{ad} values.

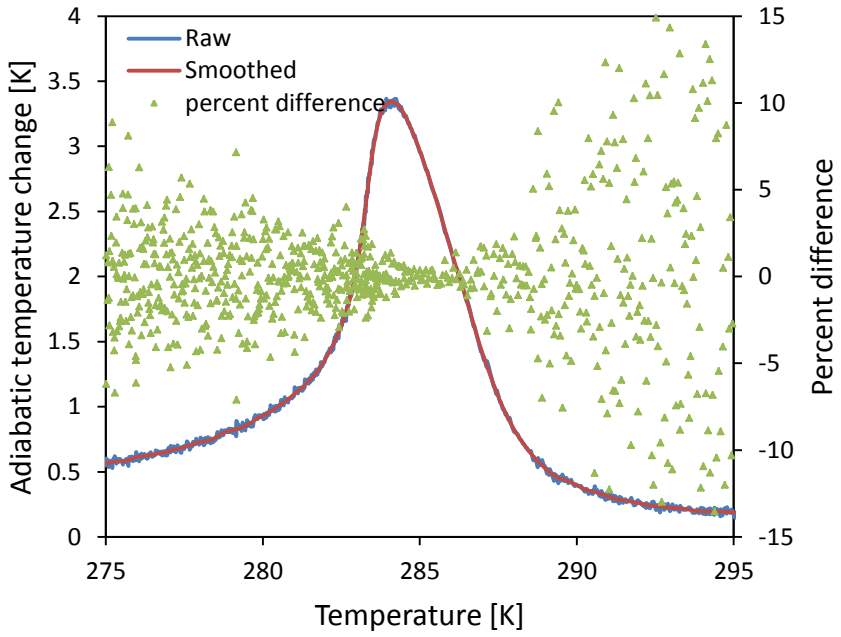

Figure 3-13 – Raw and smoothed heating adiabatic temperature change data are plotted. The percent difference between the raw and smoothed data are also plotted.

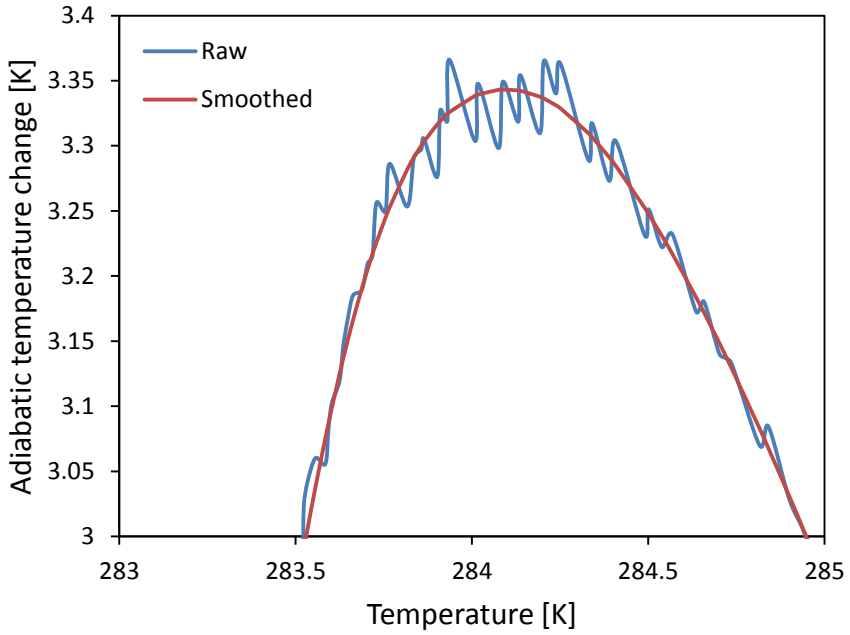

Figure 3-14 – A closer look at the peak adiabatic temperature change data shows the necessity of smoothing. Without smoothing, determining the temperature and magnitude of the peak would be difficult.

3.3. Interpolation

Specific heat, magnetization and ΔT_{ad} data do not cover the same applied magnetic fields. Specific heat data are collected at applied fields of zero, 0.5, 1.0 and 1.5 Tesla. Magnetization data are collected at applied field strengths of 0.1, 0.2, 0.3, 0.4, 0.5, 0.6, 0.8, 1.0, 1.2, 1.4, 1.6, 1.8 and 2.0 Tesla. The ΔT_{ad} measurement is conducted with an applied magnetic field that varies between zero Tesla and 1.1 Tesla. Calculating ΔT_{ad} requires both specific heat and magnetization data sets and therefore they both are required to cover the same applied magnetic fields. Once the data are initially smoothed linear interpolation is used to fill the gaps in the data sets so that they cover the same applied magnetic fields. Data set specifics can be seen in Table 3-1.

Table 3-1 – Applied magnetic field strengths

	Specific heat	Magnetization	Adiabatic temperature change
Applied field strengths [T] $\mu_0 H_a$	0, 0.5, 1.0, 1.5	0.1, 0.2, 0.3, 0.4, 0.5, 0.6, 0.8, 1.0, 1.2, 1.4, 1.6, 1.8, 2.0	0 – 1.1
Interpolated applied field strengths [T] $\mu_0 H_a$	0, 0.1, 0.2, 0.3, 0.4, 0.5, 0.6, 0.7, 0.8, 0.9, 1.0, 1.1, 1.2, 1.3, 1.4, 1.5	0, 0.1, 0.2, 0.3, 0.4, 0.5, 0.6, 0.7, 0.8, 0.9, 1.0, 1.1, 1.2, 1.3, 1.4, 1.5, 1.6, 1.7, 1.8, 1.9, 2.0	0 – 1.1

3.3.1. Specific heat interpolation

Specific heat data are interpolated to get a 0.1 Tesla resolution on applied magnetic fields from zero to 1.5 Tesla. The data are interpolated using a temperature offset defined by the difference in peak specific heat temperatures of the two applied field specific heat curves. Figure 3-15 gives a visual of the temperature offset interpolation. This offset is necessary due to the shifting of the peak with increasing magnetic field. Sample specific heat data at the four original applied field strengths are displayed in Figure 3-16. In accordance with other results [7], there is a linear variation of peak temperature with applied field.

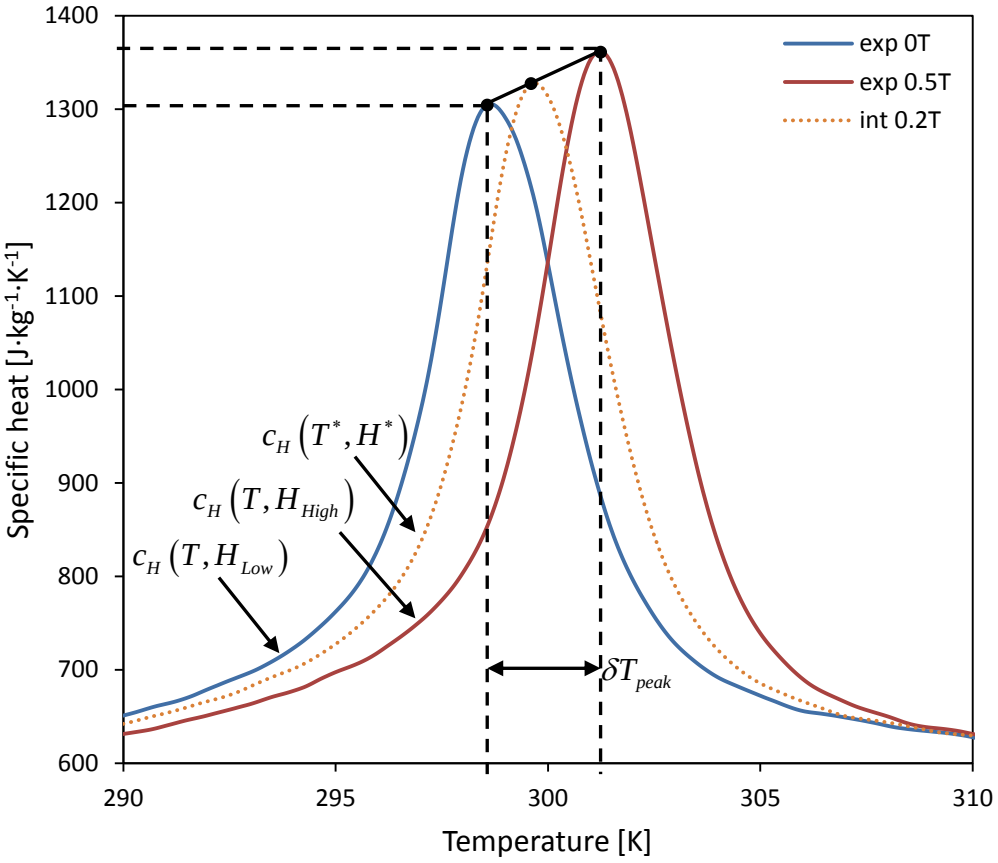

Figure 3-15 – The blue and red line represent measured specific heat data while the orange dotted line represents specific heat data at an interpolated field strength using the temperature offset interpolation method. δT_{peak} is the temperature offset and is defined as the difference in temperature of the high and low field specific heat peaks.

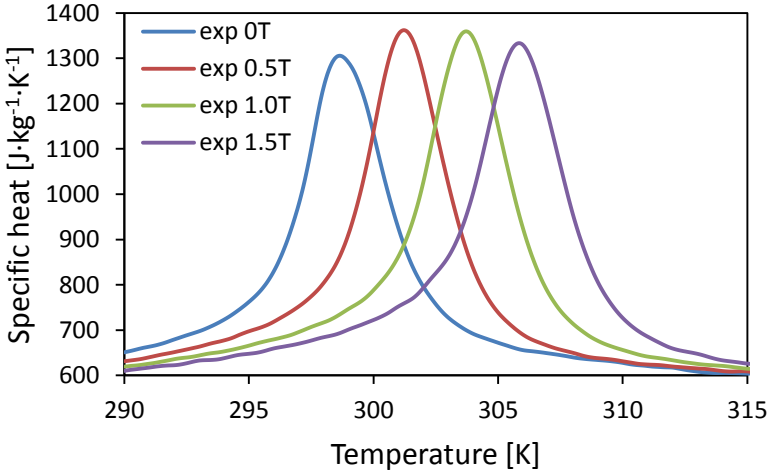

Figure 3-16 – Sample heating specific heat data.

A linear peak shift with field is assumed for all alloys. Linear interpolation between two magnetic fields using a temperature offset yields expected results [7]. The temperature offset, δT_{peak}, is defined as the difference the specific heat peaks at high and low field. δT_{peak} is used as a reference for the offset interpolation. Specific heat data can be interpolated to attain data at any applied field within the range of original applied field strengths. The interpolated magnetic field strength can be given by

$$H^* = H_{Low} + f \cdot \left(H_{High} - H_{Low} \right) \tag{3.3}$$

where H_{Low} is the low field, H_{High} is the high field, and f is the chosen fraction and can range between zero and one. The difference between the low field and the interpolated field is defined here as

$$\delta H = f \cdot \left(H_{High} - H_{Low} \right). \tag{3.4}$$

The specific heat can then be calculated for the new field strength using this following relation

$$c_H \left(T^*, H^* \right) = c_H \left(T, H_{Low} \right) + \delta H \left(\frac{c_H \left(T + \delta T_{peak}, H_{High} \right) - c_H \left(T, H_{Low} \right)}{H_{High} - H_{Low}} \right) \tag{3.5}$$

where T^* is the temperature associated with the interpolated data. The interpolated temperature, T^*, is determined using the following relationship

$$T^* = T_{Low} + f \cdot \delta T_{peak} \tag{3.6}$$

where T_{Low} is the temperature of the low field specific heat data and f is the same fraction mentioned earlier and is given by

$$f = \frac{H^* - H_{Low}}{H_{High} - H_{Low}}. \tag{3.7}$$

The above interpolation is completed four times between each applied field data set to attain specific heat data with applied field resolution of 0.1 Tesla. Focussing on the interpolations between zero and 0.5 Tesla the result is a matrix of specific heat data that has columns of constant magnetic field (0, 0.1, 0.2, 0.3, 0.4, and 0.5) but no longer isothermal rows, see Figure 3-17. This problem is solved using the MATLAB function interp1 which requires an x and y array and an X value and outputs the resultant Y based on the xy relationship. In this case the x-array is the new temperature array, the y-array is the new specific heat array and the X values were the original temperature array. Figure 3-17 gives a visual representation of the complete offset interpolation procedure. The result can be seen in Figure 3-18.

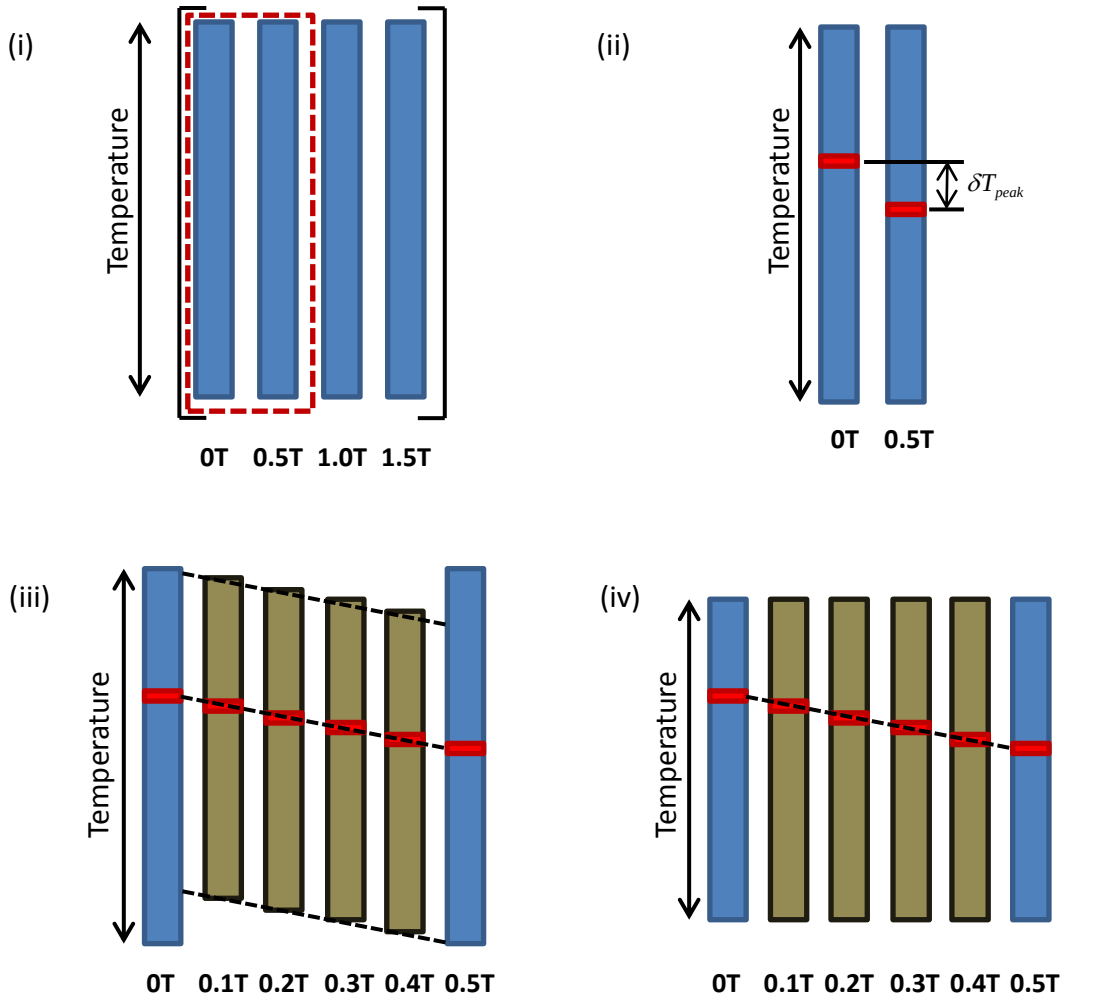

Figure 3-17 – The dark blue columns represent specific heat data at different field strengths, the tan columns represent interpolated specific heat data, and the red bars indicate the peak specific heat value for each field strength.
(i) The original specific heat data is displayed and the data involved in the sample interpolation are highlighted .
(ii) The red bars on the columns represent the location of the maximum specific heat at the given magnetic field and displays the difference, δT_{peak} , in temperature between the two maximums.
(iii) δT_{peak} is used to conduct a linear interpolation between high field and temperature offset and low field with no temperature offset. The vertical location of the columns represents the temperature values of the specific heat at different fields. It can be seen that after this interpolation the rows of the array are not isothermal.
(iv) All the columns are then interpolated with the same temperature vector to attain a specific heat matrix with isothermal rows.

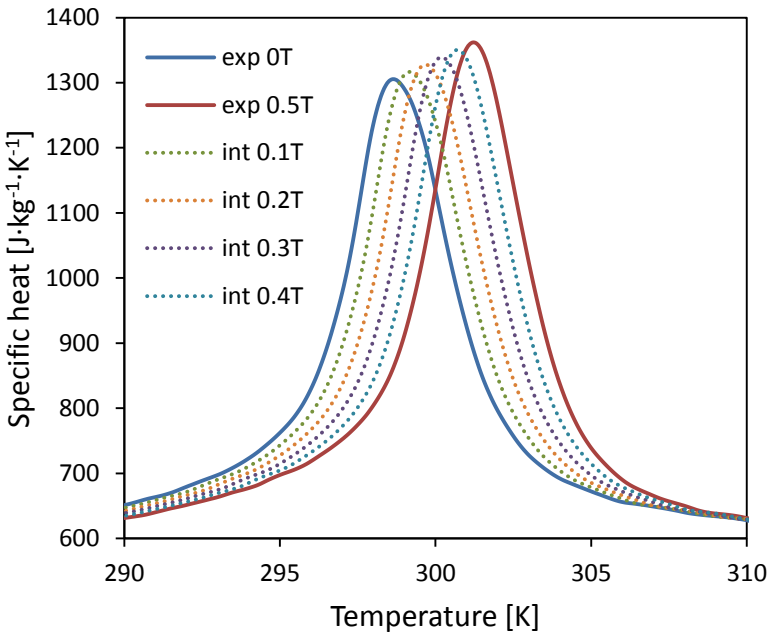

Figure 3-18 – Temperature offset interpolation results of a sample $MnFeP_{1-X}As_X$ material between zero and 0.5 Tesla.

3.3.2. Magnetization interpolation

The same method of offset interpolation is used to fill in the magnetization data gaps in applied magnetic field strengths with the exception of zero Tesla. $MnFeP_{1-x}As_x$ alloys are soft magnetic materials which have a net magnetization of zero at zero field strength. Because of this it is assumed that the magnetization is zero for all temperatures at zero field strength. Since the temperature derivative of magnetization is used in the calculations and not magnetization alone, the original magnetization curves are smoothed then differentiated with respect to temperature before being interpolated. The negative of the temperature derivative of the magnetization data has a similar shape to the specific heat data. Due to this similar shape, the magnetization derivative with respect to temperature can by interpolated by the same temperature offset interpolation outlined in Section 3.3.1.

3.3.3. Entropy interpolation

The shape of entropy curves calculated from specific heat data are simpler in the sense that they do not have a peak and are monotonically increasing. This simplified shape makes interpolation of entropy curves much less complicated than interpolating specific heat data. Entropy is calculated from specific heat using the method outlined in Section 2.1. The entropy is then linearly interpolated isothermally using the following relation

$$s^*(T) = s_{High}(T) + f \cdot \left(s_{Low}(T) - s_{High}(T)\right) \tag{3.8}$$

where $s^*(T)$ is the entropy at the interpolated magnetic field H^*, $s_{High}(T)$ is the entropy at high magnetic field, $s_{Low}(T)$ is the entropy at low magnetic field, and f is the magnetic field fraction defined by

$$f = \frac{H^* - H_{Low}}{H_{High} - H_{Low}}. \tag{3.9}$$

A sample result is displayed in Figure 3-19.

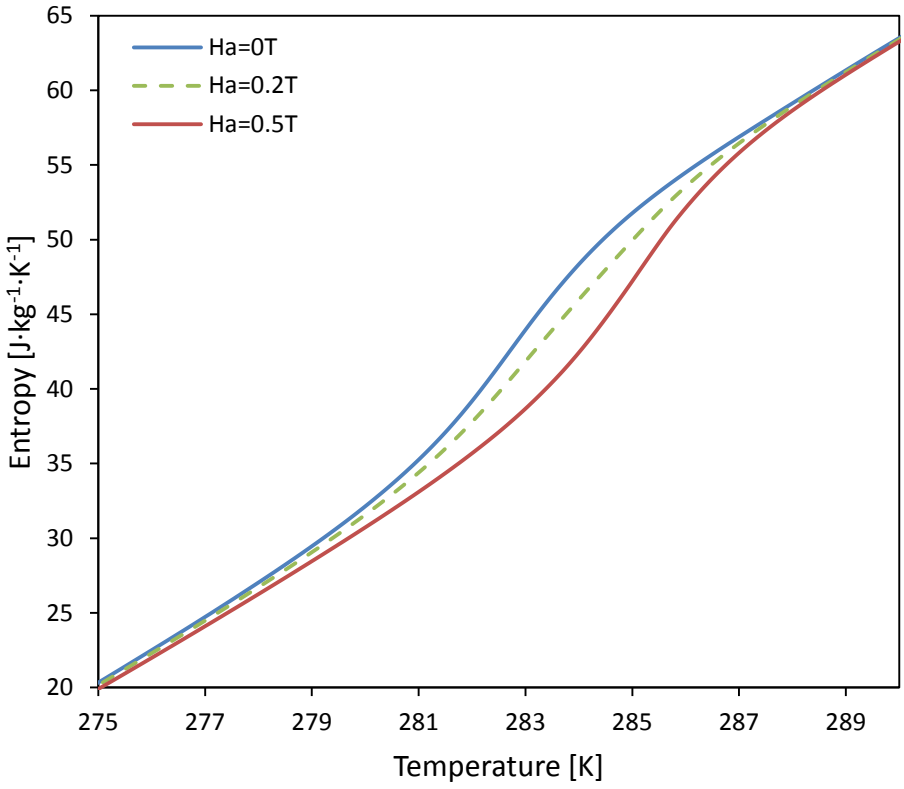

Figure 3-19 – The blue and red lines represent entropy curves calculated from specific heat data. The green dashed line represents an entropy curve calculated by isothermal linear interpolation.

3.4. Demagnetization factors

Now that all data have the same range of applied field, H_a. Demagnetization must be corrected for to present the data in the same internal field, H_{in}, range. The size, shape and composition of the tested samples determine the demagnetizing factors. Both the in-field specific heat and magnetization samples are composed of crushed particulate smaller than 150 microns. The sample holders of the two measurements are both cylinders but with different dimensions. The dimensions and corresponding demagnetizing factors can be seen in Table 3-2. The adiabatic temperature change

samples are two plates sandwiched together with the long axis parallel to the applied magnetic field, see Figure 3-9. A plate can be approximated as a thin film and a thin film running parallel to the applied field has a demagnetizing factor of zero [14].

Table 3-2 – Sample dimensions and demagnetizing factors for specific heat and magnetization data.

Measurement	Cylinder Length, *L* [mm]	Cylinder Radius, *r* [mm]	Axial demagnetizing factor $\mathcal{N}_l$	Radial demagnetizing factor $\mathcal{N}_r$	$\mathcal{N}_{rp}$ particulate correction
Specific heat	1.2	2.3	0.6255	0.1873	0.2603
Magnetization	1	1.25	0.5281	0.2359	0.2846

3.5. Correcting magnetization data for demagnetizing field

When a field-dependent property is measured the applied magnetic field may be different than the local internal field due to sample geometry. To remove the effects of shape, properties should be functions of internal field. For example the magnetization data is based on applied field, $m(T, H_a)$, while the functional dependence is on internal field, $m(T, H_{in})$. A diagram of the magnetization data is shown in Figure 3-20. For each data point the applied field and the magnetization as a function of internal field are both known. The applied field is given in Tesla while the magnetization is measured in Ampere meter squared per kilogram, $A \cdot m^2 \cdot kg^{-1}$. Combining the Equations (2.52) and (2.53), and correcting for the units of the applied field and magnetization yields the following relationship for internal field

$$H_{in} = H_a - \rho \mathcal{N}_{rp,m} m(T, H_{in}) \tag{3.10}$$

where ρ is the bulk density of the material estimated to be 6 ± 0.1 grams per cubic centimeter [9] and $\mathcal{N}_{rp,m}$ is the porosity corrected demagnetizing factor for magnetization measurement. The r subscript denotes that this demagnetization factor is for the case when applied field is in the radial direction.

$$\begin{array}{c|c} & \begin{bmatrix} H_{a1} & H_{a2} & H_{a3} & H_{a4} \end{bmatrix} \\ \hline \begin{matrix} T_1 \\ \vdots \\ \vdots \\ \vdots \\ T_j \end{matrix} & \begin{bmatrix} m\left(T_1, H_{in,11}\right) & \cdots & \cdots & m\left(T_1, H_{in,41}\right) \\ \vdots & \vdots & \vdots & \vdots \\ \vdots & \vdots & \vdots & \vdots \\ \vdots & \vdots & \vdots & \vdots \\ m\left(T_j, H_{in,1j}\right) & \cdots & \cdots & m\left(T_1, H_{in,4j}\right) \end{bmatrix} \end{array}$$

Figure 3-20 – Magnetization data diagram. Each column of data is exposed to the same field, and each row of data is exposed to the same ambient temperature. This diagram highlights that the magnetization values are dependent on internal field H_{in} rather than the applied field H_a .

Before the demagnetization correction is applied the magnetization data is smoothed, differentiated, interpolated to fill gaps in applied field data, and finally integrated back resulting in a magnetization matrix with data for applied fields from zero to two Tesla in 0.1 Tesla increments. The percent difference between the original smoothed magnetization data and the resultant magnetization data is less than 0.5%.

Applying Equation (3.10) results in a matrix of internal field values that align with the magnetization data matrix. Using the relationship between internal field and magnetization a linear interpolation of the magnetization data is conducted to attain magnetization values at internal field values equal to the original applied field values. By interpolating each row of magnetization data a new matrix is made with columns of

constant internal field and isothermal rows. Figure 3-21 shows the result of this correction. It can be seen from Figure 3-21 that the impact of demagnetization reduces with increasing applied field.

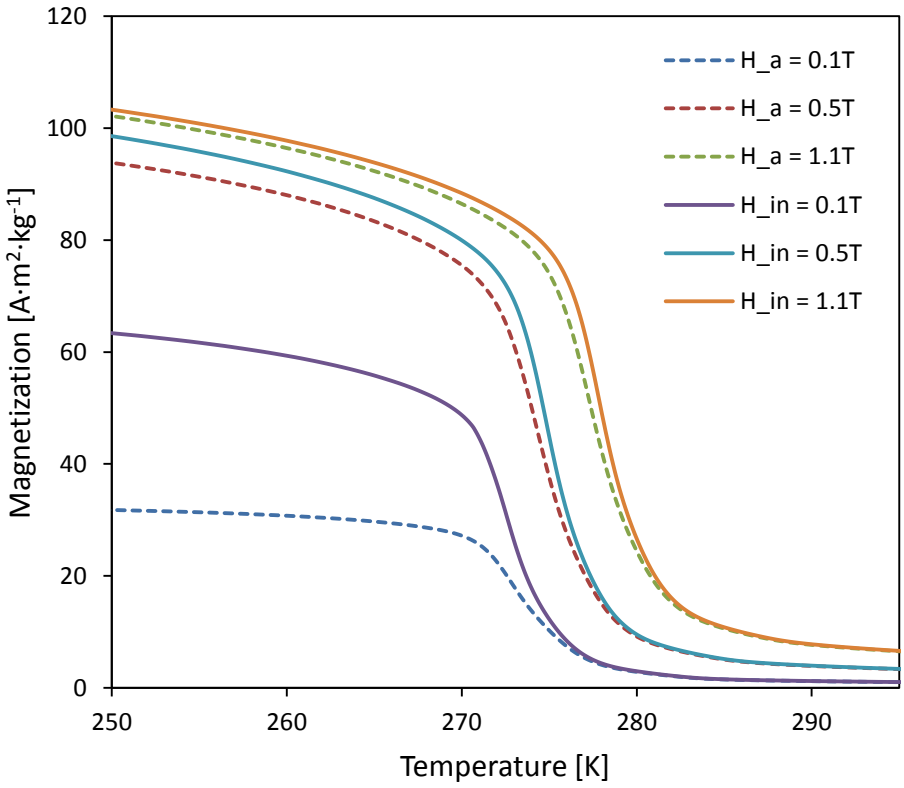

Figure 3-21 –Heating magnetization data of an example $MnFeP_{1-x}As_x$ material. The dashed lines are magnetization data at constant H_a while the solid lines are magnetization data at constant H_{in}.

3.6. Correcting specific heat data for demagnetization

The demagnetization correction is conducted on entropy curves. For an in depth description of the entropy calculation see Section 2.1 on thermodynamics. To correct the entropy data for demagnetization the method described in the previous section is slightly

adjusted. The corrected magnetized data $m(T, H_{in})$ is known for $H_{in} = [0 : 0.1 : 1.5]$ Tesla. Instead of calculating the internal field, it is assumed that the internal field ranges from 0-1.5 Tesla in 0.1 Tesla increments and the applied field that gives this internal field range is calculated. Equation (3.10) is rewritten to solve for H_a

$$H_a = H_{in} + \rho \mathcal{N}_{rp,c_B} m(T, H_{in}) \tag{3.11}$$

where $\mathcal{N}_{rp,c_B}$ is the porosity corrected demagnetizing factor for the specific heat measurement. Using the relation between the applied field strength and entropy from the entropy matrix, linear interpolation is used to find the values of entropy at the newly calculated applied field strengths that yield internal field strengths in the desired range. The result is a matrix of entropies with columns of constant internal field and isothermal rows. Figure 3-22 shows the result of this correction.

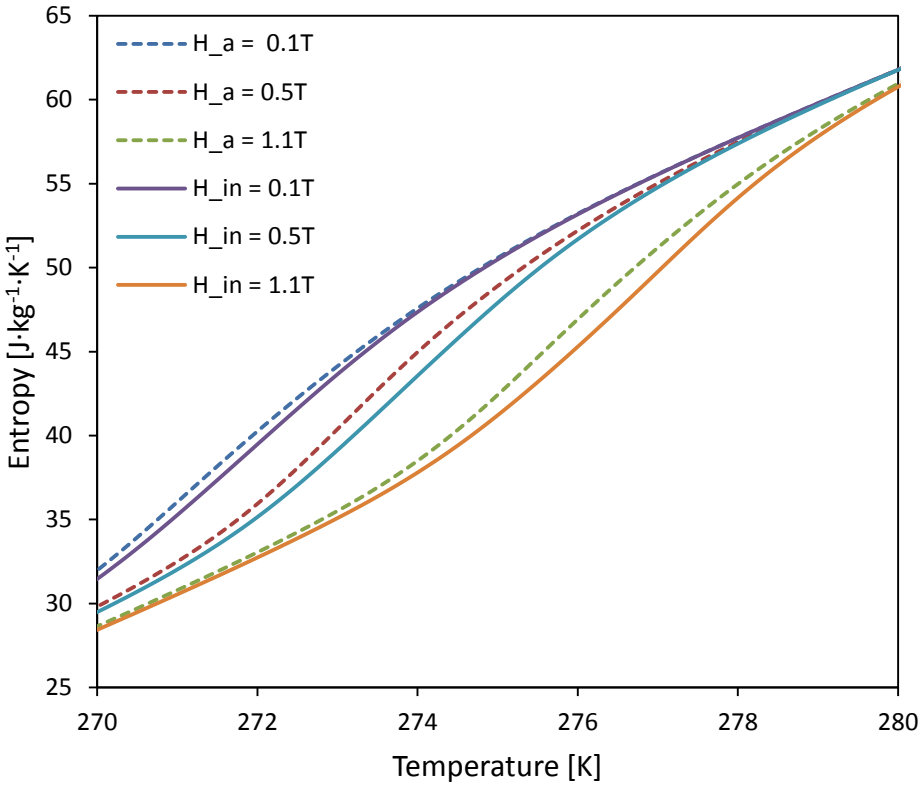

Figure 3-22 –Heating entropy data of an example $MnFeP_{1-x}As_x$ material. The dashed lines are m-data at constant H_a while the solid lines are m-data at constant H_{in}.

3.7. Hysteresis

Hysteresis may effect adiabatic temperature change. $MnFeP_{1-x}As_x$ exhibits thermal and magnetic hysteresis [13]. Thermal hysteresis is investigated due to the data collection method. Two thermal paths are followed; *heating* and *cooling*. Heating is defined by collecting data while the ambient temperature inside the test chamber is heated through a temperature range that contains the materials Curie temperature. Cooling is defined by collecting data while the ambient temperature is cooled through the same temperature range. The Curie temperature of the material is hotter in *heating* data and colder in *cooling* data. Specific heat and magnetization data for select applied field

strengths are plotted in Figure 3-23 and Figure 3-24 for sample 2. All materials exhibit the same trend for heating and cooling data. In order to quantify thermal hysteresis, it must be defined. For this study, the thermal hysteresis is defined as the difference in temperature of the peak specific heat at zero field between heating and cooling.

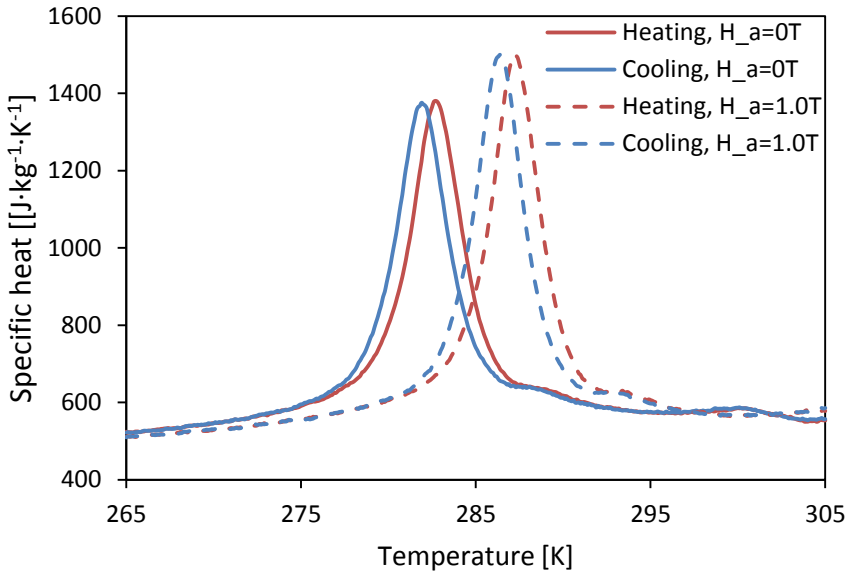

Figure 3-23 – Heating and cooling specific heat data at two applied field strengths of sample 2.

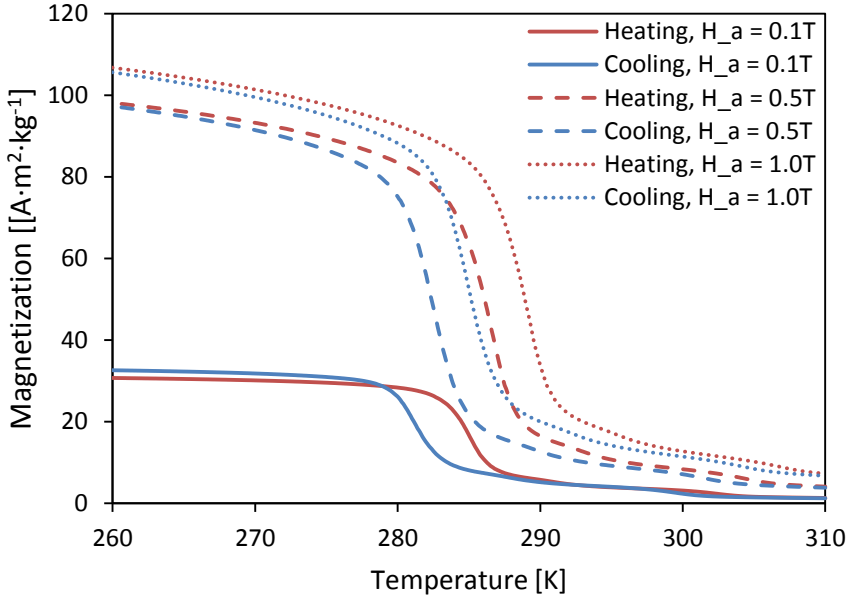

Figure 3-24 – Heating and cooling magnetization data at three applied fields of a sample 2.

Adiabatic temperature change caused by a change in magnetic field is determined by the temperature difference between the high and low magnetic field entropy curves. There are four possible entropy curve combinations to calculate adiabatic temperature change because there are *heating* and *cooling* curves of both high and low magnetic field entropy curves. Figure 3-25 gives a visual representation of the four protocols. The four ΔT_{ad} protocol definitions are presented in Table 3-3.

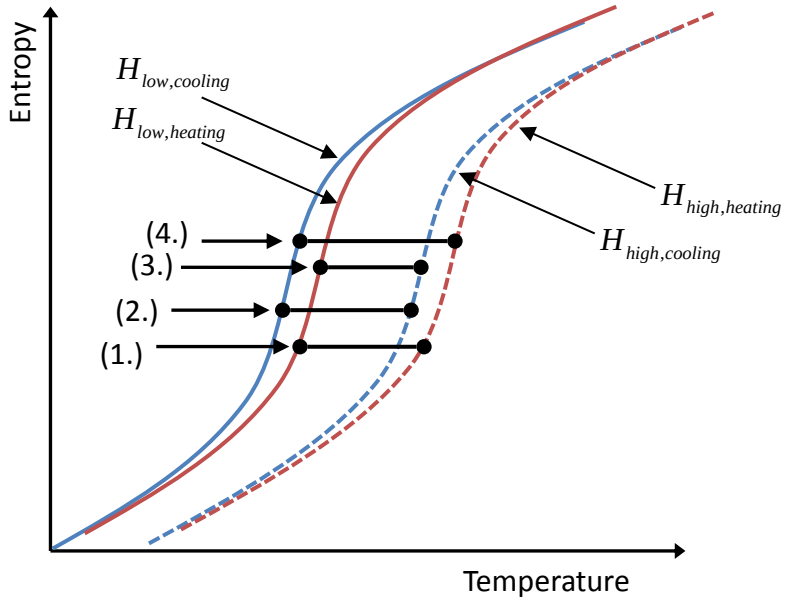

Figure 3-25 – Schematic of the four ΔT_{ad} calculation protocols.

Table 3-3 – Protocols are defined by the low and high field entropy curve used to determine the isentropic temperature change.

Protocol	Low field entropy curve	High field entropy curve	ΔT_{ad} label
1	Heating	Heating	$\Delta T_{ad,hh}$
2	Cooling	Cooling	$\Delta T_{ad,cc}$
3	Heating	Cooling	$\Delta T_{ad,hc}$
4	Cooling	Heating	$\Delta T_{ad,ch}$

3.8. Uncertainties

The propagation of uncertainty in the calculation of ΔT_{ad} from specific heat and magnetization is described here. Specific heat data collected by BASF have a relative uncertainty of 4 percent. Magnetization data have a relative uncertainty of 0.5 percent.

Entropy calculated from specific heat using the Equation (2.3) has an absolute associated uncertainty when integrated using the trapezoidal numerical approximation of [29]

$$\sigma\left[s\left(T_n\right)_H\right] \cong 0.5\left\{\sigma c_H\left(T_1\right)+\sum_{i=1}^{n-1}\left[\left(\frac{\sigma c_H\left(T_i\right)}{T_i}+\frac{\sigma c_H\left(T_{i+1}\right)}{T_{i+1}}\right)\left(T_{i+1}-T_i\right)\right]\right\} \qquad (3.12)$$

where $\sigma c_H\left(T_i\right)$ is the absolute error in the specific heat measurement at temperature T_i. However in this study the entropy is not calculated from $T=0$ therefore the entropy is calculated using Equation (2.5) which has a corresponding absolute uncertainty of

$$\sigma\left[s\left(T_n\right)_H\right] \cong 0.5\sum_{i=1}^{n-1}\left[\left(\frac{\sigma c_H\left(T_i\right)}{T_i}+\frac{\sigma c_H\left(T_{i+1}\right)}{T_{i+1}}\right)\left(T_{i+1}-T_i\right)\right] \qquad (3.13)$$

when integrated using the trapezoidal approximation.

The high field entropy data is then shifted by the magnetic entropy change offset calculated with the magnetization data using Equation (2.7). The absolute uncertainty related to Δs_m, assuming trapezoidal integration again, is given by

$$\sigma\left[\Delta s_m\left(T_i, H_n\right)\right] \cong 0.5\sum_{j=1}^{n-1}\left[\left(\sigma\left(\frac{\partial m\left(T_i\right)}{\partial T_i}\right)_{H_j}+\sigma\left(\frac{\partial m\left(T_i\right)}{\partial T_i}\right)_{H_{j+1}}\right)\left(\mu_0 H_{j+1}-\mu_0 H_j\right)\right] \qquad (3.14)$$

where $\sigma\left(\frac{\partial m\left(T_i\right)}{\partial T_i}\right)_H$ is the absolute uncertainty in the temperature derivative of magnetization and is given by

$$\sigma\left(\frac{\partial m(T_i)}{\partial T_i}\right)_H = \frac{\sigma m(T_{i-1}) + \sigma m(T_{i+1})}{2 \cdot \delta T} \tag{3.15}$$

where $\delta T = 0.1$ is the temperature interval between measurements. Once all entropy uncertainties are determined, the uncertainty in the calculated adiabatic temperature change can be determined.

Adiabatic temperature change uncertainty is dependent on three uncertainties; low field entropy, high field entropy, and magnetic entropy change. The absolute uncertainty of the calculated adiabatic temperature change can be calculated using [29]

$$\sigma\left[\Delta T_{ad}\left(T, H_{Low} \rightarrow H_{High}\right)\right] = \begin{bmatrix} \sigma s\left(T, H_{Low}\right)\dfrac{T}{c_H\left(T, H_{Low}\right)} \\ +\sigma s\left(T, H_{High}\right)\dfrac{T}{c_H\left(T, H_{High}\right)} \\ +\sigma \Delta s_m\left(T_1, H_{High}\right) \end{bmatrix}_S . \tag{3.16}$$

This uncertainty method adds every error resulting in an ‘unusably’ large uncertainty but gives the maximum error one would see using this method in the worst case scenario. It is not probable that the error terms will be either all positive or all negative. It is more probable that some will cancel each other out. Applying the root sum of squares (RSS) to uncertainty calculations is presented by [30] as a method that gives a more reasonable error estimate.

Consider a function G to be a function of n measured variables [30]

$$G = f\left(x_1, x_2, \ldots x_n\right) \tag{3.17}$$

where each measured variable x has an associated uncertainty σx_i . The uncertainty in G can then be determined as follows

$$\sigma G = \sigma x_1 \frac{\partial G}{\partial x_1} + \sigma x_2 \frac{\partial G}{\partial x_2} + \ldots + \sigma x_n \frac{\partial G}{\partial x_n} = \sum_{i=1}^{n} \sigma x_i \frac{\partial G}{\partial x_i}. \tag{3.18}$$

The maximum uncertainty in G can be found by forcing all terms to be positive:

$$\sigma G_{\max} = \sum_{i=1}^{n} \left| \sigma x_i \frac{\partial G}{\partial x_i} \right|. \tag{3.19}$$

As mentioned earlier this is not a probable uncertainty, a more reasonable estimate for the uncertainty in G is found by calculating the root of the sum of the squares (RSS)

$$\sigma G = \left[\sum_{i=1}^{n} \left(\sigma x_i \frac{\partial G}{\partial x_i} \right)^2 \right]^{1/2}. \tag{3.20}$$

RSS is applied to all uncertainty calculations that involve the addition of errors. Equation (3.13) becomes

$$\sigma\left[s\left(T_n\right)_H \right] \cong \left\{ \sum_{i=1}^{n-1} \left[0.5 \left(\frac{\sigma c_H\left(T_i\right)}{T_i} + \frac{\sigma c_H\left(T_{i+1}\right)}{T_{i+1}} \right) \left(T_{i+1} - T_i\right) \right]^2 \right\}^{1/2}. \tag{3.21}$$

Equation (3.14) becomes

$$\sigma\left[\Delta s_m\left(T_i, H_n\right) \right] \cong \left\{ \sum_{j=1}^{n-1} \left[0.5 \left(\sigma \left(\frac{\partial m\left(T_i\right)}{\partial T_i} \right)_{H_j} + \sigma \left(\frac{\partial m\left(T_i\right)}{\partial T_i} \right)_{H_{j+1}} \right) \left(H_{j+1} - H_j\right) \right]^2 \right\}^{1/2}. \tag{3.22}$$

Equation (3.15) becomes

$$\sigma \left(\frac{\partial m\left(T_i\right)}{\partial T_i} \right)_H = \left[\left(0.5 \frac{\sigma m\left(T_{i-1}\right)}{\delta T} \right)^2 + \left(0.5 \frac{\sigma m\left(T_{i+1}\right)}{\delta T} \right)^2 \right]^{1/2}. \tag{3.23}$$

Equation (3.16) becomes

$$\sigma\left[\Delta T_{ad}\left(T, H_{Low} \rightarrow H_{High}\right)\right] = \left[\begin{array}{l} \left(\sigma s\left(T, H_{Low}\right)\dfrac{T}{c_H\left(T, H_{Low}\right)}\right)^2 \\ +\left(\sigma s\left(T, H_{High}\right)\dfrac{T}{c_H\left(T, H_{High}\right)}\right)^2 \\ +\sigma\Delta s_m\left(T_1, H_{High}\right)^2 \end{array}\right]_S^{1/2} . \qquad (3.24)$$

The error in adiabatic temperature change for a sample material before and after RSS is applied is displayed in Figure 3-26.

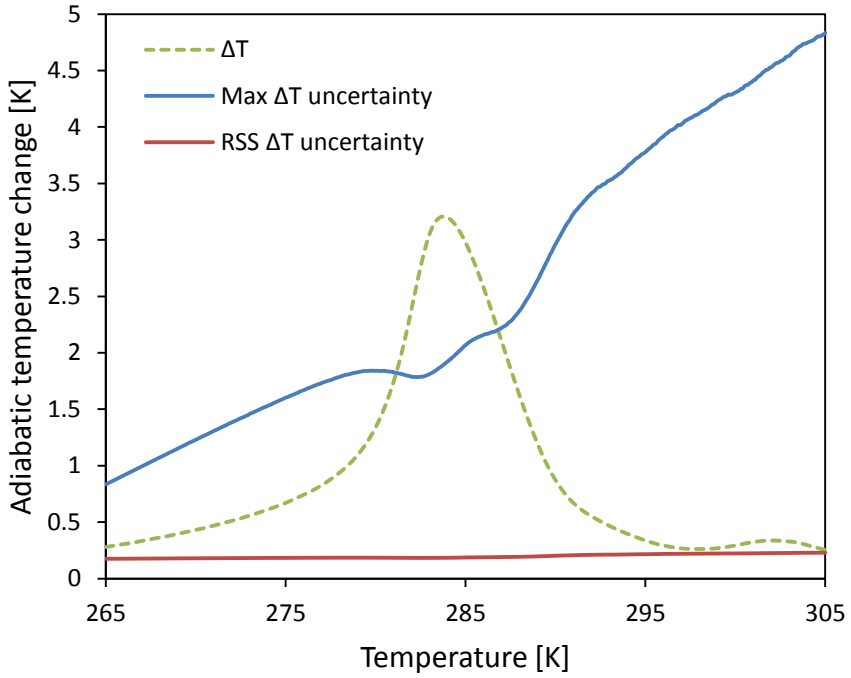

Figure 3-26 – The maximum and RSS absolute uncertainties in calculated adiabatic temperature change are plotted with the calculated adiabatic temperature change.

The RSS uncertainty is used for this analysis since the max uncertainty produces uncertainties larger than the calculated and measured values in at some temperatures.

3.9. Summary

The processes outlined in this chapter along with the calculations from Chapter 2 are combined to calculate ΔT_{ad} from specific heat and magnetization data of $MnFeP_{1-x}As_x$ alloys obtained from [9]. The calculated ΔT_{ad} results are presented in Chapter 4. MFT results are also presented to give confidence to the calculation methods used in the ΔT_{ad} calculation.

Chapter 4 – Results

The ΔT_{ad} results of $MnFeP_{1-x}As_x$ alloys from the equations and processes described in Chapter 2 and Chapter 3 are presented in this chapter. Material properties of Gadolinium calculated from MFT, described in Chapter 2, and measured by AMES are also presented.

MFT calculated Gadolinium data are presented first. Measured specific heat and ΔT_{ad} Gadolinium data are presented to show the effectiveness of MFT in calculating properties. MFT Gadolinium data are used to validate three calculations; the integration of specific heat to attain entropy, the isothermal field induced change in entropy from magnetization, and the ΔT_{ad} calculation from high and low field entropy curves.

Calculated ΔT_{ad} of $MnFeP_{1-x}As_x$ alloys are presented and compared against measured values. Peak location, peak magnitude, full width at half maximum (FWHM), and total error are metrics used to compare calculated and measured values.

4.1. MFT Gadolinium results

Material properties of Gadolinium are calculated using MFT which include magnetization, specific heat, entropy, and ΔT_{ad}. Specific heat and ΔT_{ad} are compared against AMES laboratory data that has been corrected for demagnetization by researchers from the Department of Energy Conversion and Storage at the Technical University of Denmark. The material properties of Gadolinium required for MFT are listed in the nomenclature section at the beginning of the document.

4.1.1. Magnetization

Magnetization is the first property calculated in MFT. With magnetization, specific heat and entropy can be calculated. Figure 4-1 plots the magnetization calculated using mean field theory for three field strengths.

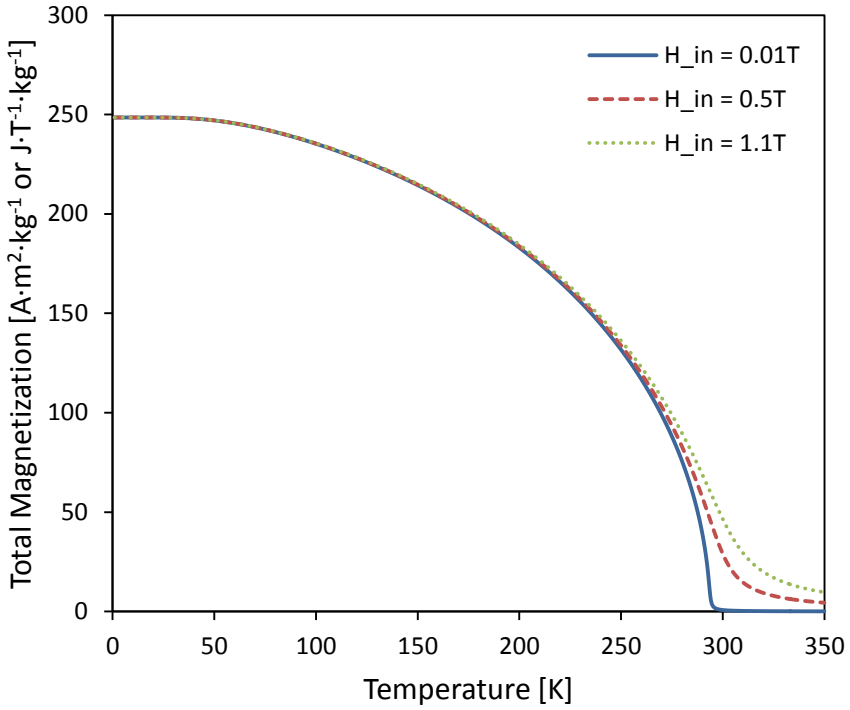

Figure 4-1 – Magnetization of Gadolinium at three field strengths.

4.1.2. Specific heat

The magnetic contribution to specific heat data is calculated from magnetization data. Lattice and electronic contributions to specific heat are independent of magnetic field. The three components and total of specific heat for Gadolinium are displayed in Figure 4-2. Note that only the magnetic contribution of specific heat changes with magnetic field strength.

MFT calculated specific heat data are compared to measured data provided by AMES Lab. Because MFT calculates material properties based on internal field, the measured data from AMES is corrected for demagnetization. The measured specific heat data are plotted against calculated MFT data in Figure 4-4 and Figure 4-3.

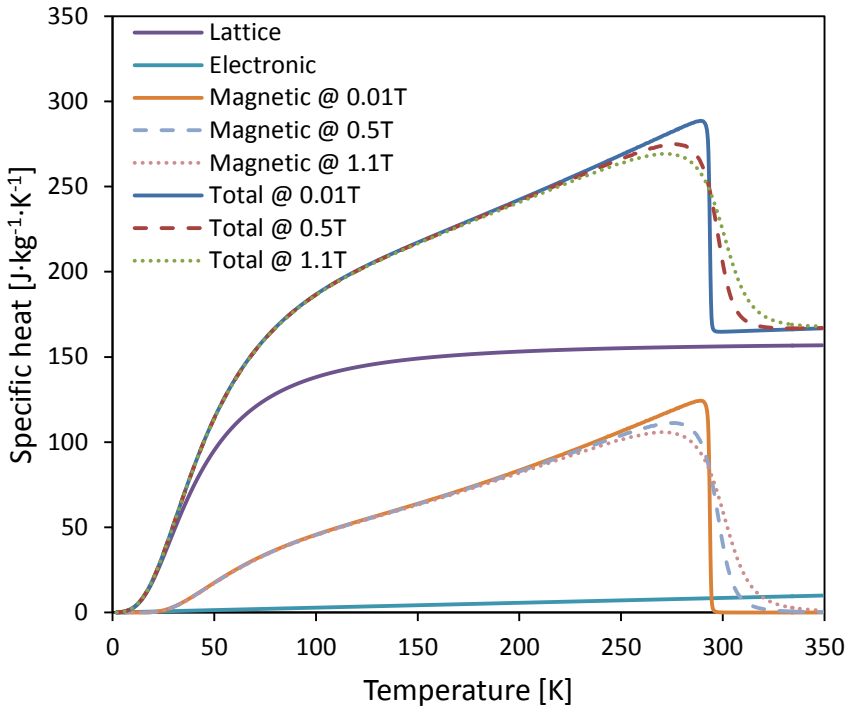

Figure 4-2 – Specific heat has three components that are plotted above: lattice, electronic and magnetic. Total specific heat data produced by MFT of Gadolinium for three internal field strengths are also plotted.

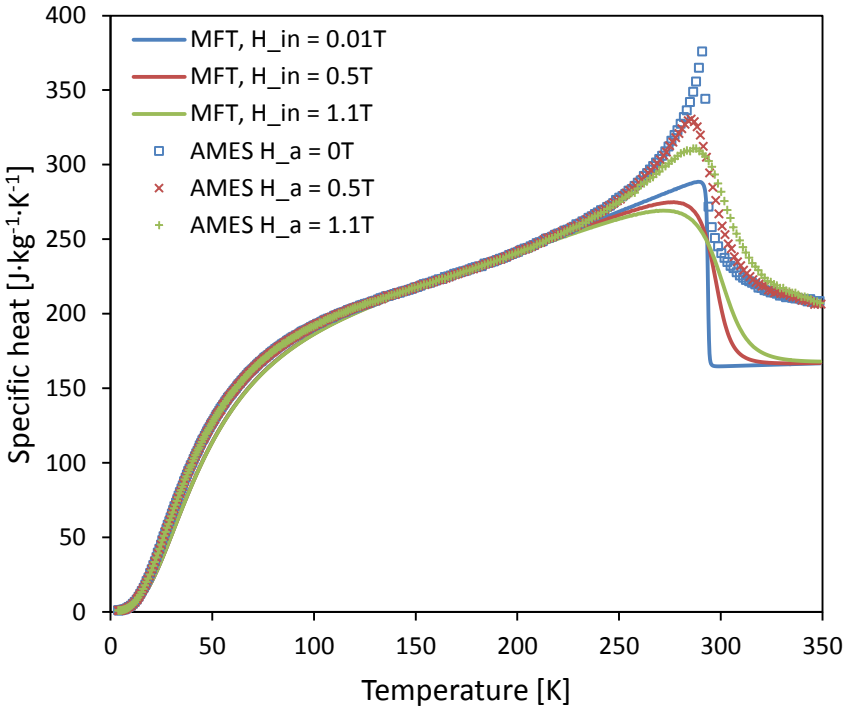

Figure 4-3 – Gadolinium MFT results compared to the original AMES specific heat data [8].

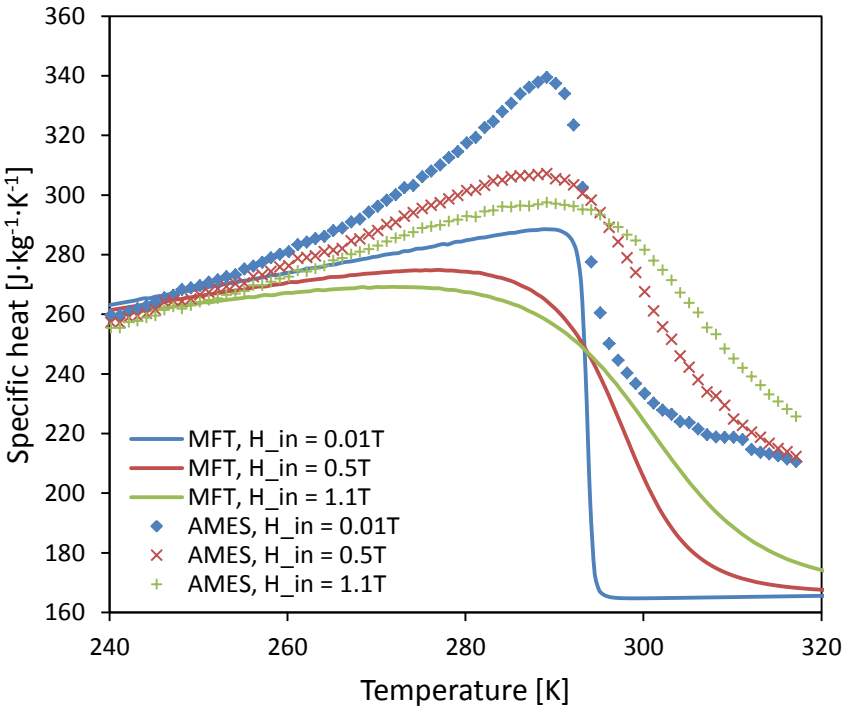

Figure 4-4 – Gadolinium MFT results compared to the corrected AMES specific heat data [10].

4.1.3. Entropy

Entropy is calculated using two different methods in MFT to increase confidence in the calculations. One method integrates the specific heat data displayed in Section 4.1.2 using Equation (2.3). The other method calculates entropy using Equation (2.50). Both methods yield the same result to within less than 0.1 $J \cdot kg^{-1} \cdot K^{-1}$ for each data point as can be seen in Figure 4-5. This gives confidence to the implementation of Equation (2.3). The resultant entropy curves are plotted in Figure 4-6. A more detailed look about the Curie temperature of the entropy data is displayed in Figure 4-7.

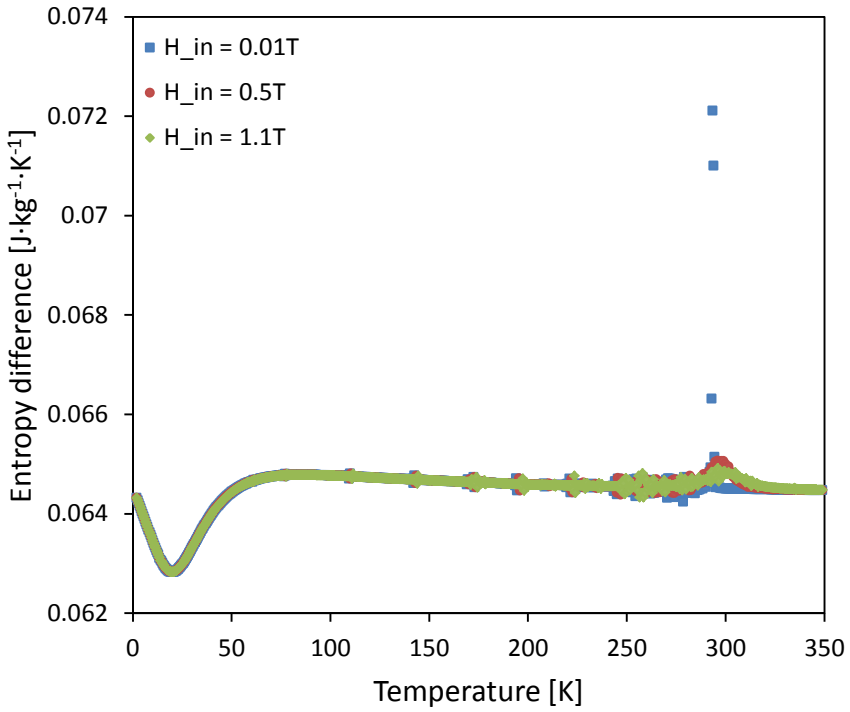

Figure 4-5 – The difference in entropy calculated from method 1 and 2 are plotted. The difference is calculated by subtracting method 1 results from method 2 results.

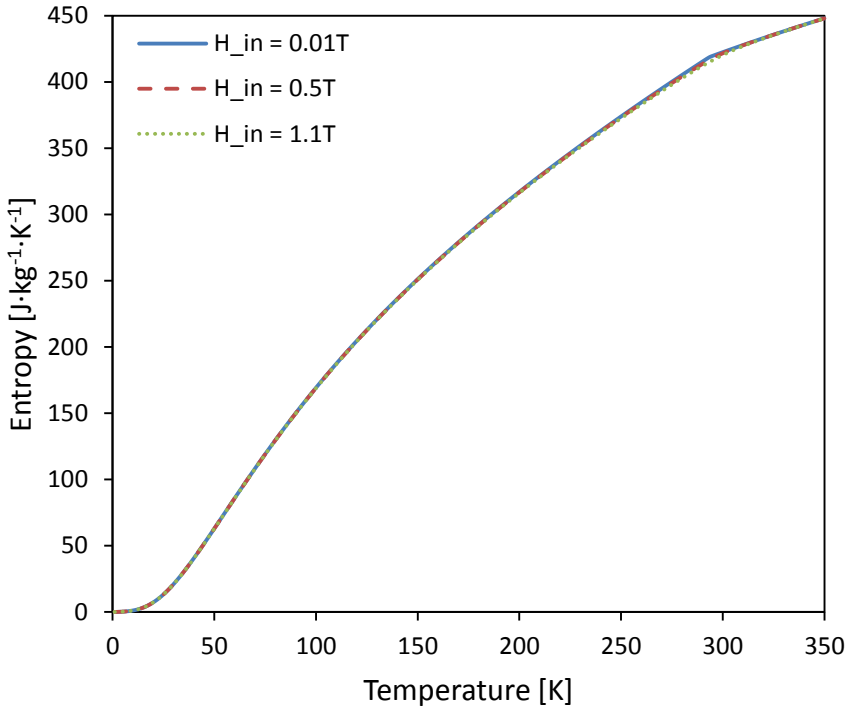

Figure 4-6 – Calculated entropy data at three internal field strengths.

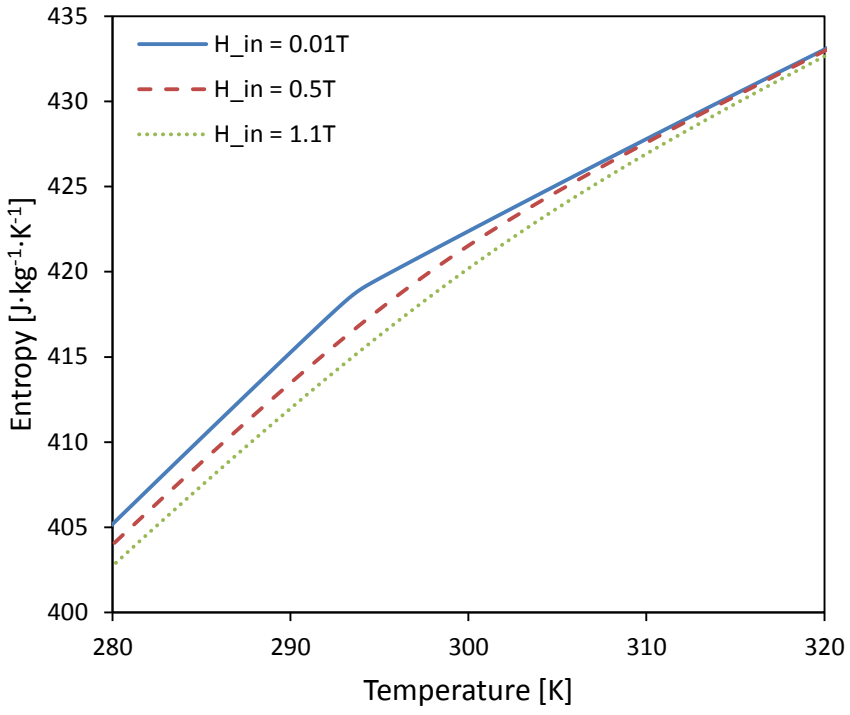

Figure 4-7 – A closer look at the entropy curves near the Curie temperature.

4.1.4. Adiabatic temperature change

Adiabatic temperature change is calculated using equation (2.9) and the entropy data displayed in Section 4.1.3. The raw and corrected measured ΔT_{ad} data is presented in Figure 4-8. Calculated ΔT_{ad} is plotted against the raw measured data in Figure 4-9 and the corrected data in Figure 4-10. MFT data agrees better with corrected data. The visual agreement between calculated and measured ΔT_{ad} in Figure 4-10 gives confidence in the implementation of MFT and of Equation (2.9).

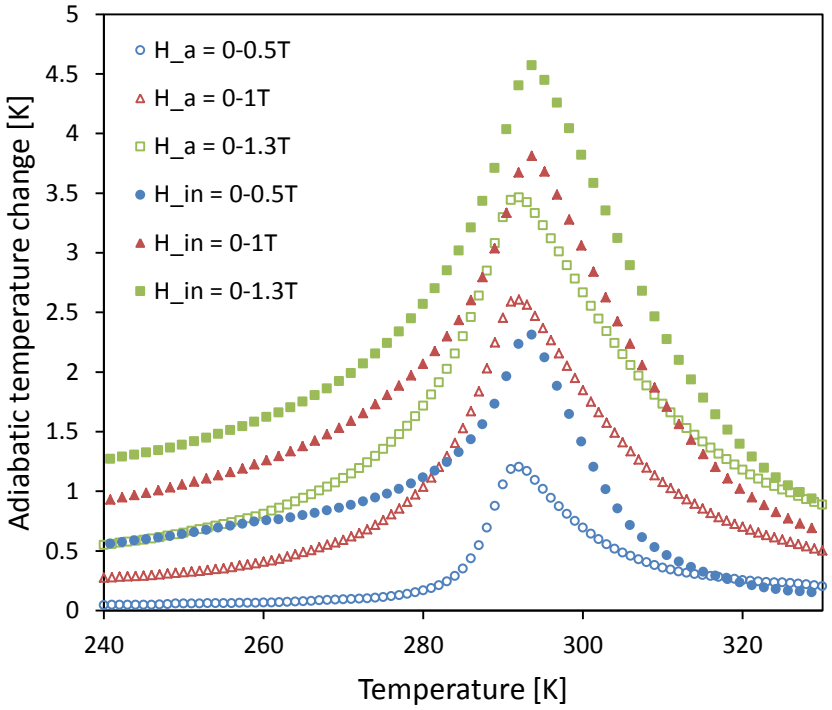

Figure 4-8 – The data series with hollow markers are the original adiabatic temperature change data that has not been corrected for demagnetization. The original data series are labeled with H_a which stands for applied field. The data series with solid markers are the corrected data. The corrected data series are labeled with H_in which stands for internal field.

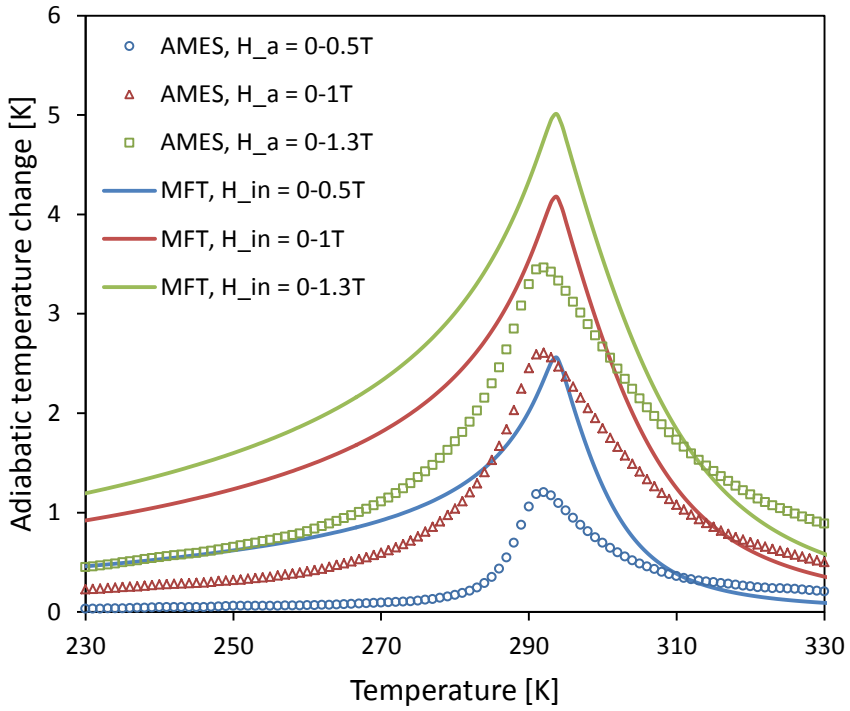

Figure 4-9 - MFT adiabatic temperature change compared to original adiabatic temperature change data from AMES laboratory.

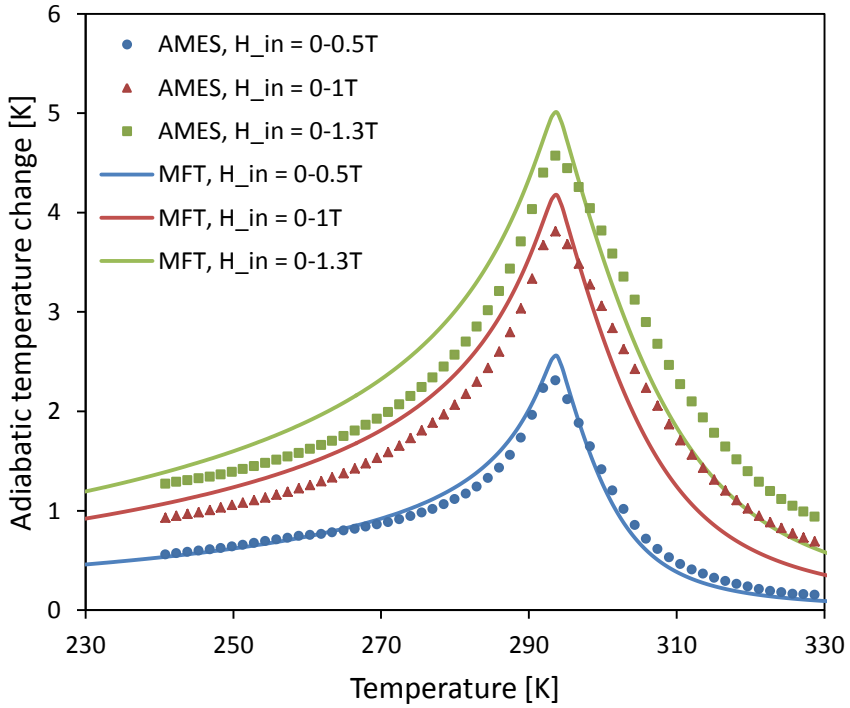

Figure 4-10 – MFT adiabatic temperature change compared to demagnetization corrected adiabatic temperature change data from AMES laboratory.

4.1.5. Isothermal field induced change in entropy

The calculation of entropy of $MnFeP_{1-x}As_x$ alloys involves an isothermal field induced change in entropy that can be determined with magnetization data as presented in Equation (2.8). To improve the confidence in this calculation, MFT entropy data is calculated two ways that should yield the same result. Entropy is calculated from zero to 350 Kelvin using Equation (2.3) with specific heat data with the same temperature range. Entropy is also calculated from $T_1 = 250K$ to $T_2 = 350K$ using equation (2.8) with specific heat data with the same temperature range $(250K - 350K)$ and magnetization data with a temperature range the spans T_1. The results from both methods are compared over the 250- 350 Kelvin temperature change. Figure 4-11 shows the percent difference between the two calculation methods.

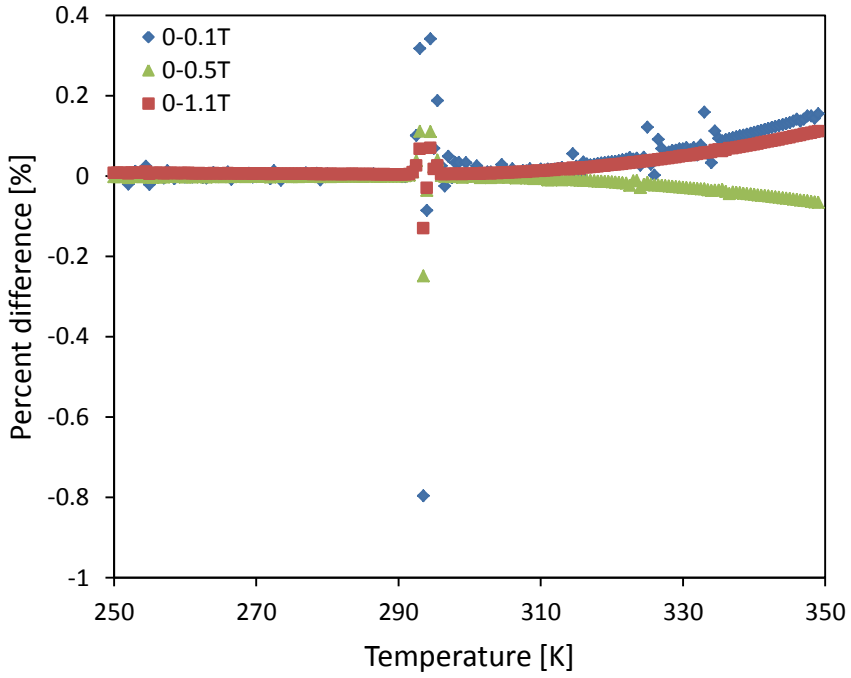

Figure 4-11 – The percent difference between adiabatic temperature change data calculated using two different methods is plotted here for three magnetic field changes.

MFT Gadolinium data gives confidence to three calculation methods that are used in the ΔT_{ad} calculations of $MnFeP_{1-x}As_x$ alloys. These calculations include calculating entropy from specific heat using Equation (2.8), calculating the isothermal field induced entropy change using Equation (2.7), and calculating ΔT_{ad} from high and low field entropy curves using Equation (2.9). The following sections are concerned with the results of the $MnFeP_{1-x}As_x$ alloy analysis that includes the equations discussed above. The effects of including the isothermal field induced entropy change in the entropy calculation of $MnFeP_{1-x}As_x$ alloys are presented in the next section.

4.2. Isothermal field induced change in entropy of $MnFeP_{1-x}As_x$

The impact of isothermal field induced entropy change $\left(\Delta s_H\right)$ on the ΔT_{ad} calculation of $MnFeP_{1-x}As_x$ alloys is presented. Figure 2-3 provides a representation of Δs_H and how it is implemented into the entropy calculation. The magnitude of Δs_H is presented for all alloys. The isothermal field induced change in entropy can be calculated using magnetization data, see Section 2.1. The change in magnetic entropy, Δs_H, can be calculated at the lowest temperature specific heat data point because the magnetization temperature range extends colder and hotter than the specific heat temperature range for all material data sets. This change in entropy is applied as an offset to the entire high field entropy curve and results in a slightly larger adiabatic temperature change peak. The entropy offset for heating and cooling data of all nine materials is displayed in Figure 4-12. Figure 4-13 shows the increase in adiabatic temperature change for a $MnFeP_{1-x}As_x$ sample alloy. The magnetic entropy change for this sample alloy for zero field to three

applied field strengths are plotted in Figure 4-14. As described in Section 2.1 the 'offset' label in Figure 4-14 is Δs_H that is subtracted from the entire high field entropy data set.

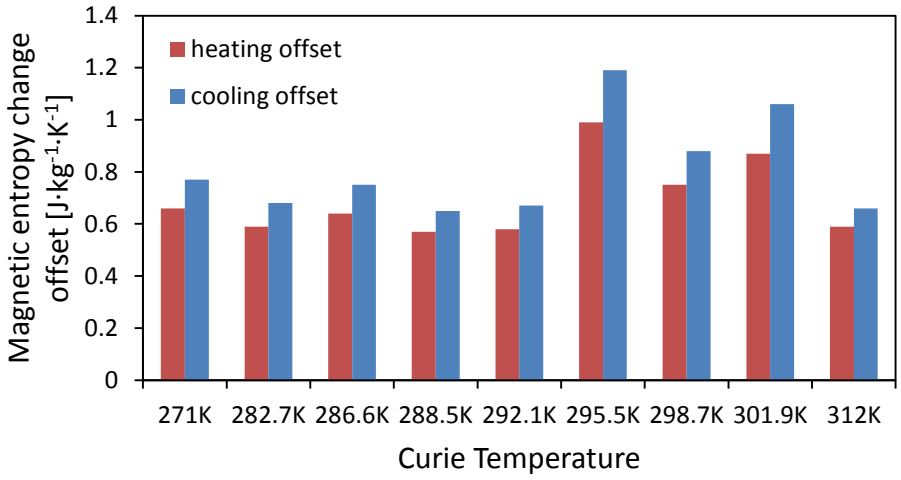

Figure 4-12 – The magnetic entropy change offset of each material for a field change from 0-1.1T.

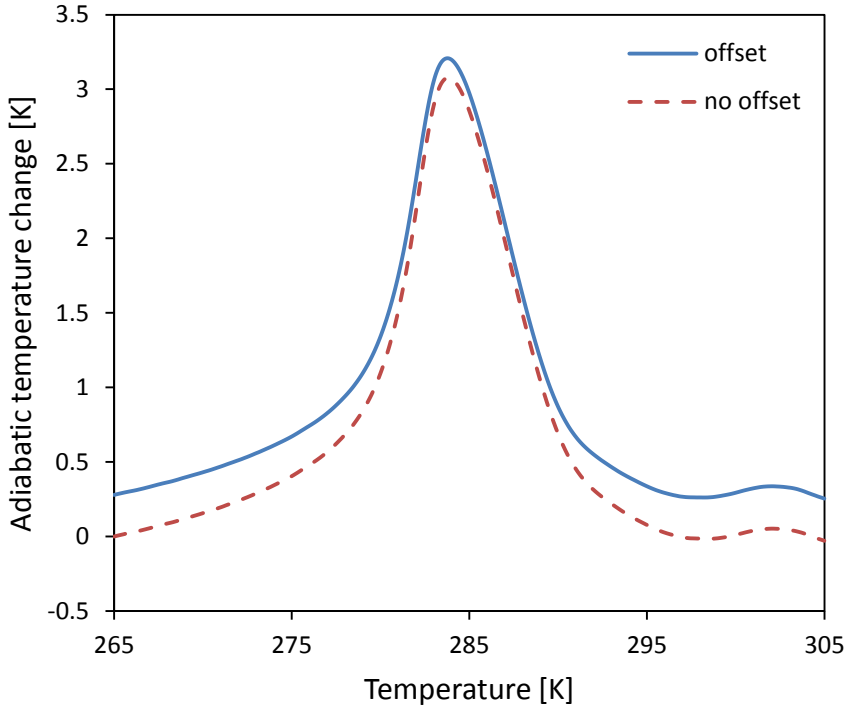

Figure 4-13 – The increase in adiabatic temperature change due to the addition of the magnetic entropy change is illustrated here.

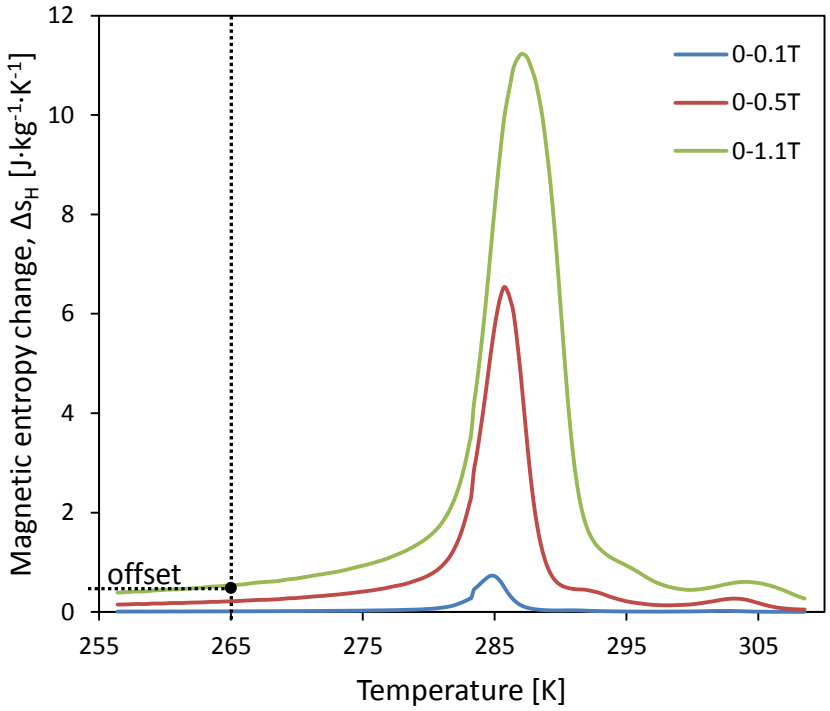

Figure 4-14 – The ‘offset’ is the magnetic entropy change value that is subtracted from the entire high field entropy curve.

4.3. Demagnetization results

The final correction applied to $MnFeP_{1-x}As_x$ data is for demagnetization. The correction is applied using the theory outlined in Section 2.8 and the processes outlined in Section 3.4, Section 3.5, and Section 3.6. By correcting for demagnetization the difference between high and low field effectively increases leading to an increase in adiabatic temperature change. The effect of the demagnetization correction on calculated ΔT_{ad} results for sample 2 can be seen in Figure 4-15.

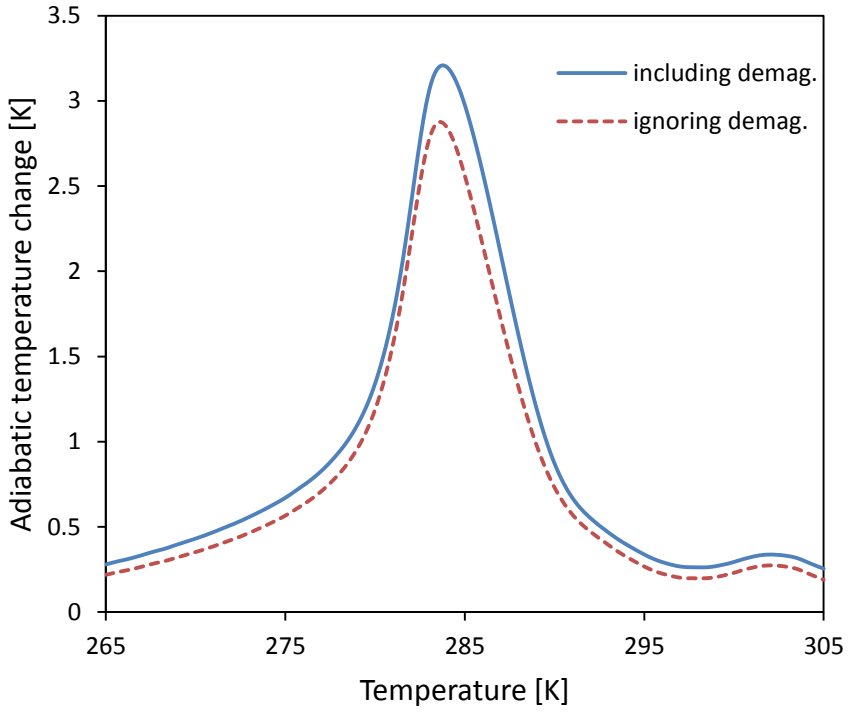

Figure 4-15 – Adiabatic temperature change results from including and ignoring demagnetization are compared for sample 2.

4.4. Measured versus calculated ΔT_{ad}

The results of calculated ΔT_{ad} of $MnFeP_{1-x}As_x$ alloys are presented in this section. Measured and calculated ΔT_{ad} data are compared using peak magnitude $\left(\Delta T_{peak}\right)$, peak temperature $\left(T_{peak}\right)$, full width at half maximum $\left(FWHM\right)$, and total error as metrics, see Figure 4-16. The total error between measured and calculated values is determined by

$$Error = \frac{\int_{T_1}^{T_2}\left(\Delta T_{ad,calc} - \Delta T_{ad,meas}\right)^2 dT}{T_2 - T_1}. \tag{4.1}$$

Each material has two measured ΔT_{ad} curves, $\Delta T_{ad,meas}$ and four calculated ΔT_{ad} curves, $\Delta T_{ad,calc}$ due to hysteresis. Hysteresis is explained in Section 3.7. Measured heating ΔT_{ad} is compared against calculated heating-heating, heating-cooling, and cooling-heating ΔT_{ad}. Measured heating ΔT_{ad} is not compared to cooling-cooling ΔT_{ad} to reduce the number of curves compared. Measured cooling ΔT_{ad} is compared against calculated cooling-cooling, heating-cooling, and cooling-heating ΔT_{ad}. Measured cooling ΔT_{ad} is not compared against calculated heating-heating ΔT_{ad} to reduce the number of curves compared.

All metrics, except total error, are presented in terms of percent difference of the calculated curve and the measured curve using the following percent difference

$$Percent_{diff} = \frac{calc - meas}{meas} \cdot 100\% \tag{4.2}$$

where $calc$ is any calculated curve metric and $meas$ is the corresponding measured curve metric. Figure 4-17 to Figure 4-22 show measured and calculated ΔT_{ad} curves for

three sample alloys. Figure 4-31 to Figure 4-36 show the same measured and calculated curves with uncertainty bands curves due to measurement error and error progression through calculations. Table 4-1 presents the metric values of the measured and calculated ΔT_{ad} for all nine alloys. Figure 4-23 to Figure 4-28 plot the percent difference of metric values between measured and calculated values.

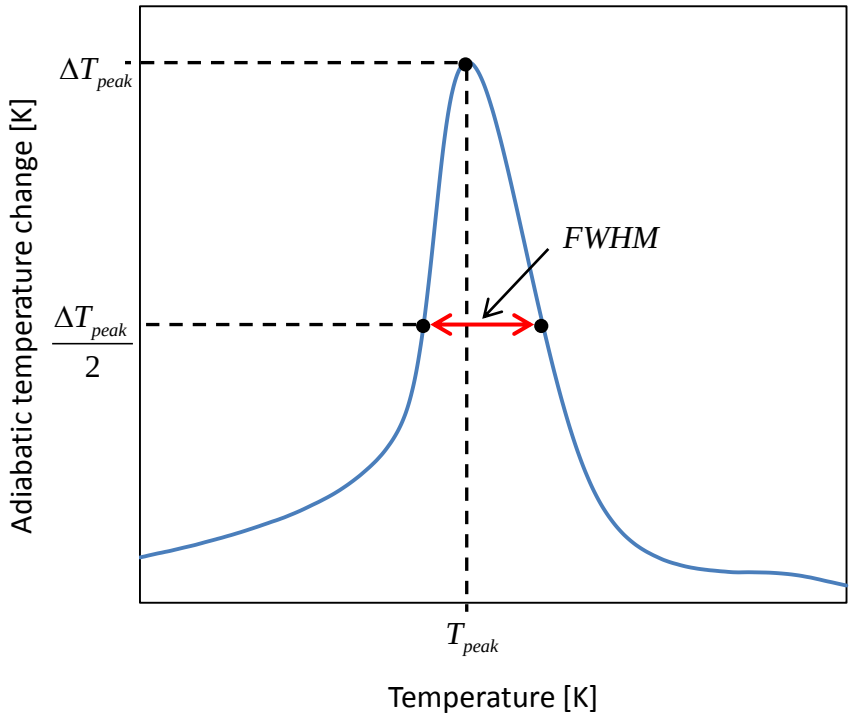

Figure 4-16 - The metrics use to compare the measured against the calculated ΔT_{ad} including peak magnitude $\left(\Delta T_{peak}\right)$, peak temperature $\left(T_{peak}\right)$, and full width at half maximum $\left(FWHM\right)$ are presented here.

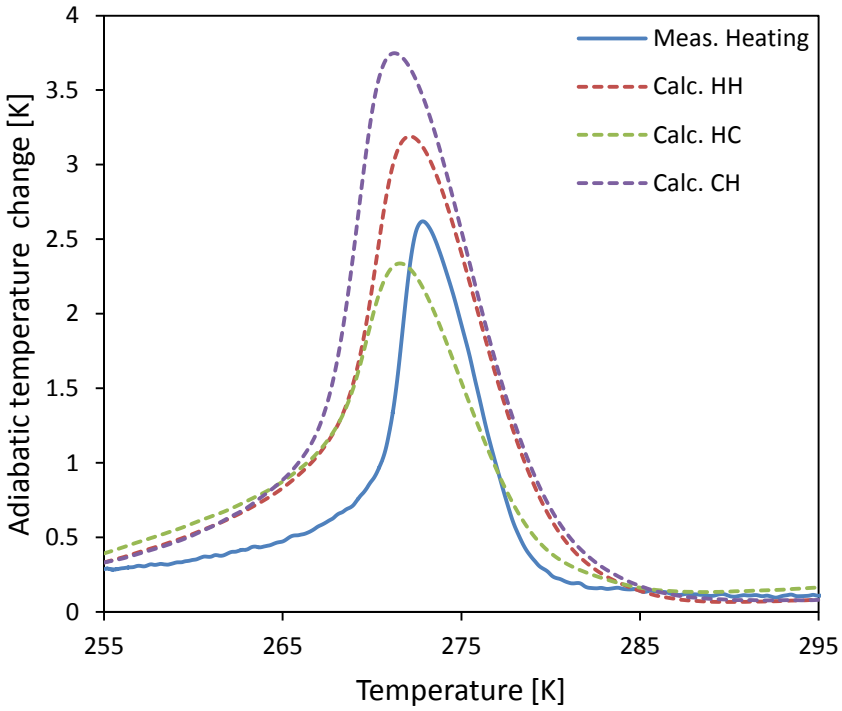

Figure 4-17 – Material 1 measured heating adiabatic temperature change data compared against three calculated adiabatic temperature change data sets.

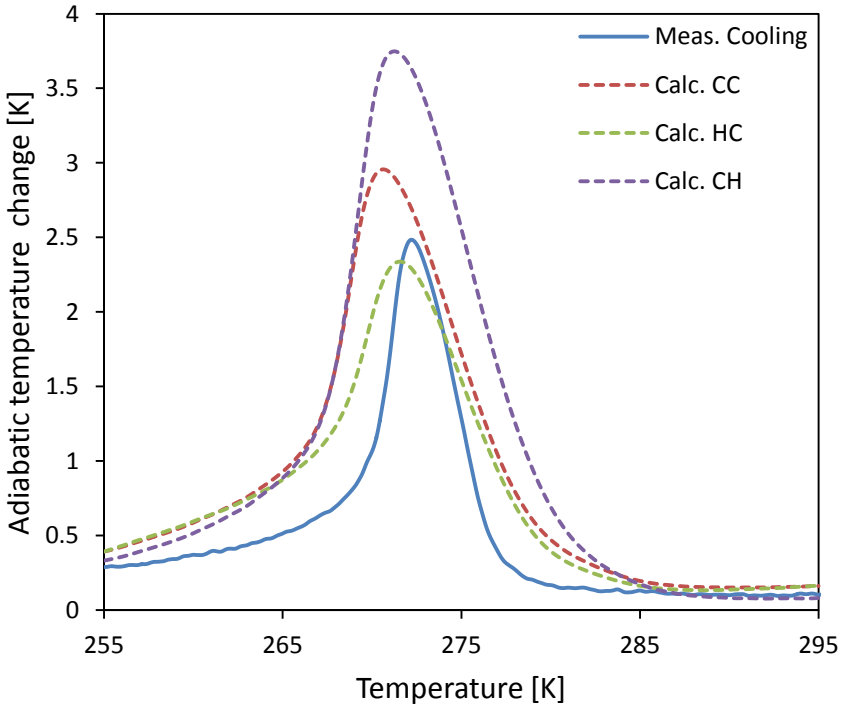

Figure 4-18 – Material 1 measured cooling adiabatic temperature change data compared against three calculated adiabatic temperature change data sets.

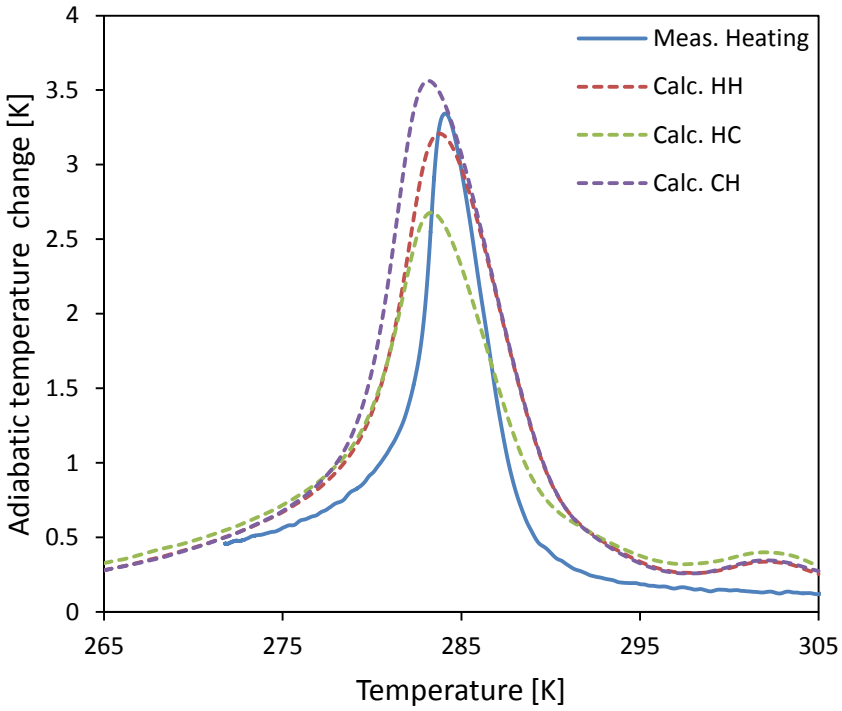

Figure 4-19 – Material 2 measured heating adiabatic temperature change data compared against three calculated adiabatic temperature change data sets.

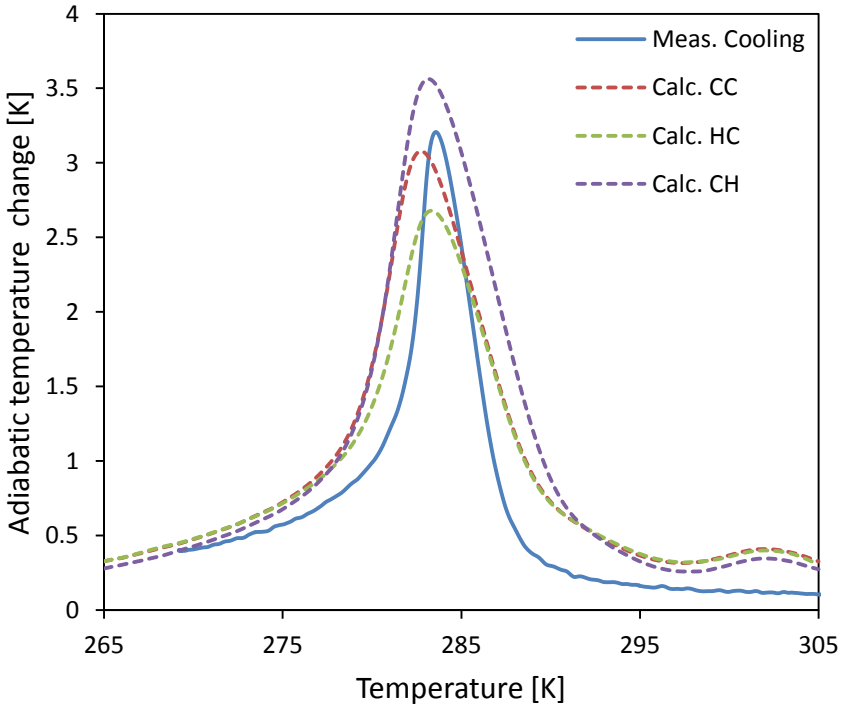

Figure 4-20 – Material 2 measured cooling adiabatic temperature change data compared against three calculated adiabatic temperature change data sets.

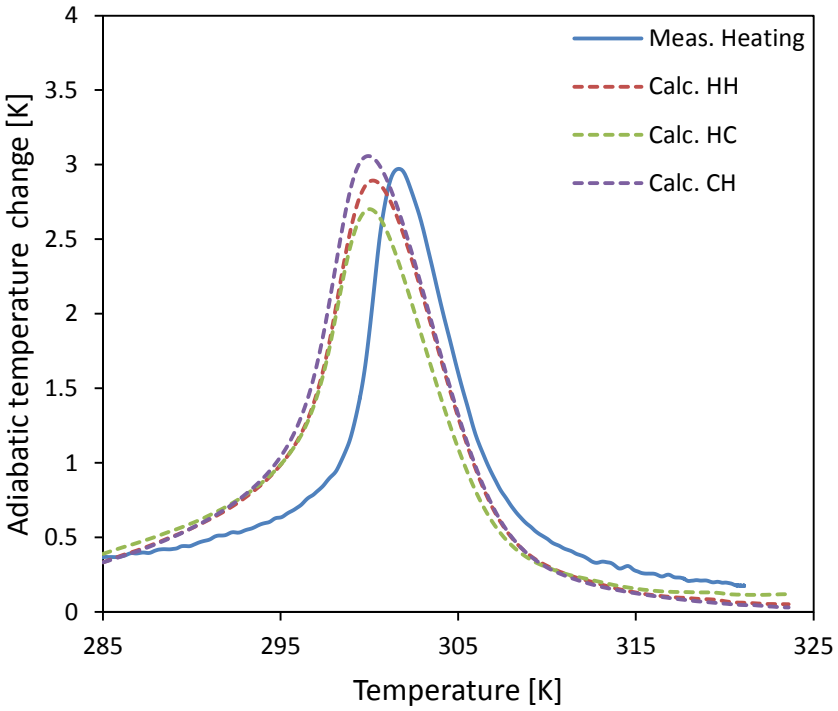

Figure 4-21 – Material 7 measured heating adiabatic temperature change data compared against three calculated adiabatic temperature change data sets.

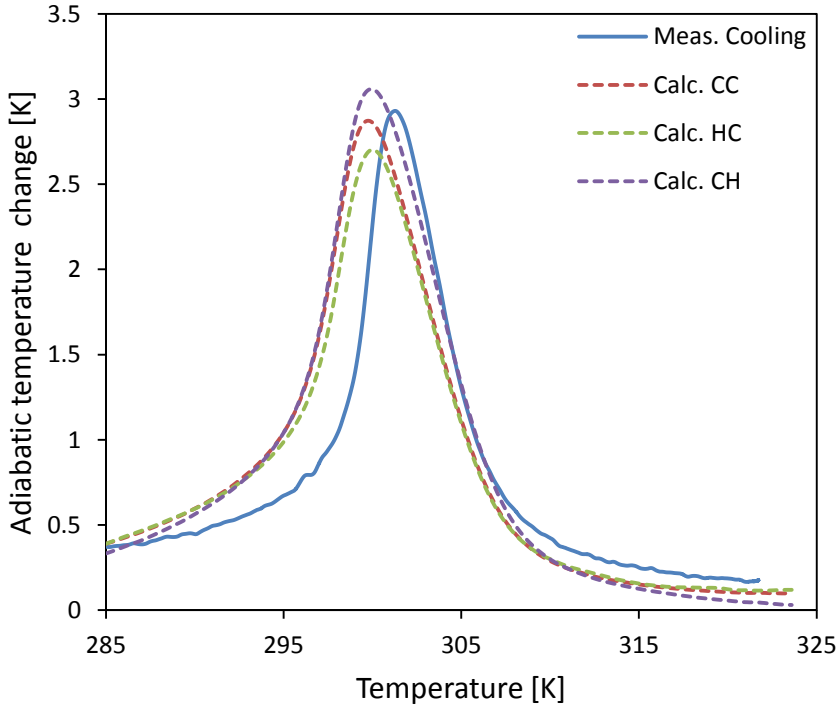

Figure 4-22 – Material 7 measured cooling adiabatic temperature change data compared against three calculated adiabatic temperature change data sets.

Table 4-1 – The three metrics that define the measured and calculated ΔT_{ad} curves for all nine alloys are presented in this table. Two other properties are presented here, hysteresis, and dT / dH . Hysteresis (Hyst.) is defined here as the difference in temperature between the heating and cooling zero field specific heat peaks. dT / dH is defined here as the shift in the temperature of the peak specific heat with increasing field strength.

	Measured data							Calculated data			
Mat	Curie Temp. [K]	Hyst [K]	Hyst path	dT/dH [K/T]	ΔT-peak [K]	T-peak [K]	FWHM [K]	Hyst path	ΔT-peak [K]	T-peak [K]	FWHM [K]
1	271	1.2	heating	4.3	2.6	272.8	5.1	HH	3.2	272.1	7.8
			cooling	4.1	2.5	272.2	4.7	CC	3.0	270.6	8.0
								HC	2.3	271.6	8.6
2	282.7	0.8	heating	4.4	3.3	284.1	4.1	HH	3.2	283.8	7.3
			cooling	4.4	3.2	283.6	4.0	CC	3.1	282.7	7.3
								HC	2.7	283.3	7.6
3	286.6	0.7	heating	4.5	2.7	288.6	5.8	HH	2.8	288.2	7.7
			cooling	4.6	2.7	288.4	5.8	CC	2.8	287.2	8.0
								HC	2.4	287.8	7.1
4	288.5	0.4	heating	4.6	3.1	291.2	5.3	HH	2.8	290.5	8.1
			cooling	4.6	3.0	290.8	5.0	CC	2.8	289.7	8.1
								HC	2.6	290.1	8.1
5	292.1	0.2	heating	4.5	3.3	294.5	4.4	HH	3.2	293.6	6.9
			cooling	4.4	3.3	293.9	4.1	CC	3.0	292.9	6.9
								HC	2.8	293.2	6.7
6	295.5	0.2	heating	4.8	2.9	298.5	5.4	HH	2.7	297.1	7.4
			cooling	4.8	2.9	298.0	5.0	CC	2.7	296.6	7.4
								HC	2.5	296.9	7.3
7	298.7	0.1	heating	4.8	3.0	301.6	5.7	HH	2.9	300.2	7.6
			cooling	4.7	2.9	301.3	5.5	CC	2.9	299.8	7.5
								HC	2.7	300.0	7.5
8	301.9	0.6	heating	4.5	2.6	304.7	7.0	HH	2.7	303.2	8.1
			cooling	4.7	2.5	304.1	6.7	CC	2.8	302.6	8.2
								HC	2.5	303.0	8.1
9	312	0.3	heating	4.7	2.6	315.9	7.2	HH	2.9	313.4	8.4
			cooling	4.8	2.6	315.5	7.2	CC	3.0	312.9	8.4
								HC	2.7	313.3	8.3

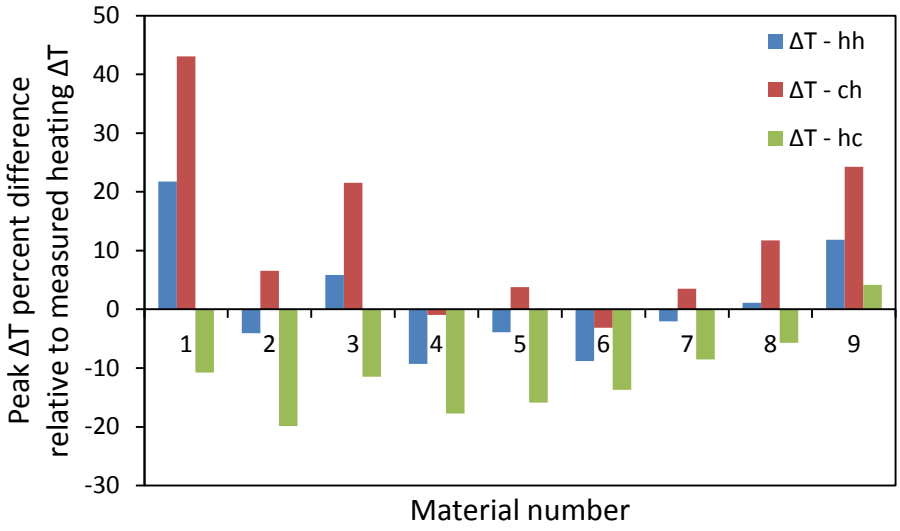

Figure 4-23 – Calculated ΔT_{ad} peak magnitudes relative to the measured heating ΔT_{ad} peak. A positive value indicates calculated values are higher than measured. A negative value indicates calculated values are lower than measured. The Curie temperature increases with material number.

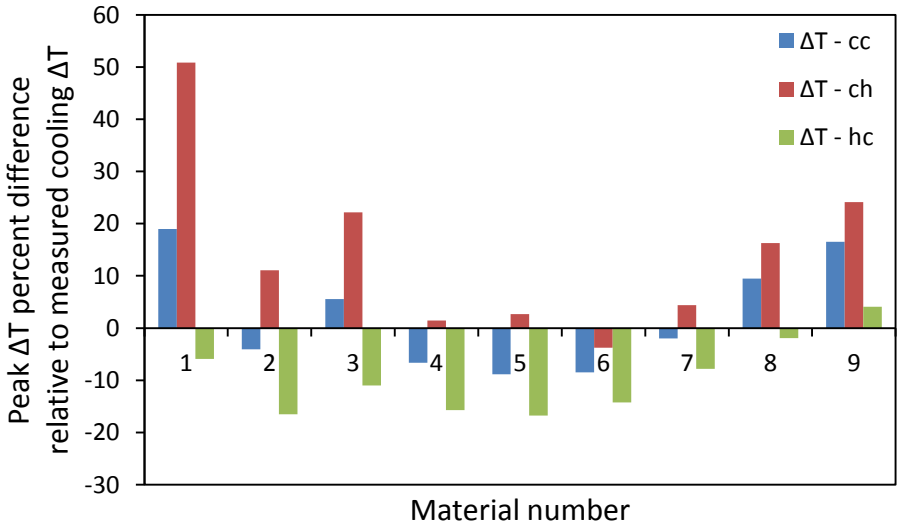

Figure 4-24 – Calculated ΔT_{ad} peak magnitudes relative to the measured cooling ΔT_{ad} peak.

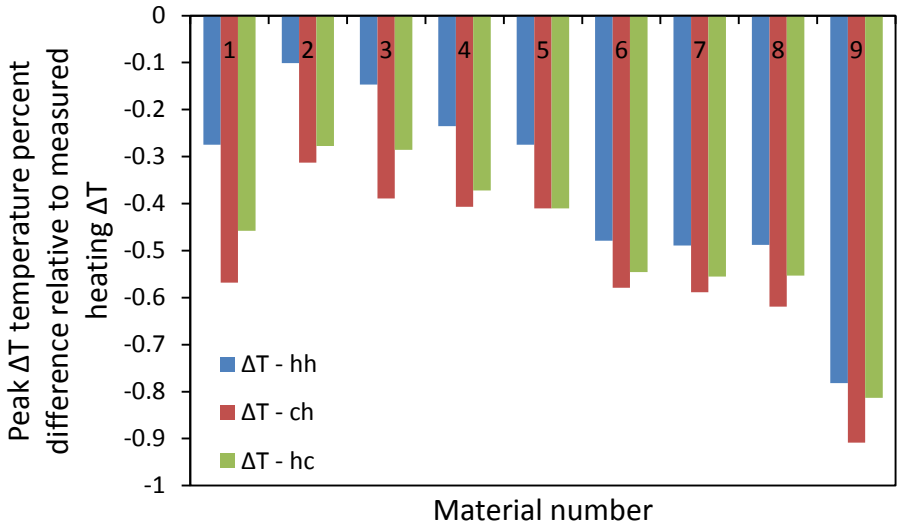

Figure 4-25 – Calculated ΔT_{ad} peak temperatures relative to the measured heating ΔT_{ad} peak.

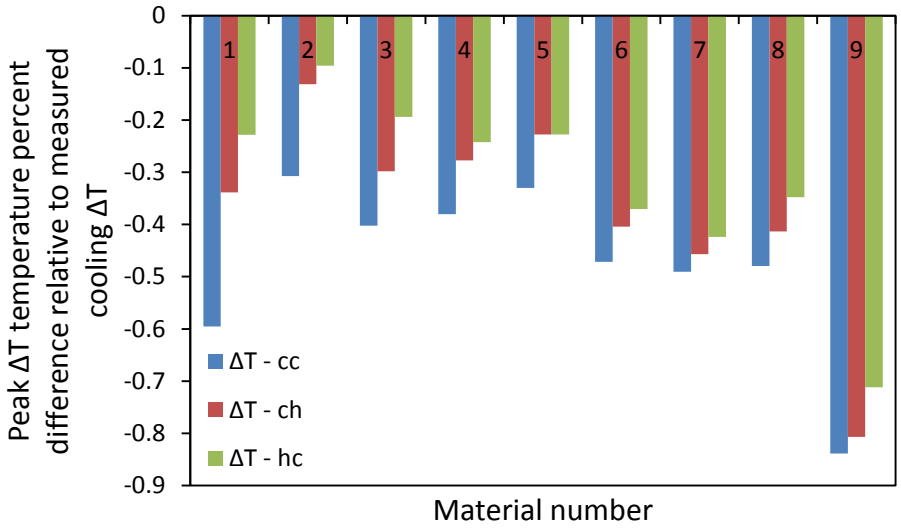

Figure 4-26 – Calculated ΔT_{ad} peak temperatures relative to the measured cooling ΔT_{ad} peak.

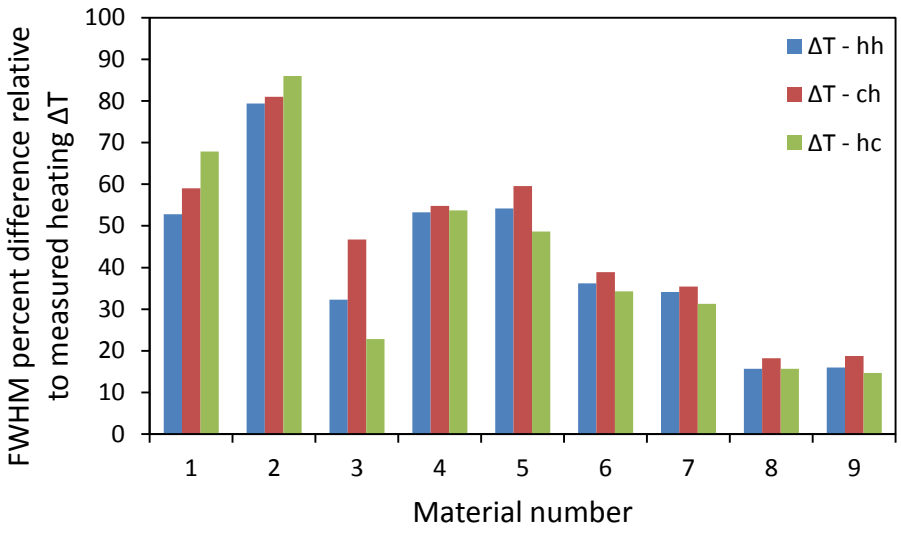

Figure 4-27 – Calculated ΔT_{ad} FWHM relative to the measured heating ΔT_{ad} FWHM.

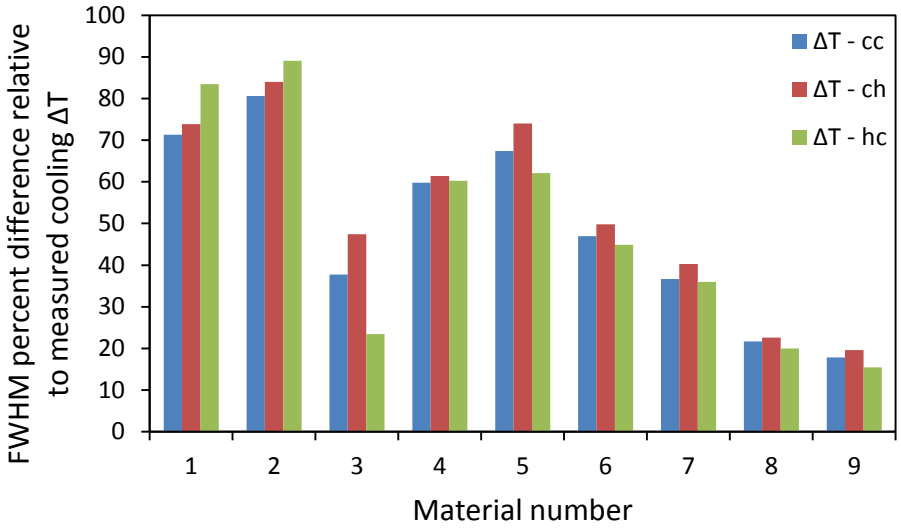

Figure 4-28 – Calculated ΔT_{ad} FWHM relative to the measured cooling ΔT_{ad} FWHM.

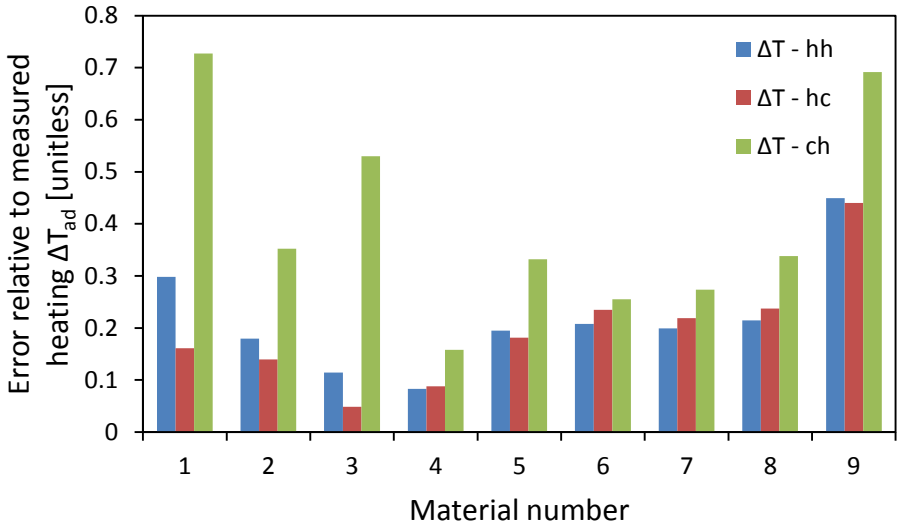

Figure 4-29 – Error relative to measured heating ΔT_{ad} .

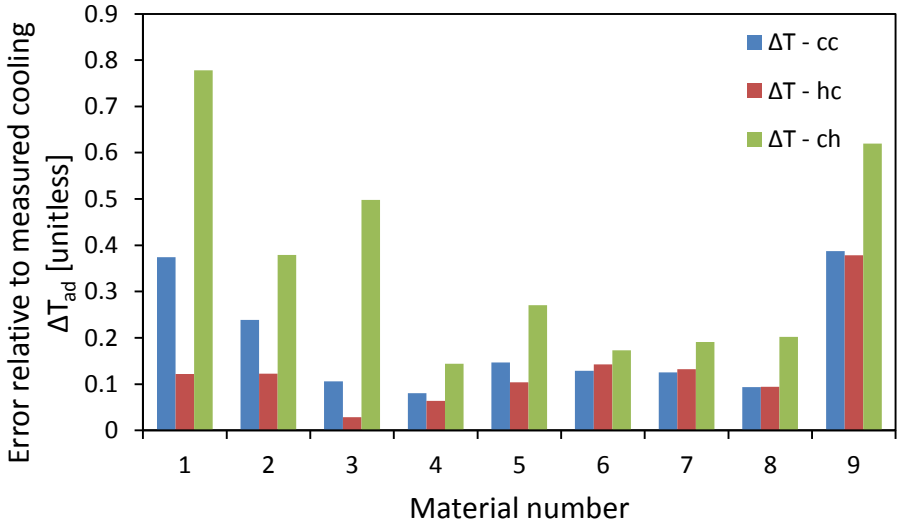

Figure 4-30 - Error relative to measured cooling ΔT_{ad} .

Table 4-2 – The 9 material average errors between calculated and measured ΔT_{ad} are presented.

	ΔT_{ad} - HH	ΔT_{ad} - CC	ΔT_{ad} - HC	ΔT_{ad} - CH
9 material average Error relative to heating ΔT_{ad}	0.22	-	0.19	0.41
9 material average Error relative to cooling ΔT_{ad}	-	0.19	0.13	0.36

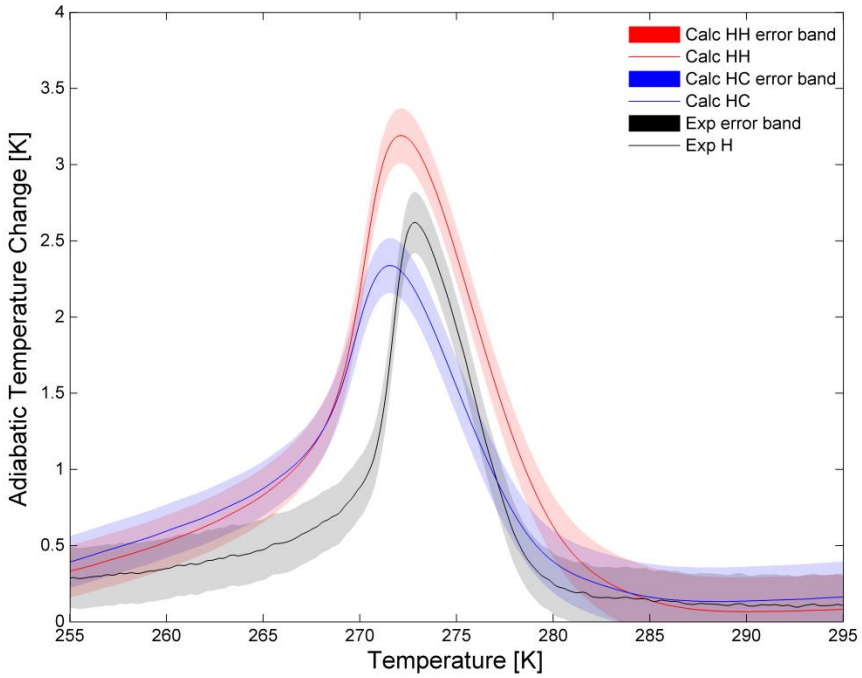

Figure 4-31 – Material 1 measured heating adiabatic temperature change data compared against two calculated adiabatic temperature change data sets. The shaded areas represent the uncertainties of each data set.

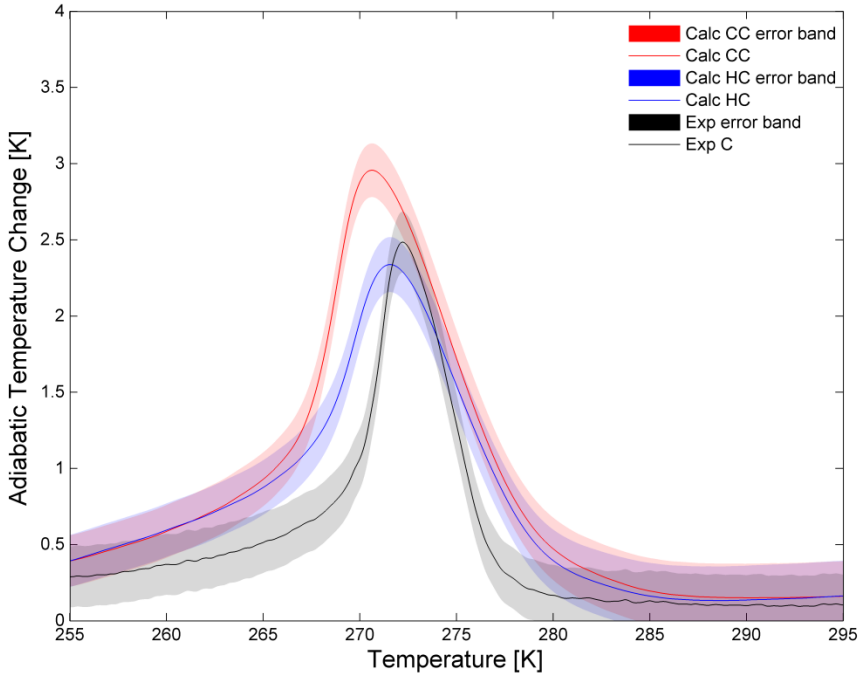

Figure 4-32 – Material 1 measured cooling ΔT_{ad} data compared to two calculated ΔT_{ad} data sets.

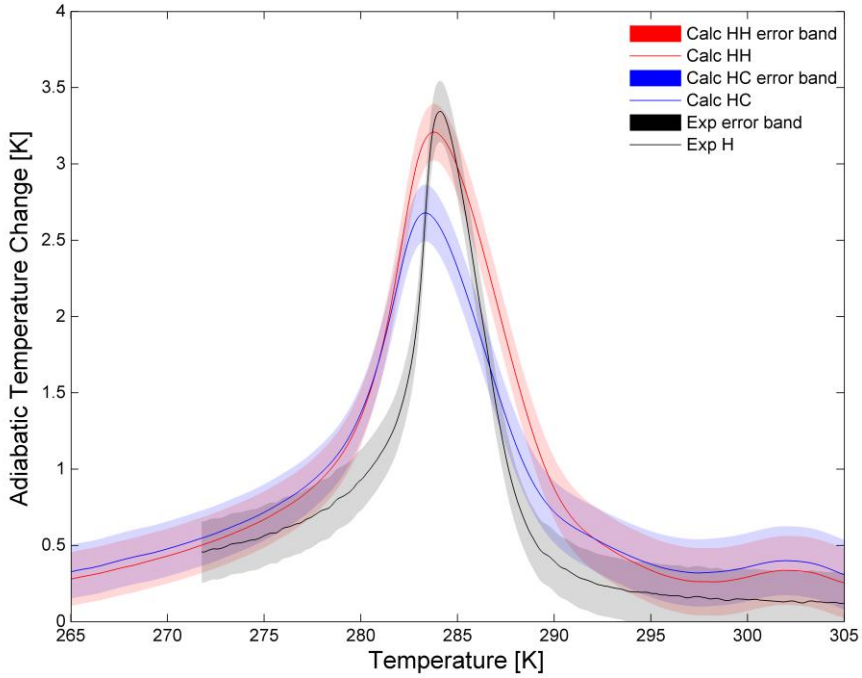

Figure 4-33 – Material 2 measured heating adiabatic temperature change data compared against two calculated adiabatic temperature change data sets.

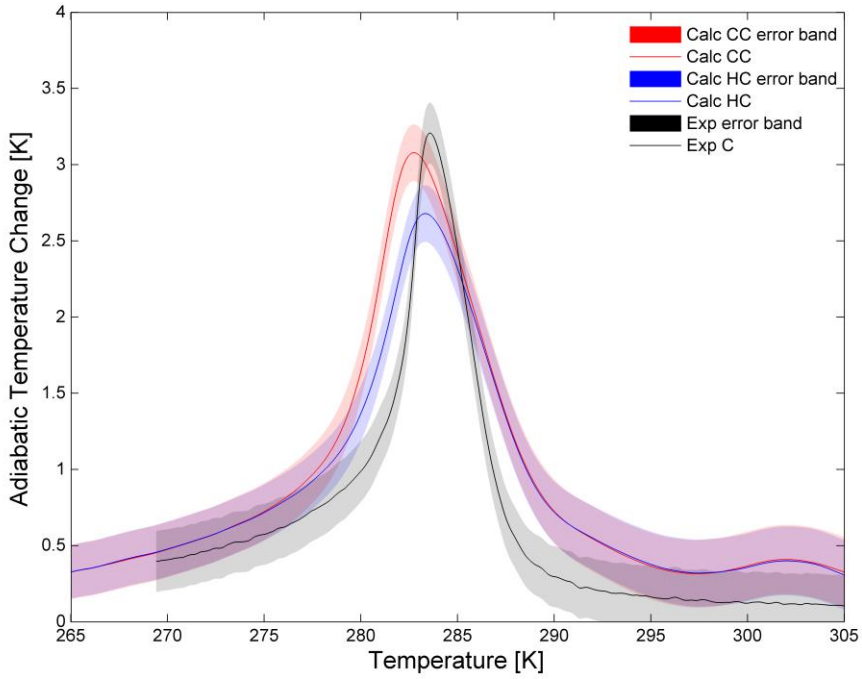

Figure 4-34 – Material 2 measured cooling ΔT_{ad} data compared to two calculated ΔT_{ad} data sets.

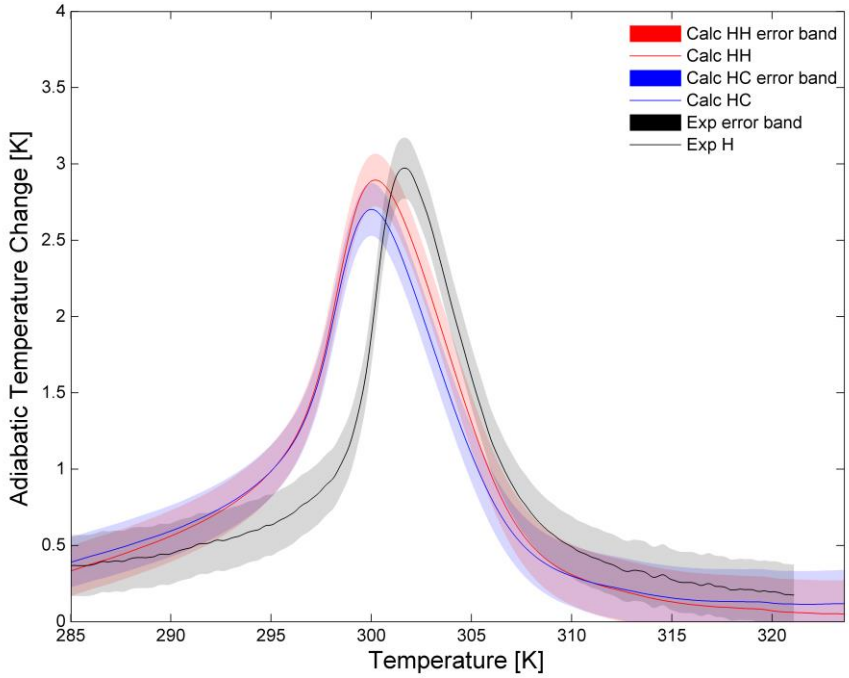

Figure 4-35 – Material 7 measured heating adiabatic temperature change data compared against two calculated adiabatic temperature change data sets.

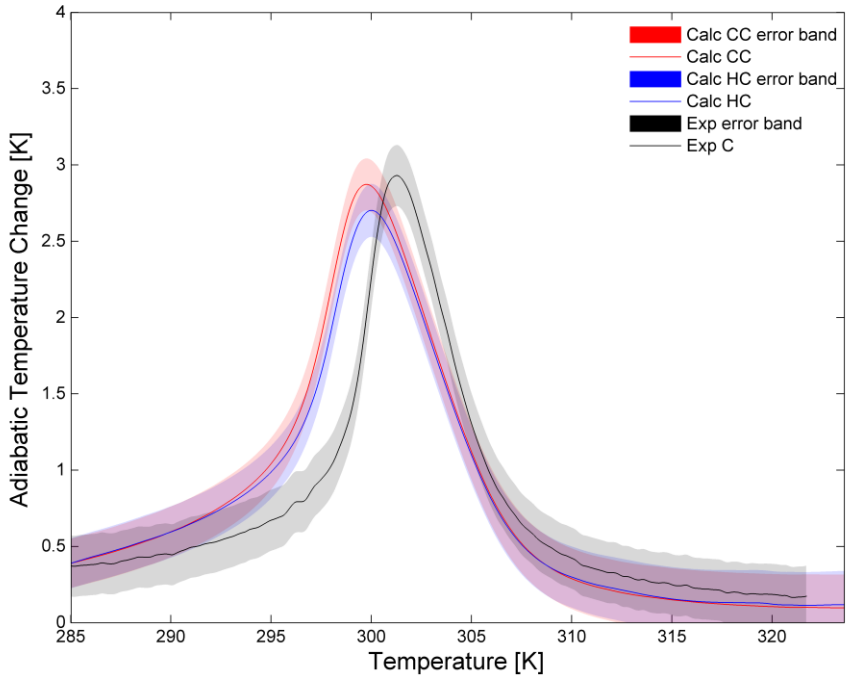

Figure 4-36 – Material 7 measured cooling ΔT_{ad} data compared to two calculated ΔT_{ad} data sets.

Chapter 5 – Discussion

$MnFeP_{1-x}As_x$ alloy results presented in Chapter 4 are discussed. Demagnetization corrections on specific heat and magnetization data and their impact on calculated ΔT_{ad} are explained. The differences between calculated and measured ΔT_{ad} are explored.

5.1. Demagnetization

Three data sets are involved in this study; specific heat, magnetization and adiabatic temperature change. The sample shapes used for specific heat and magnetization measurements cause demagnetizing effects while the sample shape used for ΔT_{ad} measurements minimize demagnetizing effects (see Sections 3.1, 3.4, 3.5 and 3.6). Since demagnetization effects are minimized in the ΔT_{ad} samples it is assumed that the applied field is equal to the internal field. Due to demagnetization, the applied and internal fields are not assumed to be equal in the specific heat and magnetization data. Because specific heat and magnetization data are used to calculated ΔT_{ad} which is then compared against the measured ΔT_{ad}, correcting for demagnetization is essential so that all the data is presented in terms of internal field. The magnitude of ΔT_{ad} is dependent on the low and high field the material experience, the larger the field change the larger the magnitude of ΔT_{ad}. In this study the field strength oscillates between zero and 1.1T. At zero field there are no demagnetizing effects, only the high field data must be corrected. Correcting high field for demagnetization essentially increases the field change between low and high field since a higher applied field is required to attain an internal field of 1.1T. The larger field change leads to a larger ΔT_{ad} as can be seen in Figure 4-15. As a

result, the demagnetization correction increases the peak magnitude of calculated ΔT_{ad} by approximately 0.3 Kelvin on average.

5.2. Measured versus calculated ΔT_{ad} of $MnFeP_{1-x}As_x$ alloys

Calculated ΔT_{ad} results are compared to measured values of nine $MnFeP_{1-x}As_x$ alloys. Figure 4-17 to Figure 4-22 display the calculated and measured ΔT_{ad} data for three sample alloys. There are two figures for each sample; one plots calculated $\Delta T_{ad,HH}$, $\Delta T_{ad,CH}$ and $\Delta T_{ad,HC}$ against the measured heating ΔT_{ad} while the other plots calculated $\Delta T_{ad,CC}$, $\Delta T_{ad,CH}$ and $\Delta T_{ad,HC}$ curves and measured cooling ΔT_{ad}. The two calculated curves involving heating and cooling data, $\Delta T_{ad,CH}$ and $\Delta T_{ad,HC}$, are plotted against both heating and cooling measured data because they are a combination of both. $\Delta T_{ad,CH}$ over predicts in all six figures. In Figure 4-17 and Figure 4-18 it appears that $\Delta T_{ad,HC}$ gives the best agreement with the measured ΔT_{ad} while in Figure 4-19 and Figure 4-20 it appears that $\Delta T_{ad,HH}$ and $\Delta T_{ad,CC}$ give the best agreement with measure ΔT_{ad}. These results show there is no obvious best method for calculating ΔT_{ad}.

Figure 4-23 to Figure 4-30 plot the percent differences between the calculated and measured ΔT_{ad} data metrics which include peak magnitude $\left(\Delta T_{peak}\right)$, peak temperature $\left(T_{peak}\right)$, full width at half maximum $\left(FWHM\right)$, and total error. Figure 4-16 provides a diagram of the metrics on a sample ΔT_{ad} curve. The percent difference between the calculated and measured peak ΔT_{ad} are plotted in Figure 4-23 and Figure 4-24. It can be seen that for all materials but material 9 the magnitude of $\Delta T_{ad,HC}$ peak is smaller than the

calculated ΔT_{ad}. The $\Delta T_{ad,HH}$, $\Delta T_{ad,CC}$ and $\Delta T_{ad,CH}$ data do not show a trend in Figure 4-23 and Figure 4-24. Figure 4-25 and Figure 4-26 plot the percent difference between the calculated and measured T_{peak}. It can be seen in the two figures that all calculated T_{peak} are colder than the measured T_{peak}. The difference between measured and calculated also appears to increase with Curie temperature. The percent different between the calculated and measured $FWHM$ are plotted in Figure 4-27 and Figure 4-28. It can be seen that for all materials the $FWHM$ of the calculated curves are larger than the measured curves and that this difference appears to decrease with Curie temperature. An error metric introduced in Section 4.4 is presented to show the error between the calculated and measured ΔT_{ad} curves. Figure 4-29 and Figure 4-30 plot the error metric. These figures and Table 4-2, which gives a nine material average, show that the $\Delta T_{ad,CH}$ calculation method gives the largest error of the four methods.

Two consistent differences between the calculated and measured ΔT_{ad} curves are the peak location and $FWHM$. The peak locations of the calculated curves are consistently colder than the measured curves. The $FWHM$ of the calculated curves are consistently larger than the measured curves. The source of these errors is unclear but it could be in part due to the reversible assumption made in the entropy calculation (see Section 2.1). The errors could also be attributed to the source data used from BASF.

Figure 4-31 to Figure 4-36 are the same as Figure 4-17 to Figure 4-22 with uncertainty bands added and $\Delta T_{ad,CH}$ data removed. These graphs are plotted to show the uncertainties in both measured and calculated data. Figure 4-31 to Figure 4-34 show results from material 1 and 2 where the calculated data differs more than the uncertainty

bands. Figure 4-35 and Figure 4-36 show results from material 7 where the calculated data differs less than the uncertainty bands. As can be seen in Table _ the hysteresis of material 7 is 0.1 Kelvin. These figures should that when dealing with materials with small hysteresis, the uncertainty in the calculated ΔT_{ad} curves is greater than the differences between them. This makes it difficult to make distinctions between the different calculated curves.

The general shape of a ΔT_{ad} can be defined by ΔT_{peak} , and $FWHM$. ΔT_{peak} and $FWHM$ of the measured and calculated ΔT_{ad} curves are plotted against the hysteresis of each material in Figure 5-1 to Figure 5-4 to explore the effect of thermal hysteresis on the shape of ΔT_{ad} curves. The expected result [13] is that ΔT_{peak} and the $FWHM$ decrease with increasing hysteresis but as can be seen in Figure 5-1 to Figure 5-4 there is no visible trend in the data. The largest hysteresis of the nine alloys in 1.2 Kelvin. A trend may be visible in materials with larger thermal hysteresis. These results are in agreement with [31] which states that thermal hysteresis of less than 4 Kelvin will not impact ΔT_{ad} .

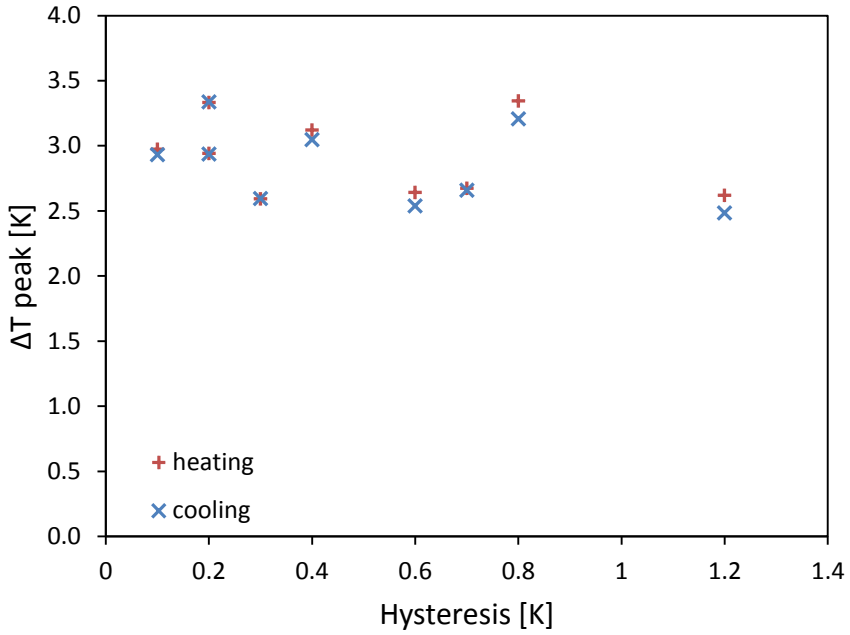

Figure 5-1 – Measured peak ΔT_{ad} is plotted against hysteresis for all nine alloys.

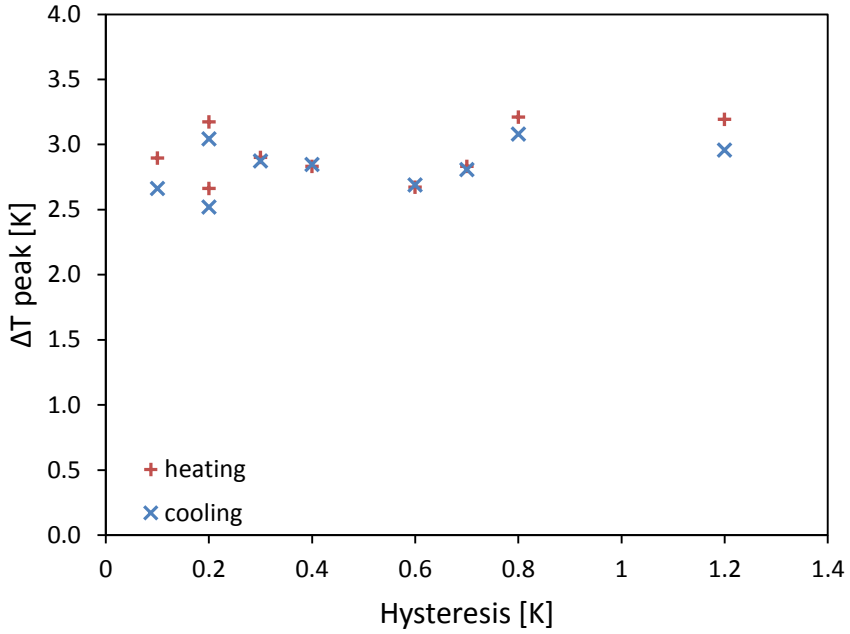

Figure 5-2 – Calculated peak ΔT_{ad} is plotted against hysteresis for all nine alloys. Heating represents calculated $\Delta T_{ad,HH}$ and cooling represents calculated $\Delta T_{ad,CC}$.

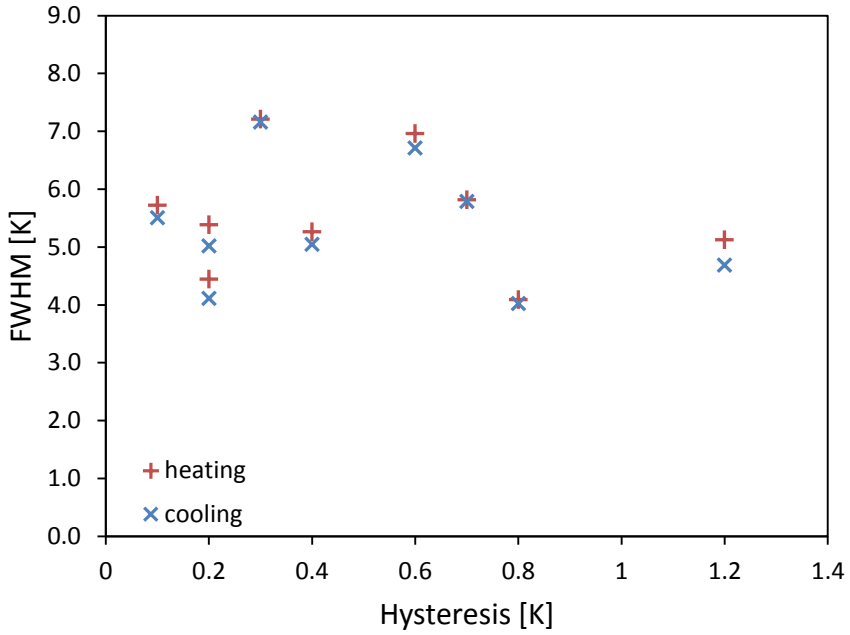

Figure 5-3 – Measured FWHM is plotted against hysteresis for all nine alloys.

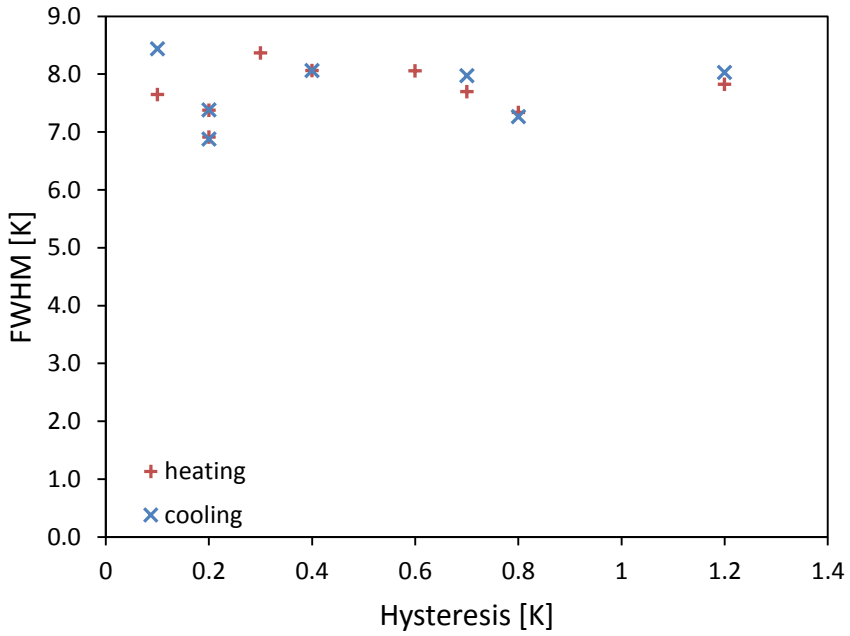

Figure 5-4 – Calculated FWHM is plotted against hysteresis for all nine alloys. Heating represents calculated $\Delta T_{ad,HH}$ and cooling represents calculated $\Delta T_{ad,CC}$.

Current data and analysis does not yield a clear calculation method that best aligns with measured data. With respect to heating ΔT_{ad} data, $\Delta T_{ad,HH}$ and $\Delta T_{ad,HC}$ align closest. $\Delta T_{ad,CC}$ and $\Delta T_{ad,HC}$ align closest to measured cooling ΔT_{ad} data. In both comparisons $\Delta T_{ad,CH}$ over predicts. $\Delta T_{ad,CH}$ is the best case scenario yielding the largest ΔT_{ad}. $\Delta T_{ad,HC}$ is the worst case scenario yielding the smallest ΔT_{ad}. It has been said [13] that this material follows $\Delta T_{ad,HC}$, the worst case scenario. The current results show that $\Delta T_{ad,HH}$ and $\Delta T_{ad,CC}$ align with measured data as well as $\Delta T_{ad,HC}$ as can be seen in Figure 4-29, Figure 4-30, and Table 4-2.

5.3. Summary

The main points presented in this chapter on the analysis of calculated $MnFeP_{1-x}As_x$ alloy ΔT_{ad} are listed below.

1. T_{peak} of calculated ΔT_{ad} is colder than measured ΔT_{ad} for all nine materials.
2. $FWHM$ of calculated ΔT_{ad} is larger than measure ΔT_{ad} for all nine materials.
3. Points 1 and 2 could be in part due to the reversible assumption made during the entropy calculation or the accuracy of the source data.
4. $\Delta T_{ad,CH}$ deviates the most from measured data and therefore it is assumed that this case is not representative of the material behavior.
5. $\Delta T_{ad,peak}$ and $FWHM$ do not appear to be a strong function of the hysteresis for the nine materials studied. This agrees with [31].
6. Results show $\Delta T_{ad,HH}$ and $\Delta T_{ad,CC}$ align with measured data as well as $\Delta T_{ad,HC}$. This goes against the results of [13].

Chapter 6 – Conclusion and Recommendations

Adiabatic temperature change is calculated from specific heat and magnetization data of nine $MnFeP_{1-x}As_x$ alloys supplied by BASF. Confidence in the calculation process is improved with MFT calculated Gadolinium data and measured Gadolinium data from AMES laboratory. The calculated ΔT_{ad} of $MnFeP_{1-x}As_x$ alloys are compared against measured ΔT_{ad} data.

Calculated ΔT_{ad} data agree roughly with measured data for the nine data sets with two consistent errors; the T_{peak} of the calculated data are colder than the measured data and the $FWHM$ of the calculated data are larger than the measured data. The source of these errors could be due to the reversible assumption in the entropy calculation. The assumption may be invalid due to irreversibilities introduced by hysteresis. The data acquired from BASF could also be the source of the errors observed between calculated and measured ΔT_{ad}.

Results from nine $MnFeP_{1-x}As_x$ materials do not show that $\Delta T_{ad,HC}$ aligns best with measured ΔT_{ad} data as has been suggested [13]. This analysis shows $\Delta T_{ad,HH}$, $\Delta T_{ad,CC}$ and $\Delta T_{ad,HC}$ align equally with measured data. $\Delta T_{ad,peak}$ and $FWHM$ do not appear to be a function of thermal hysteresis for the nine materials studied which agrees with [31] since the maximum thermal hysteresis of the nine materials is 1.2 Kelvin which is lower than the field induced peak specific heat change. These results suggest that hysteresis of less than 1.2 Kelvin does not have an impact on ΔT_{ad}.

Conducting the same analysis on more data sets of $MnFeP_{1-x}As_x$ alloys could help determine whether or not the source data caused the discrepancy between calculated and measured ΔT_{ad}. Analysing data sets of $MnFeP_{1-x}As_x$ alloys with larger thermal hysteresis should be conducted. In doing so, the 4 Kelvin thermal hysteresis limit suggested by [31] as the threshold above which the ΔT_{ad} begins to decrease could be investigated. This would also help in determining the validity of the results from [13]. According to [13] the higher thermal hysteresis materials should have a decreased ΔT_{ad}.

Bibliography

[1] EIA, “Residential Sector Key Indicators and Consumption,” 2012. [Online]. Available: http://www.eia.gov/oiaf/aeo/tablebrowser/#release=AEO2014ER&subject=0-AEO2014ER&table=4-AEO2014ER&region=0-0&cases=full2013-d102312a,ref2014er-d102413a.

[2] NOAA, “Degree Day Explanation,” 2005. [Online]. Available: http://www.cpc.ncep.noaa.gov/products/analysis_monitoring/cdus/degree_days/ddayexp.shtml.

[3] O. Tegus, E. Brück, K. H. J. Buschow, and F. R. de Boer, “Transition-metal-based magnetic refrigerants for room-temperature applications.,” *Nature*, vol. 415, no. 6868, pp. 150–2, Jan. 2002.

[4] ChartsBin, “Worldwide Cooling Needs,” 2014. [Online]. Available: http://chartsbin.com/view/1030.

[5] K. A. Gschneidner and V. K. Pecharsky, “Thirty years of near room temperature magnetic cooling: Where we are today and future prospects,” *Int. J. Refrig.*, vol. 31, no. 6, pp. 945–961, Sep. 2008.

[6] K. A. Gschneidner and V. K. Pecharsky, “Magnetocaloric materials,” no. 1, pp. 387–429, 2000.

[7] A. Smith, C. R. H. Bahl, R. Bjørk, K. Engelbrecht, K. K. Nielsen, and N. Pryds, “Materials Challenges for High Performance Magnetocaloric Refrigeration Devices,” *Adv. Energy Mater.*, vol. 2, no. 11, pp. 1288–1318, Nov. 2012.

[8] K. A. Gschneidner, “Gadolinium data,” personal communication 1995.

[9] D. Asten, “MnFePAs material data,” personal communication 2014.

[10] K. Nielson, “Corrected Gadolinium data.” personal communication.

[11] E. Brück, O. Tegus, L. Zhang, X. W. Li, F. R. de Boer, and K. H. J. Buschow, “Magnetic refrigeration near room temperature with Fe2P-based compounds,” *J. Alloys Compd.*, vol. 383, no. 1–2, pp. 32–36, Nov. 2004.

[12] E. Brück, O. Tegus, D. T. C. Thanh, and K. H. J. Buschow, “Magnetocaloric refrigeration near room temperature (invited),” *J. Magn. Magn. Mater.*, vol. 310, no. 2, pp. 2793–2799, Mar. 2007.

[13] K. Engelbrecht, K. K. Nielsen, C. R. H. Bahl, C. P. Carroll, and D. van Asten, "Material properties and modeling characteristics for MnFeP[sub 1−x]As[sub x] materials for application in magnetic refrigeration," *J. Appl. Phys.*, vol. 113, no. 17, p. 173510, 2013.

[14] J. M. D. Coey, *Magnetism and Magnetic Materials*. New York: Cambridge University Press, 2009.

[15] M. Reis, *Fundamentals of Magnetism*. Academic Press, 2013.

[16] K. H. J. Buschow and F. R. de Boer, *Physics of Magnetism and Magnetic Materials*. New York: Kluwer Academic/Plenum Publishers, 2003.

[17] A. Morrish, *The Physical Principles of Magnetism*. John Wiley & Sons, Inc., 1965.

[18] E. S. R. Gopal, *Specific Heats at Low Temperatures*. New York: Premium Press, 1966.

[19] C. Kittel, *Introduction to Solid State Physics*. New York: John Wiley & Sons, Inc., 1953.

[20] A. M. Tishin and Y. I. Spichkin, *The Magnetocaloric Effect and its Applications*. CRC Press, 2003.

[21] C. P. Bean and D. S. Rodbell, "Magnetic Disorder as a First-Order Phase Transformation." Physical Review, 1962.

[22] C. Aprea, a. Greco, and a. Maiorino, "The use of the first and of the second order phase magnetic transition alloys for an AMR refrigerator at room temperature: A numerical analysis of the energy performances," *Energy Convers. Manag.*, vol. 70, pp. 40–55, Jun. 2013.

[23] O. Tegus, G. X. Lin, W. Dagula, B. Fuquan, L. Zhang, E. Brück, F. R. de Boer, and K. H. J. Buschow, "A model description of the first-order phase transition in MnFeP1−xAsx," *J. Magn. Magn. Mater.*, vol. 290–291, pp. 658–660, 2005.

[24] R. I. Joseph, "Ballistic Demagnetizing Factor in Uniformly Magnetized Cylinders," *J. Appl. Phys.*, vol. 37, no. 13, p. 4639, 1966.

[25] M. Abramowitz and I. A. Stegun, *Handbook of Methematical Functions*. New York, 1964.

[26] G. Hohne, W. Hemminger, and H. Flammersheim, *Differential Scanning Calorimetry*. Springer Science & Business Media, 2003, p. 298.

[27] S. Foner, "Vibrating Sample Magnetometer," *Licon Laboritory MIT*, 1956.

[28] Quantum Design, “Versa Lab Vibrating Sample Magnetometer by Quantum Design.” [Online]. Available: http://www.lot-qd.de/files/downloads/qd/en/Versalab_en.pdf. [Accessed: 01-Jan-2014].

[29] V. K. Pecharsky and K. a. Gschneidner, “Magnetocaloric effect from indirect measurements: Magnetization and heat capacity,” *J. Appl. Phys.*, vol. 86, no. 1, p. 565, 1999.

[30] A. J. Wheeler and A. R. Ganji, *Introduction to Engineering Experimentation*. New Jersey: Pearson Education, 2004.

[31] F. Guillou, H. Yibole, G. Porcari, L. Zhang, N. H. van Dijk, and E. Brück, “Magnetocaloric effect, cyclability and coefficient of refrigerant performance in the MnFe(P, Si, B) system,” *J. Appl. Phys.*, vol. 116, no. 6, p. 063903, Aug. 2014.

Appendix A – Isothermal field induced entropy change derivation

Tishin 2003 states that the internal energy of a system is a function of entropy, volume and magnetic field or magnetization

$$u = u\left(s, V, B_a\right) \tag{1.1}$$

$$u = u(s, V, m). \tag{1.2}$$

The total differential of internal energy is then given by

$$du = Tds - pdV + mdB_a \tag{1.3}$$

or

$$du = Tds - pdV + B_a dm \tag{1.4}$$

where the latter two terms are work terms. The magnetic work term $B_a dm$ is positive in the above equation because the internal energy of the system increases with magnetization. The Gibbs free energy is defined by Tishin as

$$g = u - Ts + pV - mB_a. \tag{1.5}$$

Taking the total differential of Gibbs free energy yields

$$dg = du - Tds - sdT + pdV + Vdp - mdB_a - B_a dm. \tag{1.6}$$

By substituting equation (1.4) into equation (1.6), the above differential is simplified to

$$dg = -sdT + Vdp - mdB_a. \tag{1.7}$$

Taking the temperature derivative and the magnetic derivative of equation (1.7) gives the entropy and magnetization respectively.

$$s\left(T, B_a\right) = -\left(\frac{\partial g}{dT}\right)_{B_a} \tag{1.8}$$

$$m\left(T, B_a\right) = -\left(\frac{\partial g}{\partial B_a}\right)_T \tag{1.9}$$

Since Gibbs free energy is a thermodynamic potential, its second order mixed derivatives are equal, therefore

$$\left(\frac{\partial s}{\partial B_a}\right)_T = -\frac{\partial}{\partial B_a}\left(\frac{\partial g}{\partial T}\right)_{B_a} = -\frac{\partial}{\partial T}\left(\frac{\partial g}{\partial B_a}\right)_T = \left(\frac{\partial m}{\partial T}\right)_{B_a}. \tag{1.10}$$

The result is one of Maxwell's relations

$$\left(\frac{\partial s}{\partial B_a}\right)_T = \left(\frac{\partial m}{\partial T}\right)_{B_a} . \tag{1.11}$$

Finally, taking the integral with respect to the applied magnetic field strength to both sides of equation (1.11) yields an expression for the change in entropy due to change in applied magnetic field strength

$$\Delta s_m\left(T, B_1, B_2\right) = \int_{B_1}^{B_2}\left(\frac{\partial m}{\partial T}\right)_{B_a} dB \tag{1.12}$$